

Computational Materials Design for Molecular Machinery: From Nanoporous Crystals to Nanoscale Racecars

by

Kutay Berk Sezginel

Bachelor of Science, Chemical and Biological Engineering, Koç University, 2013

Master of Science, Chemical and Biological Engineering, Koç University, 2015

Submitted to the Graduate Faculty of the
Swanson School of Engineering in partial fulfillment
of the requirements for the degree of
Doctor of Philosophy

University of Pittsburgh

2020

UNIVERSITY OF PITTSBURGH

SWANSON SCHOOL OF ENGINEERING

This dissertation was presented

by

Kutay Berk Sezginel

It was defended on

December 10, 2019

and approved by

Geoffrey R. Hutchison, Ph.D., Associate Professor, Department of Chemistry

Susan Fullerton, Ph.D., Assistant Professor, Department of Chemical and Petroleum Engineering

Giannis Mpourmpakis, Ph.D., Associate Professor, Department of Chemical and Petroleum
Engineering

Dissertation Director: Christopher E. Wilmer, Ph.D., Assistant Professor, Department of
Chemical and Petroleum Engineering

Copyright © by Kutay Berk Sezginel

2020

Computational Materials Design for Molecular Machinery: From Nanoporous Crystals to Nanoscale Racecars

Kutay Berk Sezginel, PhD

University of Pittsburgh, 2020

Over billions of years of evolution, Nature mastered molecular nanotechnology, manipulating atoms and molecules with high precision. Among them are machines that perform tasks such as protein synthesis (ribosomes), gene replication (DNA and RNA polymerases), transporting molecular cargo (kinesin and dynein), and locomotion (flagella). Today these machines serve as a source of inspiration for the design of artificial molecular machines (AMMs). We are now exploring molecular motors, actuators, and logic gates at the nanoscale just as we did at the macroscale in the 19th century with electric motors and combustion engines.

Inspired by the pursuit of AMMs, this dissertation describes my research on developing computational methods to aid in the design of AMMs with targeted geometry and functionality. We first focused on the design of nanoporous crystals, developing a novel algorithm that can test whether two given crystalline structures can interpenetrate each other. Using this algorithm, we screened a database of ~6000 metal-organic frameworks (MOFs) and identified 18 hetero-interpenetrating MOF candidates. We then found that interpenetration enhances thermal conductivity which is important for various applications such as adsorbent gas storage.

Later, we developed tools to study nanoscale racecars, which are large organic molecules (~200-2000 Da) designed to diffuse quickly on atomically smooth surfaces. Here we developed both computational strategies to study their surface diffusion and tools to rapidly build hypothetical nanocars and assess their surface diffusion performance. We found that the surface diffusion gets

slower with higher molecular weight and stronger molecule-surface interaction energy. We also suggested a geometric parameter, i.e. elevation weighted density, which we found to be useful for quickly ranking diffusion of different molecular designs. Our study suggests that by careful design of the molecular structure and selection of the appropriate surface, molecular diffusion can be tailored.

In summary, we show that by developing tools and using appropriate methods we can design and study properties of both static and dynamic molecular machines. We hope that these studies, and the tools developed, will collectively help to push the frontier of knowledge (even if incrementally) towards the eventual building of useful AMMs.

Table of Contents

Preface.....	xxi
1.0 A Brief History of Computational Materials Design for Molecular Machinery.....	1
1.1 An Introduction to Molecular Machines.....	1
1.2 Artificial Molecular Machines.....	4
1.2.1 Rotaxanes.....	5
1.2.2 Molecular Motors.....	6
1.2.3 Nanocars.....	7
1.2.4 Metal-Organic Frameworks.....	8
2.0 Discovery of Hypothetical Hetero-Interpenetrated MOFs with Arbitrarily	
Dissimilar Topologies and Unit Cell Shapes.....	11
2.1 Methodology.....	12
2.2 Results and Discussion.....	17
2.3 Conclusion.....	21
3.0 Rational Design of Metal-Organic Frameworks for Improved Thermal Transport	
.....	23
3.1 Thermal Transport in Interpenetrated Metal-Organic Frameworks.....	23
3.1.1 Methodology.....	24
3.1.2 Results and Discussion.....	25
3.1.3 Conclusion.....	31
3.2 Thermal Transport in Flexible Metal-Organic Frameworks.....	33
3.2.1 Methodology.....	34

3.2.2 Results and Discussion.....	36
3.2.3 Conclusion.....	40
4.0 Computational Methods for Rational Design of Nanocars and Modeling Their	
Diffusion on Metal Surfaces.....	42
4.1 Modeling Surface Diffusion of Large Organic Molecules	42
4.1.1 Methodology	46
4.1.2 Results and Discussion.....	48
4.1.3 Conclusion.....	54
4.2 Nanocar Builder Tool.....	56
4.2.1 Methodology	56
4.2.2 How to Build a Nanocar?	58
Appendix A Discovery of Hypothetical Hetero-Interpenetrated MOFs.....	60
Appendix A.1 Algorithm Description	60
Appendix A.2 Generating Unit Cell for Interpenetrating Structures	69
Appendix A.3 High-throughput Screening	71
Appendix A.4 Comparison with Literature	79
Appendix B Computational Methods and Supplementary Results for Thermal	
Conductivity of MOFs.....	83
Appendix B.1 Thermal Transport in Interpenetrated MOFs	83
Appendix B.2 Thermal Transport in Flexible MOFs.....	92
Appendix C Calculating Surface Diffusion of Large Molecules.....	98
Appendix C.1 Force Field Parameters	98

Appendix C.2 Calculating Diffusion Coefficient from Rigid Body Molecular Dynamics Simulations.....	99
Appendix C.3 Transition State Theory	103
Appendix C.4 Elevation Weighted Density	106
Appendix D Software Packages Developed	108
Appendix D.1 Ångstrom: a Python Package for Molecular Architecture and Visualization.....	108
Appendix D.2 Nanocar Builder Avogadro Plug-in.....	109
Appendix D.3 IPMOF: a Python Package for Discovering Interpenetrated MOFs ..	110
Appendix D.4 TherMOF: a Python Package for Investigating Thermal Transport in MOFs	110
Appendix D.5 Moleidoscope (Molecular Kaleidoscope)	111
Appendix D.6 Tutorials for Computational Chemistry Tools and Scientific Visualization.....	112
Bibliography	113

List of Tables

Table 1 Structural and crystallographic information for six hetero-interpenetrating MOF candidates.	20
Appendix Table 1 Force field parameters used in this study	65
Appendix Table 2 Chemical composition information for 18 hetero-interpenetrating MOF candidates	76
Appendix Table 3 Potential used for IRMOF-1 interactions.....	86
Appendix Table 4 Total number of atoms and total number of adsorbate molecules for simulation setups with different tilt angles.....	96
Appendix Table 5 Force field parameters for a Lennard-Jones potential modeling vdW interactions of gas molecules.....	97
Appendix Table 6 Simulation parameters used in this study to calculate vdW energy using a Lennard-Jones potential. All parameters are for pairs of atoms where the epsilon values are in kcal/mol and sigma values are in Å.	98

List of Figures

- Figure 1** Examples of artificial molecular machines.⁵ 1
- Figure 2** Examples of nanocars. (a) Light-driven motorized nanocar.¹⁰ Carborane-wheeled nanocars with (b) six and (c) four wheels.¹¹ (d) Electrically driven nanocar with motorized wheels.⁸ (e) Fullerene wheeled nanocar (hypothetical).¹² 2
- Figure 3** Self-assembly of metal-organic frameworks. (a) Building blocks are self-assembled to form porous crystals. (b) A wide variety of metal nodes and organic linkers can be used as building blocks to construct MOFs with different geometries..... 3
- Figure 4** Molecular machine structures. (a) Feringa second generation molecular motor with a (2'R)-methyl-2,3-dihydronaphthiopyran propeller and a 2-methoxythioxanthene stator. Rotation around the double bond is achieved with photochemical and thermal isomerization (b) Daisy chain rotaxane model with building blocks deconstructed as stopper, extender, and ring. Different molecular structures are shown for each building block. By carefully designing the molecular structure of the building blocks properties of the rotaxane such as force needed to switch, stimulus, and speed can be tuned..... 5
- Figure 5** Hetero-interpenetrating and polycatenated metal-organic frameworks with entangled frameworks colored individually. CCDC reference codes and associated publications are provided as follows (a) WEBZEK⁶⁹ (b) COGCOS⁶⁷ (c) EJAXOC⁷⁸ (d) ATEYED.⁷⁵ 9
- Figure 6** Interpenetration discovery algorithm description and candidate interpenetrated MOF total void fraction distribution. a) Energy map generation for MOF-5. Grid points are colored from light to dark red according to calculated energy values. b) Single unit-

cell interpenetration test procedure for two given MOFs. First, the unit cells are aligned. Second, one of the unit cells is rotated and then translated to a selected position (represented by a yellow point). For this selected orientation, energy values for each atom in the red unit cell are added to obtain the energy density. c) Simplified schematic for combining two unit cells into a supercell. The 2D supercell can be obtained by repeating the red unit cell 2 times in y and 4 times in x dimensions and repeating blue unit cell 3 times in both dimensions. d) Total void fraction (V_f^{total}) distribution for MOF combinations: selecting combinations with $V_f^{total} > 1$ (corresponding to ~4.28 million MOF combinations) and V_f^{total} distribution among selected combinations (ordered with increasing void fraction from dark to light blue). More information can be found in Appendix A1. 13

Figure 7 Experimental comparison of predicted MOFs. a) Comparison of XRD patterns of predicted interpenetrated MOF-5 and experimentally synthesized MOF-5; (b) schematic for interpenetration of MOF-5; (c) Comparison of XRD patterns of predicted interpenetrated WEBZEK and experimentally synthesized WEBZEK; (d) schematic for interpenetration of WEBZEK. 18

Figure 8 Number of MOF combinations selected at different steps in the analysis: (a) percentage of MOF combinations selected with respect to previous data set; (b) percentage distribution of homo and hetero interpenetration in MOF combinations that passed the extended unit cell test (here degenerate structures with different names are not considered as homo-interpenetration); (c) Overall structure discovery distribution of MOF combinations given in both axes with increasing void fraction (V_f^{total}). Crystallographic

information files (cif) for all structures can be accessed from IPMOF GitHub repository.⁹⁹

..... 19

Figure 9 Some of the candidate hetero-interpenetrated structures discovered in this study:

(a) 1 AXUBAW¹⁰⁷ [blue] + NODTIL¹⁰⁸ [red], (b) 2 IZEPAF¹⁰⁹ [blue] + WUHDAG¹¹⁰ [red],

(c) 3 UQOFOX¹¹¹ [blue] + VEJUP¹¹² [red], (d) 4 LEHXUT¹¹³ [blue] + XAMDUM02¹¹⁴

[red], (e) 5 LURRIA¹¹⁵ [blue] + MIBQAR06¹¹⁶ [red], (f) 6 HABRAF¹¹⁷ [blue] +

HANHAH¹¹⁸ [red]. 21

Figure 10 (a) Idealized porous crystal ($8 \times 8 \times 8$ cubic unit cells). (b) Bonding arrangement

for a single unit cell using Morse potentials (red bonds are modeled more strongly than

blue bonds). (c) Doubly interpenetrated unit cell with framework depicted as red and blue

(initial frameworks in each simulation are 5 \AA apart in each dimension. (d) Different

interpenetration configurations based on cubic IRMOF series¹²⁵: metal center distribution

with BPDC linker (IRMOF-9) and PDC linker (IRMOF-13) representing less and more

bulky linkers, respectively. Color scheme is as follows: Zn (blue spheres), O (red spheres),

C (gray spheres). 24

Figure 11 Effect of framework interaction on thermal conductivity and framework mobility

in terms of forcefield parameters. For each plot, each bin represents a simulation with

corresponding ϵ and σ values. The black bins on the upper right-hand side are for

simulations where high repulsive forces caused frameworks to collapse. (a) Thermal

conductivity (W/m K). (b) Thermal conductivity prediction error (%) for interpenetrated

framework using the relationship in Eq. 3-1. (c) Coupling constant (γ). (d) Thermal

conductivity prediction error (%) for interpenetrated framework using the relationship in

Eq. 3-2. (e) Mean squared displacement, MSD (\AA^2). Derivation of Eq. 3-2 and the full equation of the coupling constant is provided in Appendix B1. 27

Figure 12 Effect of interpenetration interaction on framework distances during simulation.

Framework interactions are modeled using Lennard-Jones potential. (a) σ : 3.5 \AA and (b) σ : 4.5 \AA with varying ϵ values in kcal/mol shown in figure. Grid size: 6 \AA and bin size: 1 \AA (c) ϵ : 0.105 kcal/mol and varying σ values shown in figure. Grid size: 12 \AA and bin size: 2 \AA (d) Framework distances are measured according to middle red atom with reference to corner atoms of the surrounding blue framework. 5 \AA \times 5 \AA \times 5 \AA cube shown as dashed box in 2 dimensions. The yellow-red bins represent the position of the other framework. (e) Time spent in given location are given in percentage. Color scale is limited to 50 % of simulation time for clarity. All results are for x and y directions from a single run. More information about the framework mobility calculations are provided in Appendix B1.. 28

Figure 13 Effect of atomic mass on thermal conductivity (a) Single MOF (b) Free

interpenetration (σ : 3.5 \AA) Dashed lines are equations shown in the figure. (c) Parity plot for predicted (Eq. 3-1) and simulated thermal conductivities for “free” and “locked” interpenetrated MOFs for different masses. For interpenetrated structures, atomic mass of the second framework (M_2) is modified whereas first framework atoms are always chosen as Ar ($M_1 \sim 40$ Da). Error bars represent one standard deviation of uncertainty. 30

Figure 14 Cross-sectional view of the idealized simple cubic structure and the harmonic

bonds and angles used in the potential. (b) Complete simulation box of the idealized simple cubic structure with pores filled with adsorbates at 5 molecules / nm^3 density. (c) The idealized structures tilted at different angles to generate different stages of transition from

contracted to expanded pores. 2 x 2 x 2 unit cell of the idealized structure at (d) 90°, (e) 70°, and (f) 50° tilt angles.	35
Figure 15 (a) Thermal conductivity vs tilt angle. (b) Thermal conductivity in the y-direction scaled with $\sin(\alpha)^3$ vs tilt angle.	37
Figure 16 Thermal conductivity contribution from bond and angle potentials in a) x and b) y directions. z direction not depicted as the results were almost identical to the x direction.	38
Figure 17 (a) Thermal conductivity of gas loaded structures vs the angle which resembles the stage of expansion. (b) y-direction thermal conductivity of the gas loaded structure scaled by $\sin(\alpha)^2$ vs angle.....	39
Figure 18 (a) Ratio of thermal conductivity for gas loaded and empty crystals at different stages of pore expansion. (b) Corrected gas diffusivity for gas loaded crystals at different stages of pore expansion.	40
Figure 19 Molecular structures used in this study with chemical names where abbreviations and chemical formulae are given in brackets: (a) p-carborane¹⁷³ [pC, C₂H₁₂B₁₀]; (b) fullerene¹⁷⁴ [C₆₀, C₆₀] (c) 4-trans-2-(pyrid-4-yl-vinyl) benzoic acid¹⁷⁵ [PVBA, C₁₄H₁₁O₂N]; (d) (Z)-1,6-di(naphthalen-2-yl)hexa-3-en-1,5-diyne¹⁷² [DNHD, C₂₆H₁₆]; (e) (Z)-1,6-bis-(4-(tert-butyl)phenyl)hexa-3-en-1,5-diyne¹⁷² [BtPHD, C₂₆H₂₈]; (f) tetrakis(phenylethynyl)ethane¹⁷² [TPEE, C₃₄H₂₀]; (g) decacylene¹⁶⁴ [DC, C₃₆H₁₈]; (h) hexa tert-butyl decacylene¹⁶⁴ [HtBDC, C₆₀H₆₆]; and (i) violet lander¹⁶³ [VL, C₁₀₈H₁₀₄]. Color scheme is as follows: C (black), N (blue), O (red), B (pink), H (light gray).....	45
Figure 20 Simulation setup for HtBDC. (a) Top view - molecules are placed in the center of a 39.1 x 41.5 Å Cu (110) surface. (b) Side view - each molecule is placed 5 Å above the	

surface. (c) For TST calculations the unit cell of a Cu (110) surface is divided into 1131 grid points (29 points in [110] and 39 points in [001] directions) with a step size of 0.1 Å. 3.597 x 2.543 (d) Representative free energy barrier for the diffusion of HtBDC molecule in [110] direction obtained from WHAM analysis (more simulation details in Appendix C). 47

Figure 21 Diffusion coefficient calculated using MD simulations in [001] and [110] directions: (a) molecular weight vs $D[001]$ (b) vdW energy vs $D[001]$ (c) elevation weighted density vs $D[001]$ (d) molecular weight vs $D[110]$ (e) vdW energy vs $D[110]$ (f) elevation weighted density vs $D[110]$ 49

Figure 22 (a) Elevation weighted density calculation schematic for HtBDC. Starting from the bottom most part of the molecule, number of atoms are counted with 0.05 Å discrete steps and using a cut-off radius of 1 Å. (b) Plot of number of atoms with increasing elevation from the surface, i.e. elevation weighted density curve. (c) Side view of VL molecule on metal surface. (d) Elevation weighted density curve for VL molecule..... 51

Figure 23 Transition state theory results: (a) molecular weight vs $D[001]$ (b) molecular weight vs free energy barrier in [001] direction (c) elevation weighted density vs. free energy barrier in [001] direction (d) molecular weight vs $D[110]$ (e) molecular weight vs. free energy barrier in [110] direction (e) elevation weighted density vs. free energy barrier in [110] direction. 53

Figure 24 Nanocar builder plug-in library: (a) wheel molecules; (b) chassis molecules. Using the plug-in users can select a chassis molecule, connect wheels, build a metal surface, and setup an MD simulation configuration for LAMMPS software. 57

Figure 25 A screenshot of the nanocar builder Avogadro 2 plug-in. After installation a “Nanocar” menu appears under the build option which can be used to add chassis molecules, connect wheel molecules, add a custom metal surface, and export LAMMPS configuration files..... 58

Figure 26 A nanocar molecule placed on a Au (110) surface built using the nanocar builder: (a) side view and (b) top view. Surface is approximately 5 nm x 5 nm and the nanocar molecule is approximately 1 nm in length. 59

Appendix Figure 1 Flowchart for IPMOF algorithm. Algorithm and its documentation with examples are provided here: <https://github.com/kbsezginel/IPMOF>. 62

Appendix Figure 2 Energy map schematic for MOF-5. Each red point represents grid points 1 Å apart in 3 dimensions. For each point potential energy is calculated using Lennard-Jones equation. 63

Appendix Figure 3 Energy map generation process for MOF-5. The potential energy increases from dark red to light red..... 64

Appendix Figure 4 Number of MOFs with given metal type observed in the database 65

Appendix Figure 5 Interpenetration process for two cubic MOFs. Blue framework is the passive framework and red framework is the active framework. The active framework is first rotated and then translated to next point depicted by the yellow point. 66

Appendix Figure 6 Algorithm parameters with values used in this study shown in parenthesis. Energy density limit of 0.1 K.kB/Å³ corresponds to 0.83144621 J/mol Å³.... 68

Appendix Figure 7 Example case for supercell parameters calculation..... 70

Appendix Figure 8 Analogy for MOF combination selection. The interpenetrating MOFs must have enough empty space in their unit cell so when they form a single unit cell there

is enough space for both frameworks. This can be imagined as filling two glasses of water into a single glass. In order to avoid overflowing the glasses should have enough empty space. 72

Appendix Figure 9 Number of MOF pairs in different steps of high-throughput screening 73

Appendix Figure 10 Analysis of candidate structures to find hetero-interpenetrated pairs (Starting from 1,045 candidates that passed the extended collision test, 90 of them were pairs of same MOFs according to their CSD reference codes [Step I]. From the remaining 955 candidates, pairs of MOFs that have different reference codes but are degenerate structures (922) are removed [Step II]. Remaining 33 candidates were inspected manually by comparing chemical formulas, crystallographic information and visually examining image renders of MOFs [Step III]. 15 more candidates were removed and 18 candidates were presented as hetero-interpenetrated candidate MOFs..... 74

Appendix Figure 11 Candidate interpenetrating MOF pairs identified using 30-degree rotations. Same pairs are also present in the list provided by Kwon et al.¹⁸⁸ CCDC¹⁰⁴ reference codes for the MOF pairs are given below structures separated by an underscore. The first name corresponds the gray framework and second name corresponds to the red framework. 80

Appendix Figure 12 Hetero-interpenetration test for COGCOS⁶⁷ (a) Structure comparison (b) XRD pattern comparison 81

Appendix Figure 13 Hetero-interpenetration test for ETAXAS⁷² (a) Structure comparison (b) XRD pattern comparison 81

**Appendix Figure 14 Hetero-interpenetration test for TIVYED⁷⁴ (a) Structure comparison
(b) XRD pattern comparison 82**

**Appendix Figure 15 Hetero-interpenetration test for PELQII⁶⁸ (a) Structure comparison (b)
XRD pattern comparison 82**

**Appendix Figure 16 Hetero-interpenetration test for UNAZIT⁷¹ (a) Structure comparison
(b) XRD pattern comparison 82**

**Appendix Figure 17 Bonded interactions for the idealized porous framework. Morse
potential were used to model bonded interactions for the two types of bonds defined
(depicted in green and yellow). The Morse potential parameters for these bonds are given.
..... 84**

**Appendix Figure 18 Lennard-Jones potential for a) varying σ values and ϵ : 50 K.kB b)
varying ϵ values for σ : 3.5 Å c) varying ϵ values for σ : 4.5 Å. In all plots the variable
increases from red to blue as shown in legends..... 85**

**Appendix Figure 19 Coupling constant profile for different coupling constant limits. a) ϵ
coupling constant ($\gamma\epsilon$) profile for changing limits ($\gamma\epsilon_{max}$). b) σ coupling constant ($\gamma\sigma$)
profile for changing limits ($\gamma\sigma_{max}$)..... 89**

**Appendix Figure 20 Thermal conductivity prediction error (%) for interpenetrated
framework using the relationship in Eq. B-1 for a range of σ ($\gamma\sigma^{max}$) and ϵ ($\gamma\epsilon^{max}$) coupling
constant limits. Minimum average error (7.8 %) was found for $\gamma\sigma_{max}$: 0.498 and $\gamma\epsilon_{max}$:
0.889..... 89**

**Appendix Figure 21 Interpenetrated idealized MOF structure where entangled frameworks
are colored in blue and red. The zoomed in single unit cell shows atoms used to calculate
the relative distance between frameworks in 2D. In 3D the distance between the red atom**

in the middle and all 8 corner atoms, identical to a body centered cubic configuration, is calculated for each 1000 timesteps of MD trajectories..... 90

Appendix Figure 22 2D histograms for thermodynamic data recorded during framework interaction parametric screening. All energy in kcal/mol..... 92

Appendix Figure 23 2D histograms for change in (a) thermal conductivity (W/mK) and (b) simulated box volume to idealized box volume ratio (%) as a function of spring constants for two-body bonded and three-body angular harmonic potentials. 93

Appendix Figure 24 2D histograms for change in thermal conductivity (W/mK) due to (a) bonds and (b) angles as a function of spring constants for two-body bonded (x-axis) and three-body angular (y-axis) harmonic potentials..... 94

Appendix Figure 25 (a) 2D histogram for the thermal conductivity convergence as a function of spring constants for two-body bonded (x-axis) and three-body angular (y-axis) harmonic potentials. (b) Average thermal conductivity vs simulation time for the idealized structure with a bonded potential spring constant of 6 kcal/mol and angular potential spring constant of 5 kcal/mol. “*k*” stands for overall thermal conductivity, “*k_bond*” and “*k_angle*” are the contributions of bonded and angular potentials to the thermal conductivity, respectively. “*k_est*” is the estimated thermal conductivity (0.99 kcal/mol) calculated by averaging the last 150 ps of the time dependent thermal conductivity curve. 95

Appendix Figure 26 (a) Mean squared displacement (MSD) vs time delta (τ) for 20 molecular dynamics simulations in [110] direction for HtBDC molecule. (b) Average of all MSD vs τ curves and a linear fit between 1.5 ns – 5.0 ns to calculate self-diffusion coefficient. The R-squared value for the fit as well as the diffusion coefficient are given in the legend.. 100

Appendix Figure 27 (a) Averaged mean squared displacement (MSD) vs time delta (τ) for 20 molecular dynamics simulations in [110] direction. A linear fit between 1.5 ns – 5.0 ns was used to calculate self-diffusion coefficient. The R-squared value for the fit as well as the diffusion coefficients are given in the legend and the molecule names are given in the title. 101

Appendix Figure 28 (a) Averaged mean squared displacement (MSD) vs time delta (τ) for 20 molecular dynamics simulations in [001] direction. A linear fit between 1.5 ns – 5.0 ns was used to calculate self-diffusion coefficient. The R-squared value for the fit as well as the diffusion coefficients are given in the legend and the molecule names are given in the title. 102

Appendix Figure 29 Free energy barriers and self-diffusion coefficients for each molecule and each umbrella sampling paths for the two primary crystallographic directions. Red and blue points correspond to results for [001], and [110] directions, respectively. The dashed line represents the Boltzmann averaged value for the overall diffusion in that direction. The molecule name, crystallographic direction and variable names are given in the title..... 105

Appendix Figure 30 Elevation weighted density curves for the nine molecules used in this study 106

Preface

First of all, I would like to thank Dr. Chris Wilmer who was not just a PhD advisor but an invaluable mentor to me. Chris has always been supportive and he has given me the freedom to pursue various projects without objection. He is one of the smartest people I know and his big picture perspective has truly helped me grow intellectually. I have learned so much from him, not just about chemical engineering but about scientific visualization, bitcoin, making good career decisions, and much more. I think deciding to come to University of Pittsburgh to join his research group was one of the best decisions I made and I am very grateful to him for making my PhD education very fruitful and a much better experience than I could imagine. And secondly, I attribute special thanks to my committee members for their valuable time and contribution.

This would not have been possible without the support of my fellow Wilmer Lab members; thank you to Alec, Jenna, Paul, Brian, and Hasan. I am grateful for the positive and warm environment you all created and for your willingness to always help. I would like to thank all my dear friends, especially Yasemin Başdoğan for invaluable scientific discussions and making Pittsburgh home. She has been always there for me both as a colleague and as a friend and it wouldn't have been possible to write this thesis without her support. Thank you to my family and my parents for always encouraging me and supporting me with every way possible. Especially, I would also like to thank my sister and best friend Dilay, for always being there for me.

This work started with an interest in designing a complex class of materials (interpenetrated metal organic frameworks) as it was a challenging and novel task according to both Chris and I. Eventually, we ended up working on molecular race cars and doing many other interesting and cool science in the process. I am proud to have worked on so many challenging and interesting

scientific problems, and thankful for Chris for always prioritizing the novelty of research instead of working on more established and easily fundable problems.

This work includes three peer-reviewed articles, published in *Crystal Engineering Communications*, *Chemical Science*, and *Materials System Design and Engineering* with another one submitted to *Journal of Physical Chemistry C*. Additionally, I have worked on several other research projects that are not mentioned in this dissertation. These include one peer-reviewed article published in *Advanced Functional Materials*, and three others that are going to be submitted to other peer-reviewed articles in the near future.

Furthermore, work in this dissertation required a fair amount of software development. All software used in this work are made available on GitHub with open-source licenses. A list of software projects with summaries and links are provided in Appendix D.

1.0 A Brief History of Computational Materials Design for Molecular Machinery

1.1 An Introduction to Molecular Machines

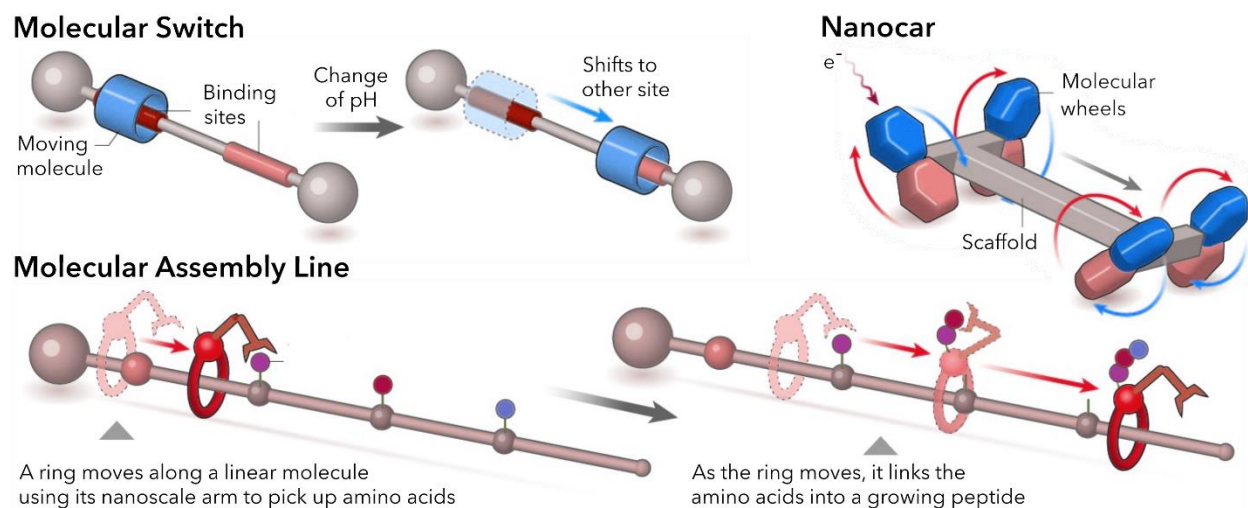


Figure 1 Examples of artificial molecular machines.⁵

How can we design the world's smallest machines—machines that operate at an extraordinarily small scale with molecular moving parts?¹ Just as experimental research on electric motors and combustion engines by nineteenth-century scientists led to revolutionary technologies, exploration of molecular motors,² actuators,³ logic gates,⁴ and other molecular machines could lead to similarly transformative discoveries and innovations in the future. However, at present, the focus of computational chemistry software is on exploring various molecular phenomena, not on designing new molecular machines. Whereas computer-aided design (CAD) software has become mainstream in the design of new cars, airplanes, and other “macro” machines, CAD tools that can design molecular machines have yet to be developed. Developing comprehensive software for this

purpose might seem daunting, even impossible, but a promising starting point is to focus on the design of molecular *components* that can eventually be incorporated into molecular *machines*.

The molecular machines of Nature have been a constant source of inspiration to the chemists which allowed them to synthesize molecular systems that can produce a type of mechanical motion from various external stimuli (see Figure 1).⁶ One of the important processes mastered by biological molecular machines is transporting molecular cargo: enzyme molecules are moved along protein filament tracks converting chemical energy into mechanical work.⁷ This requires directed motion of molecules along a track or a surface which remains extremely challenging because it either requires a stimuli that modulates the interaction of the molecule with the surface or a considerably anisotropic interaction of the molecule with the surface that result in a preferred directional motion along the surface.⁸ For this purpose, nanocars have been proposed as carrier molecules that can be used to transport small molecules or as building blocks to enable bottom-up construction of miniaturized machinery.⁹ Nanocars are single molecule vehicles that resemble macroscopic automobiles and they provide a starting point to explore more sophisticated molecular systems with directionally controlled motion (see Figure 2).⁸

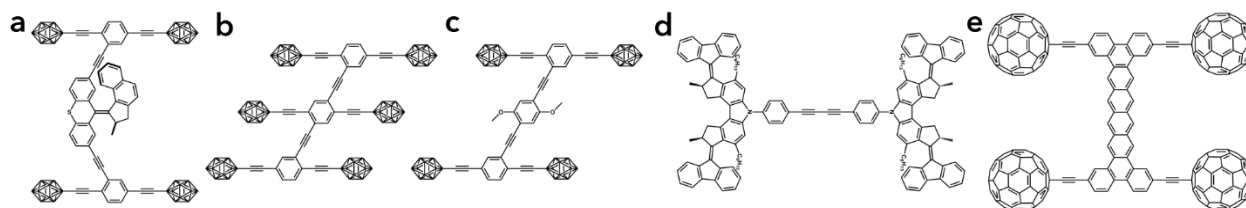


Figure 2 Examples of nanocars. (a) Light-driven motorized nanocar.¹⁰ Carborane-wheeled nanocars with (b) six and (c) four wheels.¹¹ (d) Electrically driven nanocar with motorized wheels.⁸ (e) Fullerene wheeled nanocar (hypothetical).¹²

As with macroscopic machines, molecular machines are composed of both dynamic and static molecular structures that work together (e.g. kinesin motor proteins walking on microtubules). Consequently, development of new molecular machinery requires design of cooperating static and dynamic molecular structures. One class of solid-state material that has received considerable interest is metal-organic frameworks (MOFs) because of the high variety of structures that can be achieved by the design of metal clusters and organic linkers (see Figure 3).¹³⁻¹⁷ A wide variety of available building blocks enables the synthesis of many different MOFs with fascinating architectures and provides the opportunity for properties by design when the underlying principles are well understood.¹⁸ As a result, MOFs are promising functional materials and they can be diverse and valuable *parts* for molecular machinery.

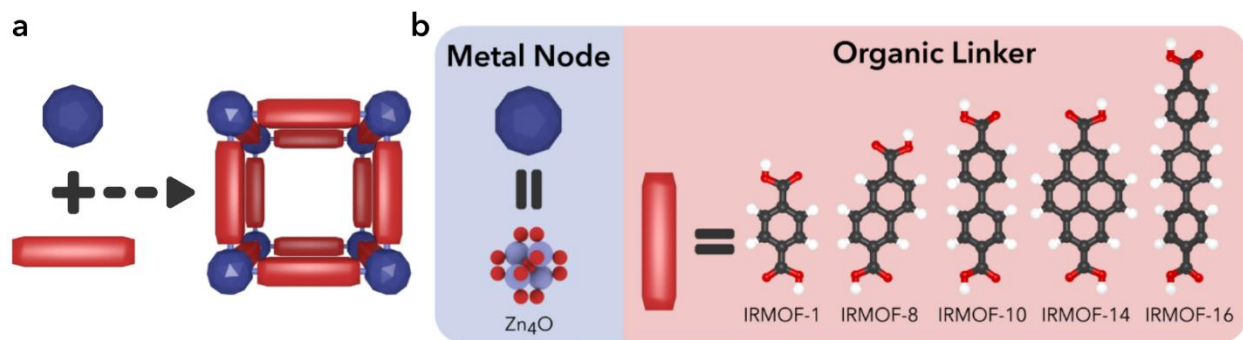


Figure 3 Self-assembly of metal-organic frameworks. (a) Building blocks are self-assembled to form porous crystals. (b) A wide variety of metal nodes and organic linkers can be used as building blocks to construct MOFs with different geometries.

1.2 Artificial Molecular Machines

Over billion years of evolution Nature mastered molecular nanotechnology, manipulating atoms and molecules with high precision. This allowed the evolution of complex molecular machines that can transfer chemical energy into mechanical energy and do continuous work to sustain vital cell functions.¹⁹ Among them are machines that perform tasks such as protein synthesis (ribosomes), gene replication (DNA and RNA polymerases), transporting molecular cargo (kinesin and dynein), and locomotion (flagella).¹⁹ For that reason, bridging the gap between macroscopic machines and synthetic molecular systems suggests great rewards.²⁰

Inspired by the molecular machines of Nature, scientists have been exploring molecular motors,^{2,21,22} switches,^{23,24} shuttles,^{25,26} nanocars,^{8–10} assemblers,^{27–29} logic gates,^{30,31} and tweezers.^{32,33} In order to produce mechanical motion, an energy input is required as a driving force. Many different external stimuli have been used including light,^{10,34–36} pH,^{37–39} redox,^{40,41} solvents,⁴² and heat.^{25,43} However, in order to extract useful work at this scale, the thermal motion of the submolecular components needs to be restricted or somehow exploited. Moreover, for most applications mechanical motion of individual components needs to be scaled to the macroscopic level, requiring collective work. One crucial difference from macroscopic machines is that molecular machines require a bottom-up design approach, which is especially challenging. However, computational tools enable us to parametrically search for molecular components that work well together, allowing the design of AMMs for targeted applications. Utilizing computational tools would allow us to optimize the design of AMMs and provide guidance to experimental chemists.

1.2.1 Rotaxanes

Mechanically interlocked molecules (such as catenanes, rotaxanes) are frequently used as artificial molecular machines exploiting the mechanical bonds in the structure.⁴⁴ This mechanical bond restricts the freedom of motion to a well-defined pathway which introduces directionality to the motion. Rotaxane motion can be activated by different stimuli such as light, pH change or heat. As the energy barrier is lowered the interlocking structures switch between different configurations (isomers).

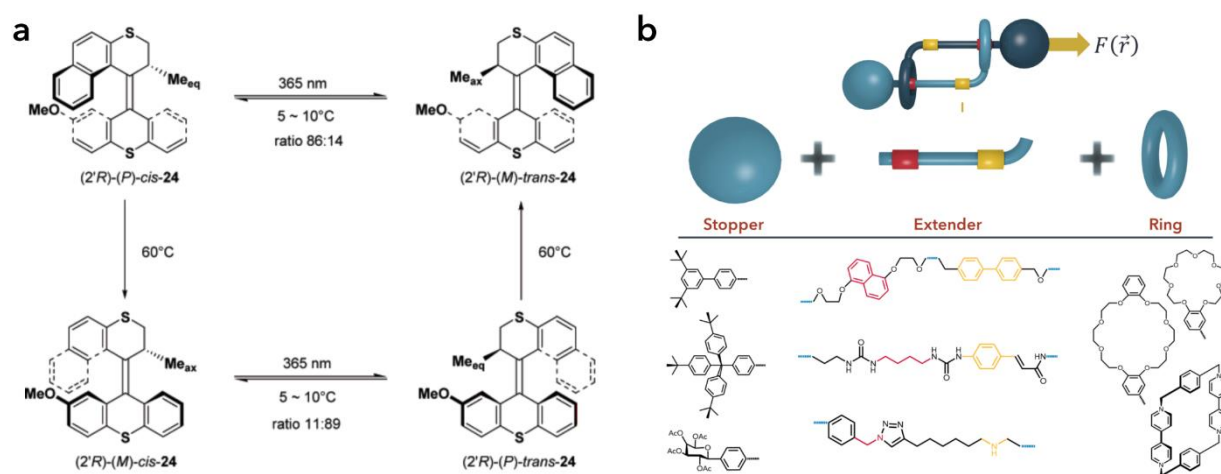


Figure 4 Molecular machine structures. (a) Feringa second generation molecular motor with a (2'R)-methyl-2,3-dihydronephthiopyran propeller and a 2-methoxythioxanthene stator. Rotation around the double bond is achieved with photochemical and thermal isomerization (b) Daisy chain rotaxane model with building blocks deconstructed as stopper, extender, and ring. Different molecular structures are shown for each building block. By carefully designing the molecular structure of the building blocks properties of the rotaxane such as force needed to switch, stimulus, and speed can be tuned.

A daisy chained rotaxane model is given in Figure 4b with building blocks deconstructed as stopper, extender, and ring. As seen in the figure, the extender part has two low energy states

shown with red and yellow. By providing energy to the system, rotaxane can be switched between these two states which can be used to apply force. Different molecular structures are shown in the figure for each building block. By carefully designing the molecular structure of the building blocks properties of the rotaxane such as force, stimulus, and switching speed can be tuned. Therefore, rotaxanes have been considered as potential building blocks for artificial muscles.⁴⁵⁻⁴⁷ Previously, Jang and co-workers have performed a series of studies to investigate the surface coverage and collective motion of monolayers of bistable [2]rotaxanes on Au (111) surface^{48,49} and at the air/water interface.⁵⁰ In another study Kim et al. investigated the free energy barrier for the shuttling of the cyclophane cyclobis(paraquat-p-phenylene) (CBPQT⁴⁺) ring between tetrathiafulvalene (TTF) and 1,5-dioxynaphthalene (DNP) stations of a bistable [2]rotaxane.⁵¹ They predicted the time limiting step of the switch to be 2.1 s which was found to be compatible with experiments.

1.2.2 Molecular Motors

Molecular motors are molecules that are capable of rotary motion around a single⁵² or double bond.^{2,21,22} As seen in Figure 4a, the rotation around the double bond can be controlled by photochemical and thermal isomerization. It was shown that the rotational direction and speed of the molecular motor can be tuned by careful design of the structure.⁵³ Inspired by this study, Bo Durbeej and co-workers have performed outstanding work to understand the rotation mechanism of molecular motors and they proposed new designs to accelerate the thermal steps of overcrowded-alkene motors using density functional theory and non-adiabatic molecular dynamics calculations.⁵⁴⁻⁶⁰

1.2.3 Nanocars

Nanocars are large organic molecules generally made up of a “chassis” with spacer functional groups (“wheels”) attached to it to keep it away from the surface and minimize surface adhesion (see Figure 2 for different nanocar structures). Most nanocars are static molecules and their motion is initiated by thermal activation or energizing the molecule with a scanning tunneling microscope (STM) tip.⁹ The molecular design of the nanocar is what determines the nature of its motion. Initially nanocars were developed to better understand diffusion of fullerenes on metal surfaces. Interest in nanocar research grew to understand and control molecular motion on surfaces. Even dynamic nanocars with rotating wheels have been designed to achieve unidirectional motion. This design employed molecular motors as wheels and the rotation of the wheels was controlled by energizing the molecule with an STM tip, prompting isomerization of the double bonds in its molecular motor “wheels.” With each shot from the STM, the molecule was shown to move ~0.6 nm.⁸

Alexey V. Akimov and co-workers have performed several studies to understand the motion of nanocars on metal surfaces using rigid body molecular dynamics.^{12,61–63} They performed the first modeling study in collaboration with James M. Tour to provide theoretical insights to thermally initiated motion of nanocars.¹² They employed a simplified nanocar design (see Figure 2e) and divided the molecule into rigid fragments as four wheels and a chassis. They showed that, in agreement with the experimental results, the nanocar mobility was initiated at temperatures higher than 400 K and they observed rotational motion of the wheels at 500 K. Moreover, they suggested that the diffusion strongly depends on the structure and periodic properties of the surface. In a later study they investigated the effect of an electric field (e.g. created by the STM tip) on the diffusion of a nanocar using the same structure.⁶³ In order to mimic the electric field,

they employed a custom charge transfer method (developed in a previous study⁶²) and performed a series of rigid-body molecular dynamics simulations. They found that external electric fields can be used to drive nonpolar nanocars unidirectionally and rolling mechanism of the wheels is the dominant factor in the nanocar surface diffusion as opposed to simple hopping and sliding mechanism. Ganji et al. studied the motion of a carborane-wheeled nanocar on graphene/graphyne surfaces using density functional theory.⁶⁴ They calculated the activation energy for the motion of the four wheeled nanocar as 17.06 and 4.38 kcal/mol for graphene and graphyne surfaces, respectively. Even though these studies provide very important insights to the motion of nanocars and the interactions between the nanocar and the surface, they do not present kinetic information about the diffusion process. Therefore, these methods cannot be used directly to estimate the timescale of diffusion. Moreover, these studies focused on elucidating the motion of nanocars instead of designing new nanocars with improved directionality and diffusion.

1.2.4 Metal-Organic Frameworks

As discussed in section 1.1, development of new molecular machinery requires design of cooperating static and dynamic molecular structures. Metal organic frameworks (MOFs) are promising candidates to be included in molecular machines or used as platforms to organize them thanks to their high geometric and chemical variety. They are formed by the self-assembly of metal clusters and organic linkers and by carefully designing these building MOFs with a wide variety of structures can be synthesized. Stephen J. Loeb and co-workers demonstrated that even molecular shuttles (based on [2]rotaxane) can be incorporated in MOFs and the interlocked macrocyclic wheel can undergo repetitive, translational motion along a rigid track built between two struts of the framework.⁶⁵ This entanglement of molecular structures or frameworks is one of

the common methods of achieving high structural complexity in MOFs. In cases where the dimensionality of the structure increases, this phenomena is referred as polycatenation whereas if the dimensionality of the final architecture remains the same, it is called interpenetration.⁶⁶ Interpenetration is generally observed in MOFs with large pores as the entanglement of multiple frameworks becomes energetically more favorable and results in a more stable overall structure. Remarkably, several hetero-interpenetrating and polycatenated MOFs, which contain frameworks with different shape, topology, and chemical composition, have been synthesized already^{67–77}; some even containing three distinct entangled frameworks.^{78,79} Figure 5a and 5b are two examples of hetero-interpenetration, Fig 5c is an example of polycatenation of 2D nets, and Figure 5d is a 3D + 1D polycatenation (For more examples, the reader is referred to Refs.^{80–83}). For homo-interpenetration, up to 54-fold interpenetration has been reported as well.⁸⁴

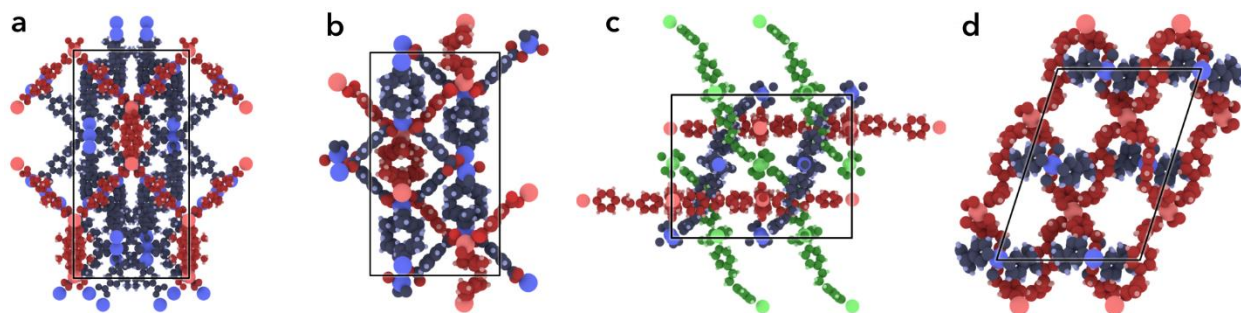


Figure 5 Hetero-interpenetrating and polycatenated metal-organic frameworks with entangled frameworks colored individually. CCDC reference codes and associated publications are provided as follows (a) WEBZEK⁶⁹ (b) COGCOS⁶⁷ (c) EJAXOC⁷⁸ (d) ATEYED.⁷⁵

The formation, or not, of interpenetrated networks can often be controlled either by rational geometric design of the structure or manipulation of experimental conditions. Deliberate

modification of organic ligands,⁸⁵ using infinite secondary building units^{86,87} and choosing solvents with appropriate molecular size⁸⁸ have been used as geometrical restraints to control interpenetration whereas manipulating reactant concentration and reaction temperature were used to control interpenetration by regulating reaction kinetics.⁸⁹ Additionally, reversible interpenetration control was achieved by ligand removal and addition⁹⁰ and anisotropic entanglement was realized by partial interpenetration.⁹¹ Using these experimental methods, advanced control of final architecture can be achieved by controlling degree of interpenetration^{92,93}, reaching up to 54-fold interpenetration⁸⁴, as well as modifying interpenetration distance to design minimally interpenetrating (interweaving) MOFs.⁹⁴ Even though several methods have been developed to computationally design MOFs, designing interpenetrated MOFs, particularly hetero-interpenetrated ones, is challenging.⁹⁵⁻⁹⁷

In this work we aim to develop computational methods that will aid the design of AMMs with targeted geometry and functionality. This includes molecular design and construction of AMMs as well as developing/identifying methods to study their performance. More specifically we aim to develop computational methods to design static and dynamic molecular architectures: MOFs and nanocars. Initially we aim to develop a computational method to design interpenetrated MOFs and study thermal transport properties of interpenetrated MOFs as well as flexible MOFs. Then, we aim to investigate different modelling strategies to estimate diffusion of nanocars on metal surfaces. Finally, we aim to develop computational tools to build hypothetical nanocars and assess their surface diffusion performances. These studies, and the tools developed, will collectively help to push the frontier of knowledge (even if incrementally) towards the eventual building of useful AMMs.

2.0 Discovery of Hypothetical Hetero-Interpenetrated MOFs with Arbitrarily Dissimilar Topologies and Unit Cell Shapes

Interpenetration is the entanglement of multiple frameworks and it is commonly observed as homo-interpenetration which is the entanglement of identical metal organic frameworks (MOFs). Hetero-interpenetration, where two (or more) distinct frameworks entangle with one another, is much rarer, although several cases have been observed in recent years. Interpenetration of either kind (hetero or homo) greatly affects the pore characteristics (size, shape, environment, dimensionality) and consequently the functionality/performance of the material. Given their complex nature, designing interpenetrated MOFs, particularly hetero-interpenetrated ones, is challenging. By combining experimental techniques to control interpenetration and computational methods to identify candidate structures, we may soon be able to engineer materials with multiple interpenetrating frameworks with targeted functionalities.

In this work, we describe an algorithm that can quickly test whether two given crystal structures have the potential to interpenetrate with one another. The algorithm is designed to work with any pair of crystal structures, regardless of the shape or size of their unit cells, and judges whether they can plausibly interpenetrate based on simple energetic calculations. Moreover, the algorithm tests different orientations and relative positions of the frameworks. Using this algorithm, we screened the CoRE database⁹⁸, supplemented with an additional 1005 MOFs, for a total of 6014 frameworks, which meant testing 4.3 million pairs. From those, the program outputted 1045 pairs that had a high likelihood of being hetero-interpenetrated structures, from which we validated 18 candidates by manual inspection. The resulting structures, along with the source code for the algorithm, are provided in a GitHub repository.⁹⁹

2.1 Methodology

Algorithm Description. To test whether two given MOFs can interpenetrate with each other, we developed a method that rapidly tries different relative orientations of the two frameworks and reports the *plausibly* energetically favorable ones. It is important to remark that it is much easier to identify *impossible* orientations (where frameworks collide with each other), than to identify cases where interpenetration would truly be favorable. We do not account for entropy, solvent effects, framework flexing, etc. Our main aim was to apply this method to screening large databases to identify candidates for hetero-interpenetration, after which more sophisticated modeling, or experimentation, could be used. Since we expected most pairs of MOFs to have only (highly) unfavorable energetics for interpenetration, it would have been premature and inefficient to apply higher accuracy energetic calculations at this stage of the discovery process.

The method tries many different orientations of two given MOFs by performing rotation and translation operations according to user configurable parameters. After an orientation is chosen, its energetic favorability is calculated based on the pairwise interactions between each atom on one framework with every atom on the other framework. For efficiency, we employ an energy map approach (see details below) that allows us to avoid repeatedly calculating interatomic distances. Overall, our algorithm can rapidly detect cases where interpenetration is impossible and suggest ones where it may be plausible. More detailed description and a flowchart of the algorithm are provided in Appendix A1.

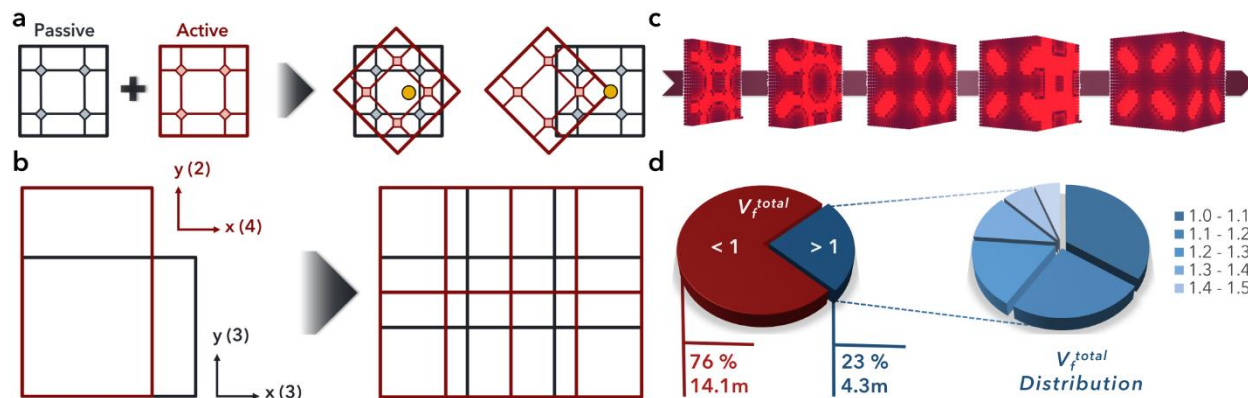


Figure 6 Interpenetration discovery algorithm description and candidate interpenetrated MOF total void fraction distribution. a) Energy map generation for MOF-5. Grid points are colored from light to dark red according to calculated energy values. b) Single unit-cell interpenetration test procedure for two given MOFs.

First, the unit cells are aligned. Second, one of the unit cells is rotated and then translated to a selected position (represented by a yellow point). For this selected orientation, energy values for each atom in the red unit cell are added to obtain the energy density. c) Simplified schematic for combining two unit cells into a supercell. The 2D supercell can be obtained by repeating the red unit cell 2 times in y and 4 times in x dimensions and repeating blue unit cell 3 times in both dimensions. d) Total void fraction (V_f^{total}) distribution for MOF combinations: selecting combinations with $V_f^{total} > 1$ (corresponding to ~4.28 million MOF combinations) and V_f^{total} distribution among selected combinations (ordered with increasing void fraction from dark to light blue). More information can be found in Appendix A1.

Energy Map Generation. An energy map is a regular grid of points representing the potential energy inside the crystal unit cell from the perspective of an atom being inserted into that space (see Figure 6c). In our method, the potential energy for each point in the grid is calculated using a Lennard-Jones (LJ) potential (Eq. 2-1)¹⁰⁰ with parameters taken from the Universal Force Field (UFF).¹⁰¹ Lorentz-Berthelot mixing rules were used for atoms of different types and a cut-off radius for interactions was set to 12 Å.

$$V_{LJ} = 4\varepsilon \left[\left(\frac{\sigma}{r} \right)^{12} - \left(\frac{\sigma}{r} \right)^6 \right] \quad 2-1$$

When an energy value is needed at a position that does not fall exactly on a grid point in the energy map, which is the usual case, interpolation is used. We used the trilinear interpolation technique, which has been commonly used by others.^{102,103}

Single Unit-cell Interpenetration Test. After generating the energy maps, the next step of the algorithm is to select an initial relative orientation for the unit cells of two given MOFs. We call one *passive* and the other *active* (shown as blue and red in Figure 6a, respectively). The active unit cell is first aligned with the passive unit cell along their respective \vec{a} vectors (using the conventional \vec{a} , \vec{b} , \vec{c} , crystallographic vector notation). The active unit cell is then rotated around the global x , y , and z axes by increments defined by the user. Then the active unit cell is translated in x , y , and z directions, also by increments defined by the user, within the passive unit cell. For each tested orientation, an energy density, ρ_{energy} , is calculated according to Eq. 2-2,

$$\rho_{energy} = \frac{\sum_{i=0}^{N_p} \sum_{j=0}^{N_a} V_{LJ}(i, j)}{V_{cell}} \quad 2-2$$

where N_p and N_a are the number of atoms in the passive and active MOFs, i and j are atom indices for the passive and active MOFs, V_{LJ} is the interatomic LJ potential energy, and V_{cell} is the unit cell volume in \AA^3 . The energy density is calculated by adding energy values for the insertion of each atom in the active unit cell to the passive unit cell. The energy values are directly obtained from the previously calculated energy map for the passive unit cell. As energy values for each

atom in the active unit cell are added and divided by unit cell volume to calculate energy density, the energy density is checked to see whether it exceeds a threshold value. If the threshold is exceeded, the currently tested orientation is rejected. If the energy density stays below the threshold until all the atoms are added, the orientation is saved for further consideration. More information about the selection of the threshold value is provided in Appendix A1.

Multiple Unit-cell Collision Test. For each saved orientation, the energy density is then recalculated by extending both unit cells up to the boundaries of a sphere with radius of 50 Å. This is performed to make sure that differences in repeating patterns of the unit cells do not cause overlap when they are extended multiple times. However, this is a computationally expensive calculation; therefore, it is only performed for the candidates that pass the single unit-cell test. It is possible, in principle, for collisions to occur outside of the sphere radius considered; however, this test narrows down the remaining candidates significantly (see Figure 8a).

Determining Supercell Dimensions and Exporting Hypothetical Interpenetrated Crystal Structures. When the interpenetrating structures have different unit cell shapes, a combined unit cell, which we refer to as a supercell, needs to be determined (see Figure 6b). This combined unit cell allows both structures to repeat according to their symmetry. In order to find the supercell parameters, first the $\vec{a} + \vec{b} + \vec{c}$ vectors of the active unit cell are converted to fractional coordinates with respect to the crystallographic vectors of the passive unit cell. Then, for each dimension, a least common multiple (*LCM*) is calculated to determine packing coefficients for the passive unit cell. The tool allows for minor linear distortions to be applied to one of the unit cells to reduce the size of the supercell, which we typically allowed to go up to 1% (but can be configured by the user to be higher or lower). Multiplying the packing coefficients with the fractional coordinates of active unit cell gives the number of repeat units for the active unit cell. Converting either of these

new parameters to the Cartesian coordinate system would yield the unit cell parameters of the supercell. A simplified equation for the procedure is provided below,

$$[\vec{a} + \vec{b} + \vec{c}]_c = [LCM(\overrightarrow{a_{2,f}}) + LCM(\overrightarrow{b_{2,f}}) + LCM(\overrightarrow{c_{2,f}})]_c \quad \mathbf{2-3}$$

where subscripts c and f represent Cartesian and fractional coordinates, respectively, and subscript 2 indicates parameters for the active unit cell. More information about supercell calculation including an example case can be found in Appendix A2.

High-throughput Screening. For high-throughput screening, the CoRE MOF database created by Chung and co-workers⁹⁸ has been used. This database was created by analyzing the CCDC database¹⁰⁴ to select MOFs and making them suitable for molecular simulations. This included removing solvent molecules and resolving issues with partially occupied atoms when necessary. In addition to the structures in that database, 1005 additional MOFs were provided to us by Dr. Yongchul G. Chung. The additional MOF structure files were obtained using the same methodology as used for the original CoRE MOF database. The database only consists of 3D MOFs therefore only 3D + 3D interpenetrated structures are considered in this study. However, our algorithm can test interpenetration/catenation of structures with any given dimensionality.

Selecting MOF Combinations. To eliminate MOF combinations that are physically incapable of interpenetration based purely on the fraction of space each framework occupies, only MOF pairs whose individual void fractions sum to greater than one were considered (when the sum is less than one, we know with certainty that there is not enough empty space for one MOF to accommodate the other). See Figure 6d.

Other Screening Parameters. For the screening of the MOF database, we selected a set of algorithm parameters that we estimated would yield a high enough number of successful trials in a reasonable amount of time. Twenty-four different rotational orientations were considered per pair of MOFs for each position in the energy grid. The orientations were determined as all the possible 90-degree rotations around x , y , and z axes. To limit the memory requirements for the energy maps, we used UFF parameters for C, H, O, and N atoms and the most common 7 metal atoms in the database, whereas for the rest of the atoms, dummy parameters were used. In theory, by using our tool, it is possible to discover interpenetrated structures from the CoRE MOF database that were not found in this reported screening run. The screening study here was performed to make an initial estimate for possible interpenetrations rather than rigorously exploring every possible orientation for every pair of MOFs considered. More information about MOF combination selection and analysis of candidate structures are given in Appendix A3.

2.2 Results and Discussion

Experimental Comparison. First, we validated the algorithm by “predicting” experimentally synthesized interpenetrated structures. For that purpose, we considered one homo-interpenetration case and one hetero-interpenetration case. MOF-5 was selected as a test case for validating the algorithm in predicting simple homo-interpenetration. To test the algorithm, we used a non-interpenetrated MOF-5 structure as input and compared the output structure with the experimentally synthesized interpenetrated MOF-5.

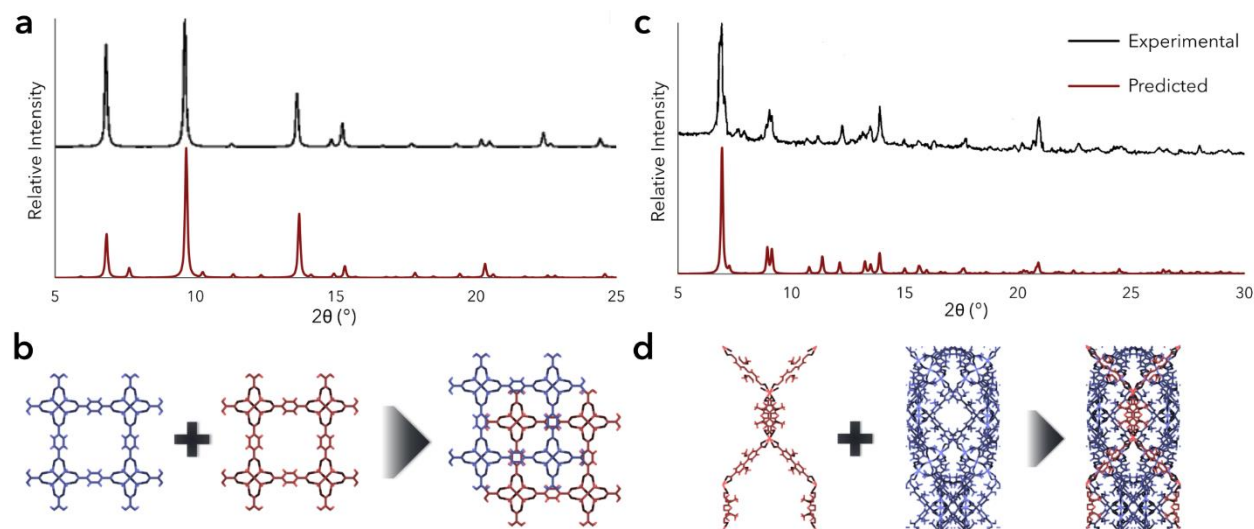


Figure 7 Experimental comparison of predicted MOFs. **a)** Comparison of XRD patterns of predicted interpenetrated MOF-5 and experimentally synthesized MOF-5; **(b)** schematic for interpenetration of MOF-5; **(c)** Comparison of XRD patterns of predicted interpenetrated WEBZEK and experimentally synthesized WEBZEK; **(d)** schematic for interpenetration of WEBZEK.

As seen in Figure 7a, the x-ray diffraction patterns for the predicted and experimental structure fit nearly perfectly. Moreover, the surface area for the predicted structure was calculated as 769.5 m²/g, which is in the range of experimentally reported values between 600 – 1300 m²/g.¹⁰⁵ We also tested the algorithm for a 3D/3D hetero-interpenetrated tetragonal Cd-MOF⁶⁹ and observed a good match between predicted and experimental x-ray patterns as presented in Figure 7c. Comparisons with other MOFs are provided in Appendix A4.

High-throughput Screening. Initially, energy maps were generated for all the 6014 MOFs, and then single-unit cell interpenetration tests were performed for the selected 4.3 million MOF pairs. Among these, 262,664 of the pairs resulted in favorable interpenetrations. These pairs were then subjected to multiple unit-cell collision tests which narrowed down the combinations to 1045 (see Figure 8a). The resulting 1045 MOFs were examined in detail, and it was found out that all of the pairs were formed from a set of 113 MOFs. In this set, 46 of the structures turned out to be

MOF-5 degenerate structures that had different CCDC codes. By excluding pairs of degenerate MOFs (which consisted mainly of MOF-5), only 33 MOF pairs remained as actual hetero-interpenetrated candidates. Among these pairs, 18 of them were confirmed as unique hetero-interpenetrated structures by visual inspection (see Figure 8b). All structures can be accessed from Ref¹⁰⁶.

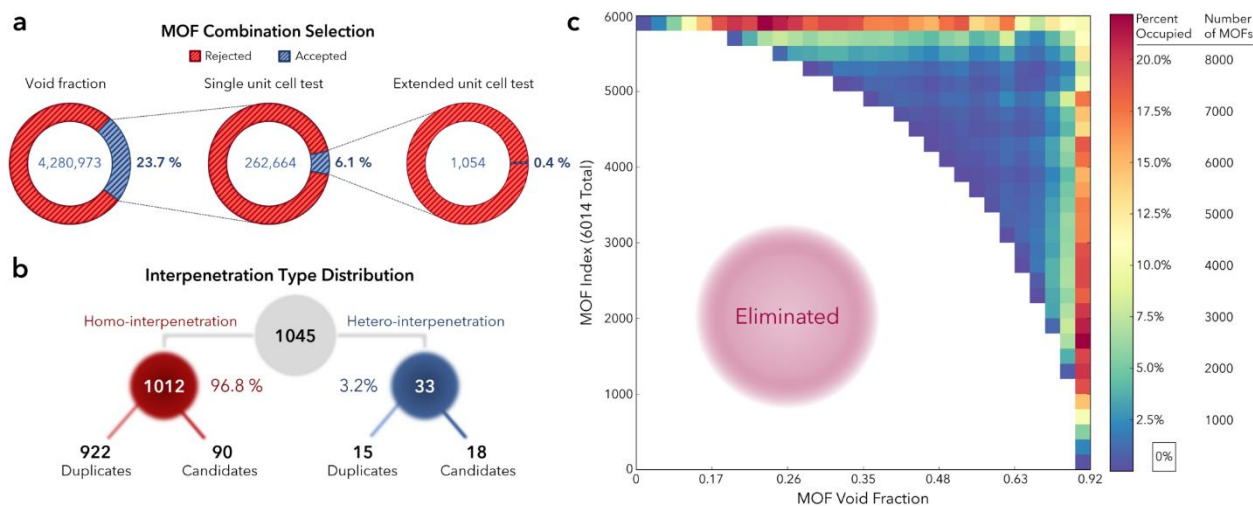


Figure 8 Number of MOF combinations selected at different steps in the analysis: (a) percentage of MOF combinations selected with respect to previous data set; (b) percentage distribution of homo and hetero interpenetration in MOF combinations that passed the extended unit cell test (here degenerate structures with different names are not considered as homo-interpenetration); (c) Overall structure discovery distribution of MOF combinations given in both axes with increasing void fraction (V_{ftotal}). Crystallographic information files (cif) for all structures can be accessed from IPMOF GitHub repository.⁹⁹

In order to get an overall picture of pairs that yielded one or more interpenetration configurations (262,664 pairs total), a histogram was created (Figure 8c). In both x and y axes, MOFs have been sorted by increasing void fraction and bins were colored according to number of pairs with one or more configurations. The white area corresponds to the region of pairs that were eliminated due to lack of empty space in the frameworks. The circular boundary between the white

and colored regions represents where $V_{f,1} + V_{f,2} = 1$. As expected, the increase in void fraction of both MOFs tends to increase the possibility of interpenetration.

Table 1 Structural and crystallographic information for six hetero-interpenetrating MOF candidates.

MOF Pair	Formula	LCM ^a	Distortion ^b	SupercellParameters ^c	V _f ^d		
1	AXUBAW (IRMOF-18)	C ₇₂ H ₇₂ O ₂₆ Zn ₈	[1, 1, 1]	1.11 %	[18.112, 18.112, 18.112]	[60, 60, 60]	0.29
	NODTIL (MOF-5)	C ₄₈ H ₂₄ O ₂₆ Zn ₈	[1, 1, 1]				
2	IZEPAF	C ₂₈₈ H ₁₄₄ O ₁₅₆ Cr ₃₆	[43, 43, 43]	2.89 %	[1226.36, 1226.36, 1226.36]	[90, 90, 90]	0.68
	WUHDAG (NU-1104)	C ₂₄₀ H ₁₃₀ N ₁₂ O ₃₂ Zr ₆	[42, 42, 42]				
3	UQOFOX (PCN-528)	C ₉₆ H ₅₆ N ₄₀ Mn ₆	[23, 1, 1]	1.58 %	[47.815, 20.550, 20.550]	[90, 90, 90]	0.63
	VEHJUP	C ₁₀₈ H ₃₆ O ₇₂ Zn ₂₂	[22, 1, 1]				
4	LEHXUT	C ₄₀₈ H ₂₁₆ N ₂₄ O ₁₂₀ Cu ₂₄	[1, 1, 1]	0.13 %	[37.163, 37.163, 37.163]	[60, 60, 60]	0.49
	XAMDUM02 (CuBTC)	C ₇₂ H ₂₄ O ₄₈ Cu ₁₂	[2, 2, 2]				
5	LURRIA (NOTT-1116)	C ₄₃₂ H ₁₉₂ O ₉₆ Cu ₂₄	[1, 1, 1]	0.11 %	[36.536, 36.536, 36.536]	[60, 60, 60]	0.61
	MIBQAR06 (MOF-5)	C ₄₈ H ₂₄ O ₂₆ Zn ₈	[2, 2, 2]				
6	HABRAF (PCN-68)	C ₄₃₂ H ₁₉₂ O ₉₆ Cu ₂₄	[1, 1, 1]	0.87 %	[37.291, 37.291, 37.291]	[60, 60, 60]	0.56
	HANHAH (ZnBTC)	C ₇₂ H ₂₄ O ₄₈ Zn ₁₂	[2, 2, 2]				

a Least common multiplier values for the extension of unit cell to generate supercell. 1 % tolerance was used to calculate these values.

b Cell distortion is calculated by summing how much interatomic distances are scaled in each *a*, *b*, *c* direction of the unit cell.

c The unit cell parameters for the calculated supercell given as [*a*, *b*, *c*] in Å and [*alpha*, *beta*, *gamma*] in degrees.

d Void fraction (*V_f*) are calculated using RASPA. For MOF pairs **2** and **3** smaller supercells are generated by increasing the tolerance. Supercells that combine single unit cell of each MOF was generated with 4.15 % and 4.08 % cell distortion for pairs 2 and 3 respectively.

Of the 18 hetero-interpenetrated structures we confirmed by visual inspection, six examples are shown in Figure 9, along with additional crystal structure information in Table 2.1. In determining the supercell parameters, a maximum tolerance of 1% in each *a*, *b*, and *c* direction of the cell was used. For that reason, the total cell distortion is always less than 3%. For four of the MOF pairs, the supercell size was relatively small. However, for two MOF pairs, the supercells were much larger. These huge supercells are not well suited for molecular simulations, but we discovered that by allowing a mere 4% distortion, these two supercells could be reduced to the size of a single unit cell of one of the MOFs from the pair.

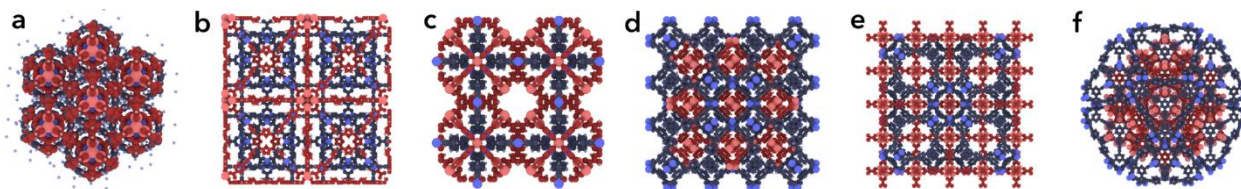


Figure 9 Some of the candidate hetero-interpenetrated structures discovered in this study: (a) 1 AXUBAW¹⁰⁷ [blue] + NODTIL¹⁰⁸ [red], (b) 2 IZEPAF¹⁰⁹ [blue] + WUHDAG¹¹⁰ [red], (c) 3 UQOFOX¹¹¹ [blue] + VEHJUP¹¹² [red], (d) 4 LEHXUT¹¹³ [blue] + XAMDUM02¹¹⁴ [red], (e) 5 LURRIA¹¹⁵ [blue] + MIBQAR06¹¹⁶ [red], (f) 6 HABRAF¹¹⁷ [blue] + HANHAH¹¹⁸ [red].

Since MOFs can undergo structural changes, due to their flexible nature¹¹⁹, it is not out of the question that the frameworks and unit cell sizes may adjust slightly to accommodate hetero-interpenetration. Given a successful synthesis, this suggests that interpenetration of similar frameworks with functionalized linkers can be possible. Combining multiple linkers into an interpenetrated structure can be a way of attaining multifunctional materials.

2.3 Conclusion

Here we presented a novel algorithm that can quickly test whether two given crystal structures have the potential to interpenetrate with one another and shared its source code. We used this algorithm to discover candidate homo- and hetero-interpenetrated MOFs, however our algorithm is designed to work with any pair of crystal structures, regardless of the shape or size of their unit cells. We believe interpenetrated MOFs may have promise in various applications that make use of their complex internal geometry. Moreover, in the case of hetero-interpenetration, the use of two distinct frameworks might yield materials with intriguing dual-functionality properties. For

example, there may be applications where different metal sites, from different individual frameworks, could catalyze different reaction steps. We hope this study will facilitate the discovery of hetero-interpenetrated MOF structures and motivate finding novel applications for their use.

3.0 Rational Design of Metal-Organic Frameworks for Improved Thermal Transport

In practice, the usefulness of metal-organic frameworks (MOFs) for many gas storage applications depends on their ability to rapidly dissipate the heat generated during the exothermic adsorption process. Since the adsorption capacities of MOFs are reduced at higher temperatures, the exothermic process of gas adsorption can limit the rate at which tank-filling, separations, or other processes can be performed.¹²⁰ Thus, studying design principles for thermal transport in MOFs is critical for allowing these materials to reach their full potential for gas storage and separations applications.¹²¹ In this section, we investigate the effects of interpenetration and framework flexibility on thermal transport.

3.1 Thermal Transport in Interpenetrated Metal-Organic Frameworks

MOFs can be precisely designed to have a wide variety of architectures which can allow tuning their thermal conductivity. MOFs with particularly high void fractions are often capable of having interpenetrated or interwoven structures as discussed in Section 1.^{82,106} Interpenetrating frameworks provide parallel pathways for thermal transport. The effect of thermal coupling between frameworks, however, has so far been uncertain. In the present work, we use molecular dynamics (MD) simulations to investigate thermal transport in a variety of doubly interpenetrated MOFs. To isolate the effects of interpenetration from other structural parameters, a simple cubic idealized framework was considered. Effects of pore structure on thermal conductivity have been reported elsewhere.¹²² We find interpenetration yields a system thermal conductivity approximately equal to the sum of the two independent frameworks, which can be used as a “rule of thumb” for design purposes. We show that both the strength and range of interactions between

constituent frameworks play a significant role in framework mobility as well as framework coupling which can result in deviation from this relationship. To account for deviations from this general rule, we present equations that can be used as guidelines for predicting thermal conductivity in doubly interpenetrated MOF structures.

3.1.1 Methodology

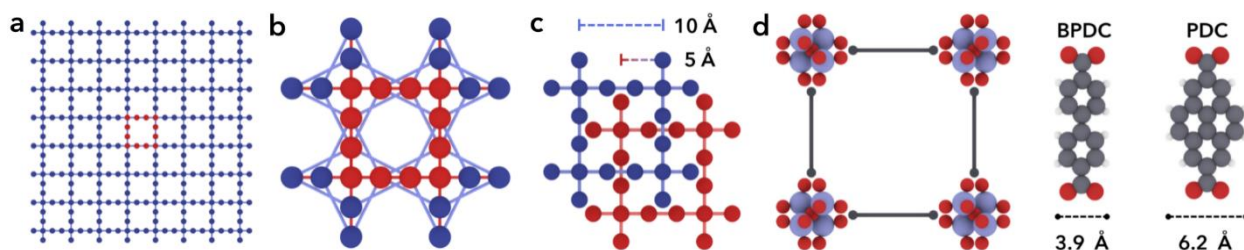


Figure 10 (a) Idealized porous crystal ($8 \times 8 \times 8$ cubic unit cells). (b) Bonding arrangement for a single unit cell using Morse potentials (red bonds are modeled more strongly than blue bonds). (c) Doubly interpenetrated unit cell with framework depicted as red and blue (initial frameworks in each simulation are 5 \AA apart in each dimension). (d) Different interpenetration configurations based on cubic IRMOF series¹²⁵: metal center distribution with BPDC linker (IRMOF-9) and PDC linker (IRMOF-13) representing less and more bulky linkers, respectively. Color scheme is as follows: Zn (blue spheres), O (red spheres), C (gray spheres).

We used an idealized cubic MOF structure inspired by MOF-5 to better understand parameters that affect thermal transport, as we had done in prior studies^{122,123} (see Figure 10a). The idealized interpenetrated MOF allows us to study the effect of framework interactions parametrically which would not be possible in a real interpenetrated MOF. We use two-body bonded interactions between atoms within each of interpenetrated structures, modeled using the Morse potential (see

Figure 10b).¹²⁴ The force field parameters were chosen so that the thermal conductivity of the simple cubic structure with a pore size of 1 nm was of the same order as a typical MOF (~1 W/mK).

The interpenetrated structure is generated by creating a copy of the idealized structure and translating it 5 Å in each dimension which corresponds to the maximal distance between frameworks (see Figure 10c). All thermal conductivity predictions were done using the Green-Kubo approach and equilibrium molecular dynamics (MD) simulations (LAMMPS¹²⁶). More simulation details including force field parameters are provided in Appendix B1.

The non-bonded interactions between interpenetrating frameworks were modeled by a Lennard-Jones potential where ε is the depth of the potential well and σ is the distance at which the interatomic potential is zero (see Eq. 2-1). A range of ε values between 0.01 – 1 kcal/mol and σ values between 1 – 6 Å were chosen to systematically understand the effects of framework interactions on thermal transport. Then, an ε value of 0.105 kcal/mol (corresponding to a carbon atom in UFF¹⁰¹) and σ values of 3.5 Å and 4.5 Å were selected to represent different interpenetration configurations for further analysis. The σ influences framework mobility where a value of 3.5 Å allows interpenetrating frameworks to “freely” translate relative to each by 2 Å in each direction, while a σ value of 4.5 Å models interpenetrated frameworks that are “locked in” and whose distance from each other remains constant. These configurations can be imagined as, for example, isorecticular MOFs with more or less bulky ligands (see IRMOF-13 vs. IRMOF-9 in Figure 10d) that correspond to frameworks that are “locked in” or “free”, respectively.

3.1.2 Results and Discussion

Framework interaction dependency of constituent position and thermal conductivity. The effect of inter-framework interactions on thermal conductivity and framework mobility was

investigated by calculating thermal conductivity and MSD for a wide range of ε and σ values (see Figure 11). On average, the thermal conductivity for the interpenetrated framework was found to be around 1.6 W/mK which is approximately double that of the single framework (0.82 W/mK). Consequently, this led us to explore the idea that the thermal conductivity of the interpenetrating frameworks can be predicted by a simple linear combination rule:

$$k_{IP} = k_1 + k_2 \quad \mathbf{3-1}$$

where k_{IP} , k_1 , and k_2 are the thermal conductivities of the interpenetrating framework, single framework 1 and single framework 2, respectively. In order to understand the conditions under which this relationship holds, percentage error for predicting thermal conductivity using Eq. 3-1 was calculated (Figure 11b). As seen in Figure 11a and 11b the thermal conductivity is relatively constant in the region $0.01 < \varepsilon < 0.2$ kcal/mol and $1 < \sigma < 4.5$ Å. However, increasing ε above 0.1 kcal/mol decreases thermal conductivity for σ values lower than 4.5 Å as apparent from the dark blue region in Figure 11a. This low thermal conductivity region described by $1.5 \leq \sigma \leq 4.5$ Å and $0.1 \leq \varepsilon \leq 1.0$ corresponds to increased coupling of the frameworks, which likely leads to higher phonon scattering rates introduced by the interactions between two frameworks. We then modified Eq. 3-1 by adding a coupling constant (γ) that depends on the interframework interactions as follows:

$$k_{IP} = (k_1 + k_2)(1 - \gamma) \quad \mathbf{3-2}$$

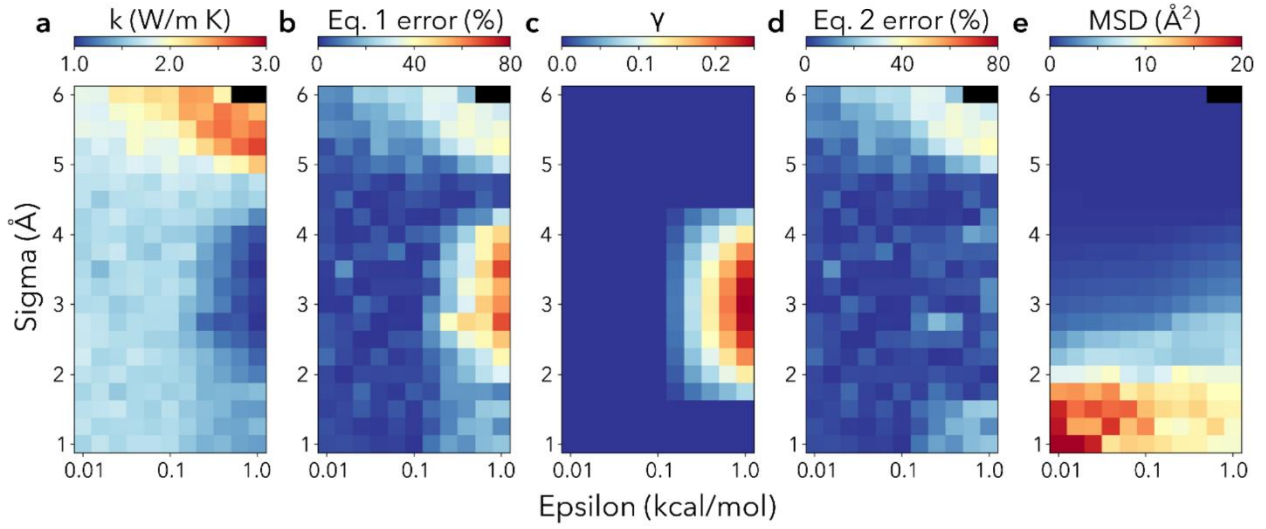


Figure 11 Effect of framework interaction on thermal conductivity and framework mobility in terms of forcefield parameters. For each plot, each bin represents a simulation with corresponding ϵ and σ values. The black bins on the upper right-hand side are for simulations where high repulsive forces caused frameworks to collapse. (a) Thermal conductivity (W/m K). (b) Thermal conductivity prediction error (%) for interpenetrated framework using the relationship in Eq. 3-1. (c) Coupling constant (γ). (d) Thermal conductivity prediction error (%) for interpenetrated framework using the relationship in Eq. 3-2. (e) Mean squared displacement, MSD (\AA^2). Derivation of Eq. 3-2 and the full equation of the coupling constant is provided in Appendix B1.

We defined individual coupling constants for σ and ϵ as $\gamma = \gamma_\epsilon \gamma_\sigma$ and derived equations to represent the coupling seen for the region $1.5 \leq \sigma \leq 4.5 \text{ \AA}$ and $0.1 \leq \epsilon \leq 1.0$. As seen in Figure 11c the coupling constant was modeled to increase linearly with ϵ and change quadratically with σ between 0 – 0.25. Including the coupling constant in Eq. 3-2 decreases the average error for the whole interaction range from 13.9 % to 7.8 % (Fig 11d). We limited the region of the coupling constant because we believe the deviations seen from Eq. 3-1 outside this region are not related to framework coupling. It can be seen in Figure 11a that increasing σ above 4.5 \AA increases the

system thermal conductivity especially at higher ϵ values. This increase is a result of stronger interactions between frameworks providing better thermal transport pathways. As for $\sigma < 1.5 \text{ \AA}$ we observe very high framework mobility (Figure 11e) which is attained to unphysically low repulsive forces causing frameworks to slide through each other.

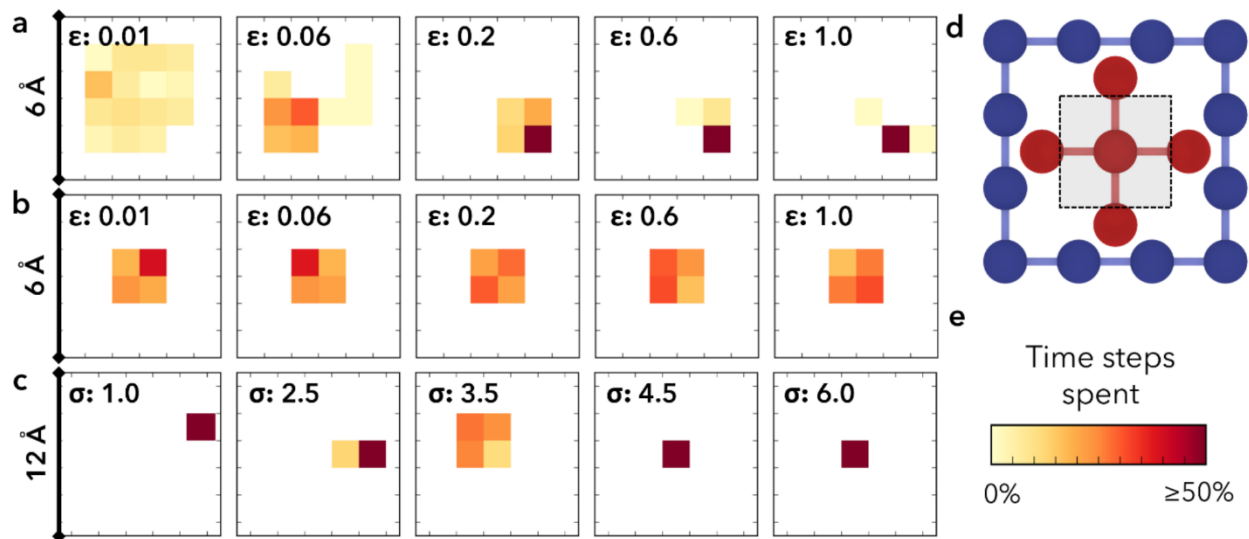


Figure 12 Effect of interpenetration interaction on framework distances during simulation. Framework interactions are modeled using Lennard-Jones potential. (a) $\sigma: 3.5 \text{ \AA}$ and (b) $\sigma: 4.5 \text{ \AA}$ with varying ϵ values in kcal/mol shown in figure. Grid size: 6 \AA and bin size: 1 \AA (c) $\epsilon: 0.105 \text{ kcal/mol}$ and varying σ values shown in figure. Grid size: 12 \AA and bin size: 2 \AA (d) Framework distances are measured according to middle red atom with reference to corner atoms of the surrounding blue framework. $5 \text{ \AA} \times 5 \text{ \AA} \times 5 \text{ \AA}$ cube shown as dashed box in 2 dimensions. The yellow-red bins represent the position of the other framework. (e) Time spent in given location are given in percentage. Color scale is limited to 50 % of simulation time for clarity. All results are for x and y directions from a single run. More information about the framework mobility calculations are provided in Appendix B1.

Framework mobility is also significantly affected by the force field parameters as evident from the MSD shown in Figure 11e. In addition to MSD, the framework mobility was investigated by

calculating the relative distance between reference atoms selected from interpenetrating frameworks (see Figure 12). The relative distance of one corner atom of the second framework (Figure 12d shown in red) to the 8 corner atoms of the surrounding first framework (Figure 12d shown in blue) were calculated from MD trajectories. The resulting 2D histograms given in Figure 12 show where the framework spends time during the simulation. The effect of ε is shown in Figure 12a for σ 3.5 Å and Figure 12b for σ 4.5 Å and the effect of σ is shown in Figure 12c.

Generally, σ is inversely related to the total area the frameworks can translate relative to each other whereas ε is directly related with the amount of time frameworks spend in a given configuration. Consequently, MSD is generally higher at lower ε and σ values. Above σ value of 4 Å, the frameworks are tightly locked therefore any change in force field parameters do not reflect directly on the MSD. Below 4 Å, however, MSD increases with decreasing σ as seen in Figure 11e. For lower σ values, there are multiple potential wells in between the frameworks. As a result, frameworks reside in different potential wells during each run and can jump between wells during simulation (see Figure 12a). With increasing ε , the energy barrier to jump between potential wells increases and frameworks become more closely coupled. Depending on the initial velocities, frameworks are trapped (for the duration of the simulation) in a position relative to each other (Figure 12c). For low ε values, however, frameworks easily move relative to each other (Figure 12a). Given an infinite simulation time, the average distance between frameworks should correspond to optimal distance since, by symmetry, each corner would be visited equally many times resulting in complete sampling of the configuration space.

For low σ values, the frameworks have increased mobility as the amount of space they can translate with respect to each other with the same energy penalty is increased. This is also complemented by the MSD (Figure 11e) where the displacement generally increases towards

lower σ values. For $\sigma \geq 2 \text{ \AA}$ increasing ε slightly decreases MSD since fewer potential wells are visited during a simulation. The high MSD for $\sigma < 2 \text{ \AA}$ is due to frameworks sliding through each other since interatomic distances within a framework are 3.3 \AA . In this region increasing ε decreases the MSD as the interaction strength is increased. However, these extraordinary framework interactions are not expected to be observed in real MOFs.

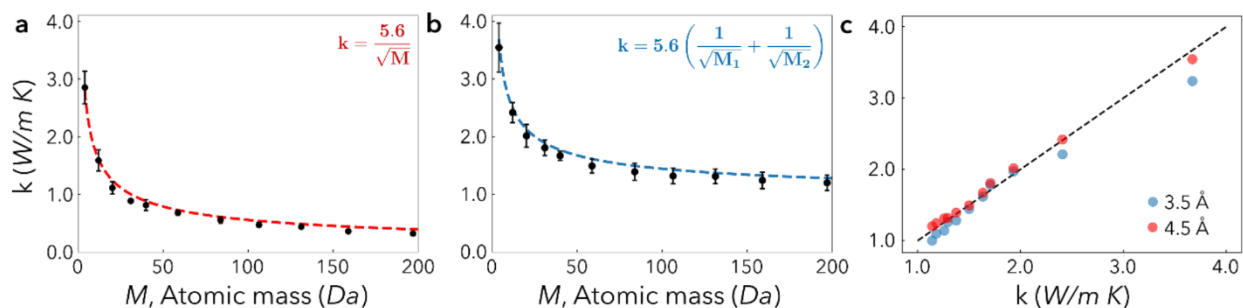


Figure 13 Effect of atomic mass on thermal conductivity (a) Single MOF (b) Free interpenetration (σ : 3.5 \AA) Dashed lines are equations shown in the figure. (c) Parity plot for predicted (Eq. 3-1) and simulated thermal conductivities for “free” and “locked” interpenetrated MOFs for different masses. For interpenetrated structures, atomic mass of the second framework (M_2) is modified whereas first framework atoms are always chosen as Ar (M_1 ~40 Da). Error bars represent one standard deviation of uncertainty.

Mass dependency of thermal conductivity. Initially thermal conductivities for a single framework were investigated for different atomic masses between 4 to 200 Da (i.e., changing the mass of every atom in the framework, see Figure 13). As seen in Figure 13a, thermal conductivity as a function of atomic mass shows a $1/\sqrt{M}$ relation. As previously shown by others,¹²⁷ this is because frequency and group velocity of acoustic phonons in the lattice scales as $1/\sqrt{M}$ whereas the mean free path and specific heat do not change considerably with mass. We then investigated interpenetrated frameworks, where the atomic mass of one of the frameworks was changed and

the other kept constant. We found the same relationship to hold for both “free” and “locked” interpenetration (Figure 13b).

Moreover, thermal conductivity values for the interpenetrated framework is approximately the sum of thermal conductivity of individual frameworks. For instance, thermal conductivity for individual frameworks made of atoms that have masses of either, 39.95 Da (Ar), or 83.80 Da (Kr), have thermal conductivities of 0.83 W/mK and 0.57 W/mK, respectively. Summing their individual thermal conductivities gives 1.40 W/m K, which is between 1.49 and 1.34 W/m K given by the interpenetrated frameworks having σ values of 4.5 Å and 3.5 Å respectively. As shown in Figure 13c, the predicted thermal conductivities (using Eq. 3-1) for different masses match closely with simulated thermal conductivity values. This suggests that a linear combination of single-framework thermal conductivities is a good model for the conductivities of interpenetrated frameworks, even when their corresponding masses are different.

3.1.3 Conclusion

The work presented here shows that, based on MD simulations, doubly interpenetrated MOFs will have thermal conductivity approximately the sum of the constituent frameworks. For rare cases where frameworks are not maximally interpenetrating and interframework attraction is high, the effect of coupling might result in lower thermal conductivity than the sum of individual frameworks. This suggests that the nature of interpenetration is quite important for thermal conductivity. We show that the decrease in thermal conductivity can be approximated by calculating a coupling factor using force field parameters (σ and ϵ) that define interframework interactions. For interactions described by $0.01 < \epsilon < 0.1$ kcal/mol and $1 < \sigma < 4.5$ Å the effect of coupling was found to be minimal.

We believe these results provide important insights into the gas adsorption application of interpenetrated MOFs especially for small gasses such as H₂. The inclusion of additional frameworks could increase storage capacity of the gas by increasing adsorption sites and provide additional thermal transport pathways which allows the generated heat to dissipate more quickly.

3.2 Thermal Transport in Flexible Metal-Organic Frameworks

There is considerable recent interest in the use of so-called “breathing” porous crystals for a wide range of gas adsorption and separations applications, such as for improved natural gas fuel tanks in cars.^{128–134} These crystals, as mostly exemplified by metal–organic frameworks (MOFs), have pores that are flexible and can undergo reversible phase transformations in response to external stimuli such as host–guest interactions, temperature, and pressure.^{135–137} Particularly, the pores can expand considerably when loaded with gas molecules. Unlike rigid porous crystals, flexible porous crystals show step-shaped gas uptake behavior that make them inherently more practical for pressure/temperature-swing adsorption/separations, working with smaller pressure/temperature differences and much higher working capacities.¹²⁹ Without considering transient thermal effects, the mechanisms of phase transitions in breathing crystals have been extensively investigated.^{138–141,128,142,143} However, an often overlooked challenge in using porous materials for gas storage is that the process of gas adsorption (or desorption) generates (or consumes) significant amounts of heat. For rapid loading, this leads to sharp temperature spikes,¹⁴⁴ which inhibits further adsorption of gas and largely mitigates the benefits of using a porous adsorbent in the first place. Similarly, for rapid unloading, the sharp temperature drop exacerbates the stranded gas problem as the gas molecules are more likely to condense onto the pore walls. Efficient thermal transport can reduce this effect by facilitating heat dissipation. In this regard, previous studies have investigated thermal transport in rigid MOFs using atomistic modeling^{145–151} and experiments.^{152–155} Whereas the thermal effects of adsorption in rigid porous crystals are now somewhat understood, the more complicated thermal behavior of flexible porous crystals, which show even greater promise for many applications, has not been studied at all.

In this work, we study thermal conductivity of idealized breathing porous crystals. We perform molecular dynamics (MD) simulations on a series of idealized model structures representing porous crystals at different stages of pore expansion and apply the Green-Kubo method to predict their thermal conductivities with and without adsorbed gas. We find that upon pore expansion, with increasing pore volume, while thermal conductivity parallel to the direction of change increases, while thermal conductivity in the other directions remains unchanged. We observe that, similar to our previous studies,^{148,149} the presence of adsorbed gases reduce thermal conductivity. However, the reduction is less pronounced when the pores are in the fully contracted state.

3.2.1 Methodology

We use idealized structures with pores tilted at various angles, as shown in Figure 14. We start with a 40-degree tilt angle to represent the closed form going up to a cubic pore with 90-degree tilt angle to represent the open form with 10-degree increments. This breathing model was adapted from our idealized cubic structure described in prior work. The simple cubic lattice structure is built using 7 atoms per unit cell. As depicted in Figure 14a, we define two-body bonded and three-body angular interactions between atoms, which are modeled using harmonic potentials. To determine meaningful spring constants for the potentials we screened spring constants between 1 - 10 kcal/mol for the 90° structure. We picked the parameters that resulted in a thermal conductivity of ~1 W/m K and a simulation box volume that is within 5% of the ideal volume (see Appendix B2 for the force field parameters used). For all angle bending potentials, we used an equilibrium angle of 180° except for the angles containing corner atoms, for which we use different equilibrium angles (90°, 80°, 70°, 60°, 50° and 40°).

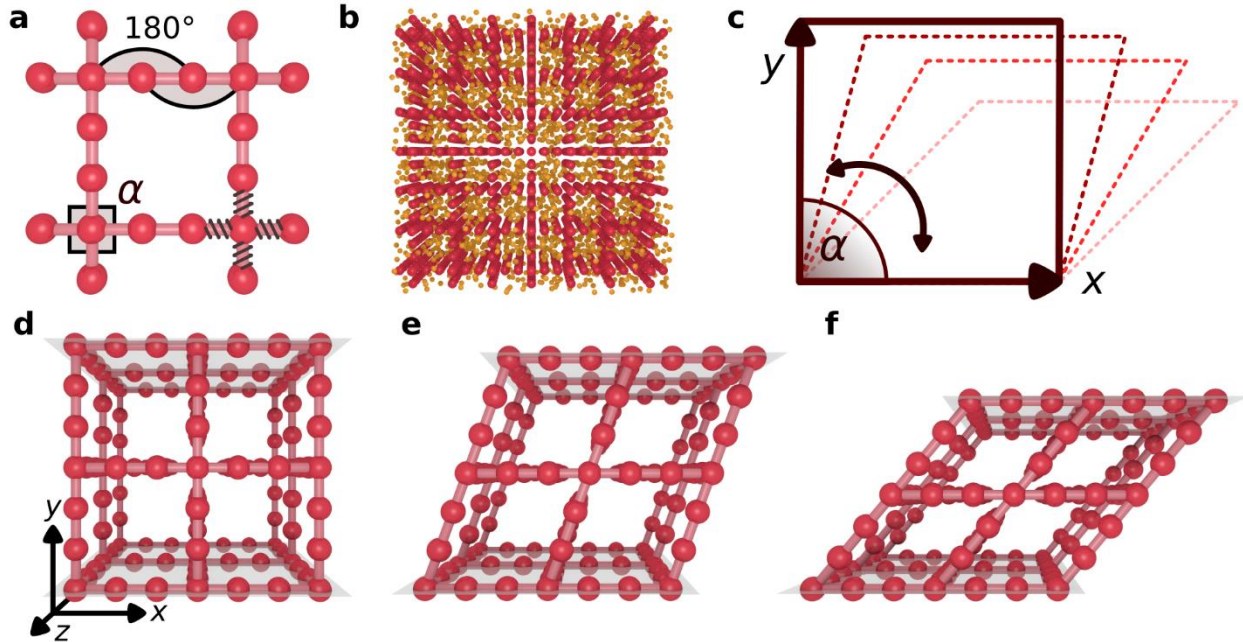


Figure 14 Cross-sectional view of the idealized simple cubic structure and the harmonic bonds and angles used in the potential. (b) Complete simulation box of the idealized simple cubic structure with pores filled with adsorbates at 5 molecules / nm³ density. (c) The idealized structures tilted at different angles to generate different stages of transition from contracted to expanded pores. 2 x 2 x 2 unit cell of the idealized structure at (d) 90°, (e) 70°, and (f) 50° tilt angles.

To investigate the effect of adsorbed gas on thermal transport, for all structures, a gas density of 5 molecules / nm³ was used. As the volume of the simulation box is changed with angle, the initial number of molecules were adjusted accordingly. For each angle different gas molecule configurations were generated, however for the same angle same initial configuration was used for different simulations using a different initial velocity distribution. The gas is methane, which is modeled as a point particle with force field parameters given in Appendix B2.

All thermal conductivity predictions were done using the Green-Kubo approach¹⁵⁶ and equilibrium molecular dynamics (MD) simulations. All simulations were carried out at a temperature of 300 K and atmospheric pressure using a time step of 1 fs. The partial enthalpy terms

required to analyze multicomponent systems were implemented as discussed in Refs.¹⁵⁷ The MD simulations were performed using a version of Large-scale Atomic/Molecular Massively Parallel Simulator (LAMMPS)¹⁵⁸ software which has the correct implementation of heat flux for many-body potentials.¹⁵⁹ Periodic boundary conditions were applied in all directions. To gain further insight into the thermal conductivity predictions, we also calculated the corrected diffusivity of gas molecules within the porous crystals, which is associated with the gas mobility.¹⁶⁰ The corrected diffusivity is based on a Green-Kubo relation and is defined as the time integral of the center of mass velocity autocorrelation function for the gas component. Details of the Green-Kubo calculations for both thermal conductivity and diffusivity along with samples of the associated autocorrelation functions and their integrals are provided in Appendix B2.

3.2.2 Results and Discussion

The thermal conductivities of the structures at different stages of expansion were first predicted without any adsorbed gas. As shown in Figure 15a, thermal conductivity in the y direction, which is the only direction where the box length changes (see Figure 14c), increases as the pore is expanded (tilt angle increases to 90°). However, thermal conductivities in the x and z directions remain unchanged. This trend is likely due to the fact that bonds become less effective in transferring heat in the y -direction when tilted. In the absence of gas, these bonds are the means of transporting heat through the atomic vibrations (i.e., phonons) in a dielectric solid. Supporting this argument, as shown in Figure 15b, thermal conductivity scaled by $\sin(\alpha)^{-3}$ becomes nearly constant (α is the tilt angle).

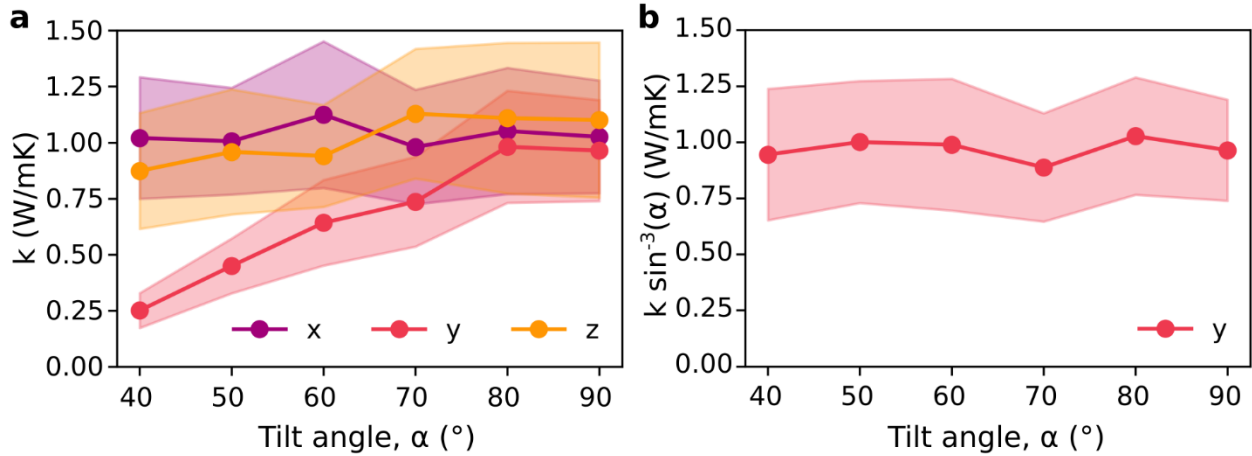


Figure 15 (a) Thermal conductivity vs tilt angle. (b) Thermal conductivity in the y-direction scaled with $\sin(\alpha)^3$ vs tilt angle.

To further shed light on the effect of pore contraction on thermal transport, thermal conductivity was decomposed into the contributions from different interatomic potentials (bond and angle). The decomposition was made possible by the Green-Kubo method, where forces and energies from any potential can be separately treated in the equation. Figure 16 shows the contributions from bond and angle potentials on the overall thermal conductivity. It is observed that overall, the angle contribution is much smaller than the bond contribution. Interestingly, the decrease of overall thermal conductivity for smaller angles is due to the decrease of the bond contribution. This further confirms the reason mentioned earlier, that is: the thermal conductivity in any direction depends on how bonds are aligned in that direction. For the structure with 90° , the thermal conductivity is the highest because the bonded atoms are parallel to the y-axis; while for smaller angles bonds are tilted from y-axis.

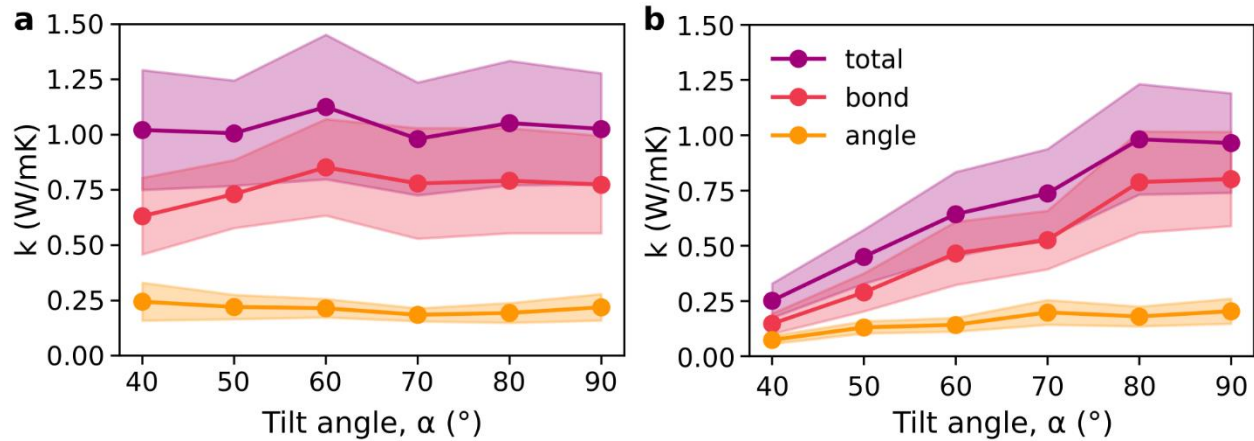


Figure 16 Thermal conductivity contribution from bond and angle potentials in a) x and b) y directions. z direction not depicted as the results were almost identical to the x direction.

We then predicted the thermal conductivity of the porous materials loaded with gas at a density of 5 molecules/nm³. The results are plotted in Figure 17. Like the case without gas, thermal conductivity in the y-direction decreases as the pores contract. However, the decrease in thermal conductivity is not as significant. With gas present in the pores, the thermal conductivity for the structure with 40° tilt angle is approximately half of its value at 90° tilt angle. However, for the structures without gas, the thermal conductivity of the structure with 40° tilt angle is almost 20% of its value for the structure with 90° tilt angle.

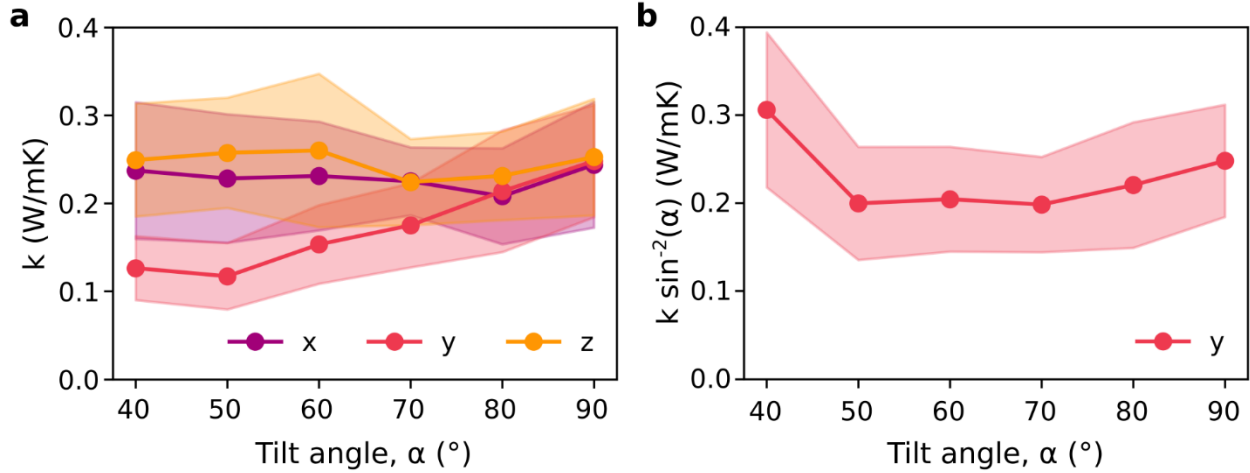


Figure 17 (a) Thermal conductivity of gas loaded structures vs the angle which resembles the stage of expansion. (b) y-direction thermal conductivity of the gas loaded structure scaled by $\sin(\alpha)^2$ vs angle.

Next, we address the relative effect of adsorbed gas on thermal conductivity of porous crystals at various stages of contraction. As shown in Figure 18a, the overall thermal conductivity is significantly decreased upon loading structures with gas; a phenomenon previously observed in our studies.^{148,149,161} Except for the fully contracted pores (i.e., 40° tilt angle), thermal conductivity of gas loaded structures is 25% of that of the structures without gas. At fully contracted state (40°), the thermal conductivity of the gas loaded structure is 50% of that without gas. The observed weaker effects from gas-crystal collisions on the thermal transport in contracted system compared to other systems is likely due to the already shorter intrinsic lifetimes of phonons.

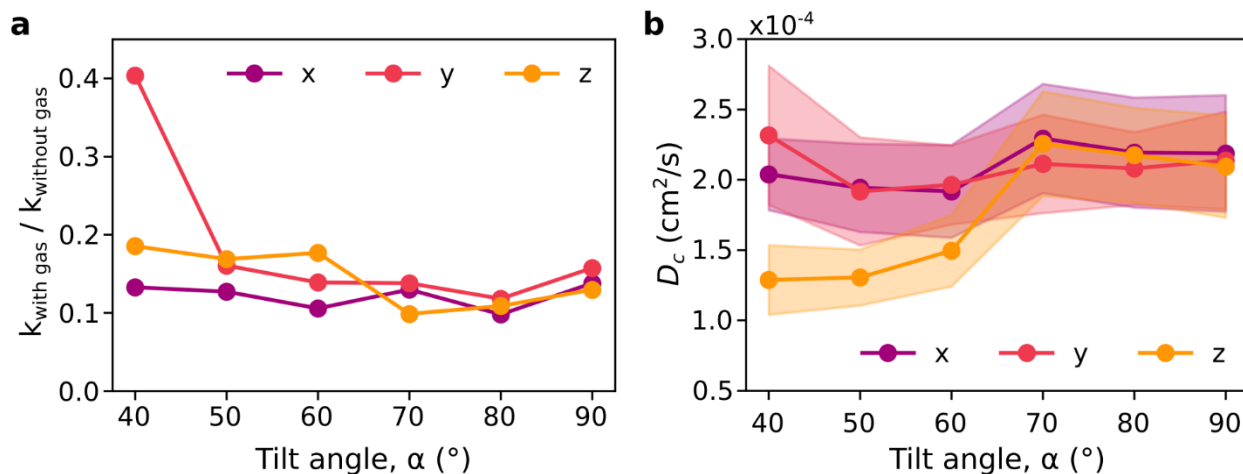


Figure 18 (a) Ratio of thermal conductivity for gas loaded and empty crystals at different stages of pore expansion. (b) Corrected gas diffusivity for gas loaded crystals at different stages of pore expansion.

The other important parameter that could affect the rate of gas adsorption in the pores during expansion is the gas diffusion through pores. To better understand the gas molecule dynamics inside the pores, we calculated corrected gas diffusivities, which are plotted in Figure 9b. The diffusivities in x and y directions are nearly constant. However, in the z direction, the only direction where the pore cross sectional area changes with changing angle, the diffusivity increases with pore expansion. This is due to the pore expansion which allows higher gas mobility in z direction. It shows that during gas adsorption, upon pore expansion, the diffusion of gas molecules into pores would be facilitated.

3.2.3 Conclusion

With the purpose of understanding heat transfer in breathing porous crystals, we studied a series of idealized model systems using molecular dynamics simulations. We investigated the effect of pore expansion on thermal conductivity with and without adsorbed gases. We showed

that, in the direction that pore changes, the thermal conductivity of empty porous crystals increases with expansion. In contrast, the thermal conductivity in other directions do not change with pore expansion. Our study also reveals that the presence of gases decreases thermal conductivity in all states of pores, with the lowest effect on the fully contracted pores. Lastly, we show that the gas diffusion increases during pore expansion, leading to easier transport of gas.

4.0 Computational Methods for Rational Design of Nanocars and Modeling Their Diffusion on Metal Surfaces

4.1 Modeling Surface Diffusion of Large Organic Molecules

Understanding and controlling molecular motion on surfaces is essential for the bottom-up construction of nanoscale machines.^{162–165} Such machines are commonly utilized in cells to transport molecular cargo: enzyme molecules are moved along protein filament tracks converting chemical energy into mechanical work.⁷ A class of artificial molecular machines, nanocars, have been studied to understand and control molecular motion on metal surfaces. From the initial design with fullerene wheels in 2005¹⁶⁶ to more advanced designs with rotatable molecular wheels,⁸ various strategies have been employed to achieve better control over the diffusion process.^{9,10,167} More recently in 2017, the world's first ever nanocar race was organized where six teams raced their molecular machines on a 100 nm track.¹⁶⁸ As highlighted by the contestants, molecular design played a crucial role in controlling the motion of the nanocar.^{169–171} Although, substantial effort has been put into understand key features that affect nanocar diffusion, only a limited number of molecular designs have been tried so far and a thorough understanding of the relevant design parameters is still lacking. As discussed by the competitors as well as the organizers of the nanocar race, a better understanding of the key features that affect nanocar motion is required and computational methods can be helpful for this purpose.^{169,170} A key question, also asked when designing “macrocars,” is how to add weight while maintaining or increasing speed (i.e., the diffusion coefficient)?

In the broadest definition, nanocars are simply large molecules designed to have fast surface diffusion (with or without external stimuli). Previously, several experimental studies were employed to study the diffusion of large molecules on metal surfaces. Several strategies have been shown to greatly influence diffusion such as molecular functionalization^{164,172} and manually adjusting the orientation of the molecule with respect to the substrate lattice by a scanning tunneling microscope (STM) tip.¹⁶³ Schunack et al. studied the diffusion of decacylene (DC) and hexa-*tert*-butyldecacylene (HtBDC) using time-resolved STM images and found out that long jumps spanning multiple lattice spacings were the dominant type of diffusion as opposed to conventional surface diffusion described by random jumps between nearest neighbor sites. Moreover, they demonstrated that the molecular diffusion rate can be tailored by raising the molecule from the surface by *tert*-butyl spacer groups resulting in a diffusion constant higher by 4 orders of magnitude. Similarly Sun et al. studied the influence of *tert*-butyl spacer groups on the mobility of organic molecules on a Cu(110) surface.¹⁷² Conversely, they found that adding *tert*-butyl groups lowered the mobility of the molecule even compared to a higher molecular weight molecule. In their case *tert*-butyl group changed the adsorption geometry and locked the molecule to the surface highlighting the importance of the relation between the molecular 3D shape and surface geometry. Otero et al. investigated the diffusion of Violet Lander (VL, C₁₀₈H₁₀₄) on Cu(110) and showed that they can change the diffusion coefficient by two orders of magnitude by switching between different surface orientations.¹⁶³ They achieved this by manipulating the molecular orientation with respect to the substrate lattice using STM. In the immobile configuration the VL molecule locks to the surface and it is kinetically stabilized at low temperature, which emphasizes the importance of considering the complementarity between the molecular and surface geometry.

Although these strategies discovered by trial-and-error, such as inserting *tert*-butyl spacers, are useful, a more systematic investigation of surface diffusion as a function of structure is needed to improve future nanocar designs. Akimov and co-workers have performed several studies to understand the motion of nanocars on metal surfaces using rigid body molecular dynamics.^{12,61–63} They employed a simplified nanocar design and divided the molecule into rigid fragments as four wheels and a chassis. They showed that, in agreement with experimental results, nanocar mobility was initiated at temperatures higher than 400 K and they observed rotational motion of the wheels at 500 K. In a later study they investigated the effect of an electric field (e.g. created by the STM tip) on the diffusion of the same structure.⁶³ In order to mimic the electric field, they employed a custom charge transfer method (developed in a previous study⁶²) and performed a series of rigid-body molecular dynamics simulations. They found that external electric fields can be used to drive nonpolar nanocars unidirectionally and that the rolling mechanism of the wheels is the dominant factor in the nanocar surface diffusion as opposed to a simple hopping and sliding mechanism. Ganji et al. studied the motion of a carborane-wheeled nanocar on graphene/graphyne surfaces using density functional theory.⁶⁴ They calculated the activation energy for the motion of the four wheeled nanocar as 17.06 and 4.38 kcal/mol for graphene and graphyne surfaces, respectively. Even though these studies provide important insights on the motion of nanocars and their interactions with the surface, they focus on qualitatively explaining the motion rather than quantifying it by estimating a diffusion coefficient. Therefore, these methods cannot be used directly to estimate the timescale of diffusion and rank molecules. Moreover, these studies focused on elucidating the motion of nanocars instead of understanding how structure affects diffusion, which could be helpful to design better nanocars.

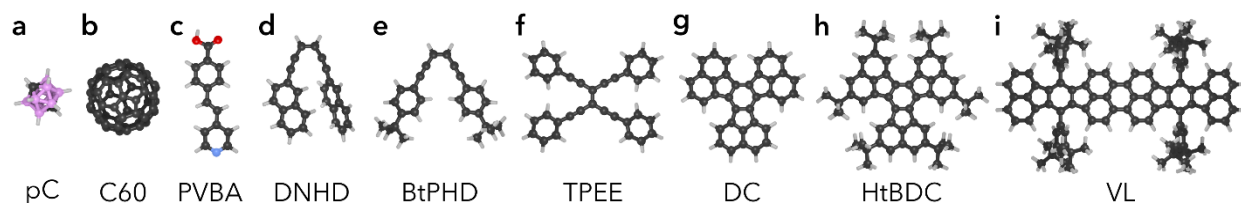


Figure 19 Molecular structures used in this study with chemical names where abbreviations and chemical formulae are given in brackets: (a) p-carborane¹⁷³ [pC, C₂H₁₂B₁₀]; (b) fullerene¹⁷⁴ [C60, C₆₀] (c) 4-trans-2-(pyrid-4-yl-vinyl) benzoic acid¹⁷⁵ [PVBA, C₁₄H₁₁O₂N]; (d) (Z)-1,6-di(naphthalen-2-yl)hexa-3-en-1,5-diyne¹⁷² [DNHD, C₂₆H₁₆]; (e) (Z)-1,6-bis-(4-(tert-butyl)phenyl)hexa-3-en-1,5-diyne¹⁷² [BtPHD, C₂₆H₂₈]; (f) tetrakis(phenylethynyl)ethane¹⁷² [TPEE, C₃₄H₂₀]; (g) decacylene¹⁶⁴ [DC, C₃₆H₁₈]; (h) hexa tert-butyl decacylene¹⁶⁴ [HtBDC, C₆₀H₆₆]; and (i) violet lander¹⁶³ [VL, C₁₀₈H₁₀₄]. Color scheme is as follows: C (black), N (blue), O (red), B (pink), H (light gray).

In this work, we investigated the diffusion of 9 large organic molecules on a Cu (110) surface (see Figure 19). We chose these molecules to represent a wide variety of molecular geometries and to be able to compare our findings with available experimental studies of their motion (references for the studies are provided in the Figure 19 caption). We used classical molecular dynamics (MD) simulations and estimated self-diffusion coefficients by calculating mean squared displacement. We found that even though the correct timescales of diffusion cannot be achieved with typical MD simulations (i.e., without rare-event sampling techniques), we can still obtain certain useful information, such as the preferential crystallographic directions for diffusion on the surface. To obtain diffusion coefficients within the same orders of magnitude as experimental measurements, we then employed umbrella sampling and the weighted histogram analysis method (WHAM)¹⁷⁶ to estimate free energy barriers for diffusion. Using the free energy profiles, we estimated hopping rates and self-diffusion coefficients using a transition state theory (TST) approach. We found that by tuning the surface-molecule interaction energetics and employing the TST method we can obtain activation energies and self-diffusion coefficients that are in good

agreement with experimentally observed values. Both methods predict the fastest and slowest molecules to be the same, however, the individual rankings varied slightly between different methods. Overall, we find that to optimize speed for a given molecular weight minimizing the molecule-surface interaction by elevating the body of the molecule with spacer functional groups is a good strategy, which is supported by empirical observations from past nanocar racers. To quantify this we proposed a metric, named *elevation-weighted-density*, to quickly rank molecular designs. Furthermore, we reiterate that the complementarity between the molecular design and surface geometry is crucial.

4.1.1 Methodology

Structure generation. We selected a total of 9 molecules, namely: p-carborane;¹⁷³ C60;¹⁷⁴ PVBA;¹⁷⁵ DNHD;¹⁷² BtPHD;¹⁷² TPEE;¹⁷² decacylene;¹⁶⁴ hexa tert-butyl decacylene;¹⁶⁴ and violet lander¹⁶³ (see Figure 19) to represent a wide variety of molecular geometries and to compare our findings with available experimental studies of their motion. Molecular geometries were optimized using Kohn-Sham density functional theory at BP86-D3/ Def2-SVP¹⁷⁷⁻¹⁷⁹ level of theory as implemented in ORCA.¹⁸⁰ The Cu (110) surface was generated using ASE¹⁸¹ slab builder tool to a size of 39.1 x 41.5 x 5.5 Å and 1400 atoms (see Figure 20a).

Molecular Dynamics. Molecular dynamics (MD) simulations in the NVT ensemble at 300 K were performed with a timestep of 1 fs for a total of 10 ns using LAMMPS.¹²⁶ 20 set of simulations were performed with different initial velocity distributions to improve statistical sampling. For each molecule, the center of mass was calculated at every 1 ps which was used to calculate the mean squared displacement (MSD) to estimate the self-diffusion coefficient. A periodic simulation box of 39.1 x 41.5 X 40 Å was used for all simulations. The Cu (110) surface was placed at the

bottom of the simulation box and the molecule was placed in the middle and 5 Å above the surface (see Figure 20). The surface atom positions were fixed during the simulations and nonbonded interactions between Cu atoms were neglected. All molecules were modelled as rigid bodies and a Lennard-Jones potential was used to model vdW interactions with a cut-off radius of 12.5 Å. The force field parameters were adopted from universal force field (UFF)¹⁰¹ and the Cu atom epsilon value was changed to 0.125 kcal/mol (instead of the original 0.05 kcal/mol) to increase surface adsorption energy (see Appendix C1 for all parameters used). Rigid body approximation was used to simplify the model and make it easier to tune the vdW interaction energy between the molecule and the surface. Furthermore, the main intention of modeling in this study is to provide a method to quickly screen candidate molecular geometries, therefore computational cost of the method was reduced with this approach. As a result, configurational changes within the molecule due to surface adhesion were neglected. The effects of this assumption are further discussed in the results and discussion section. More information about calculation of the self-diffusion coefficients are given in Appendix C2.

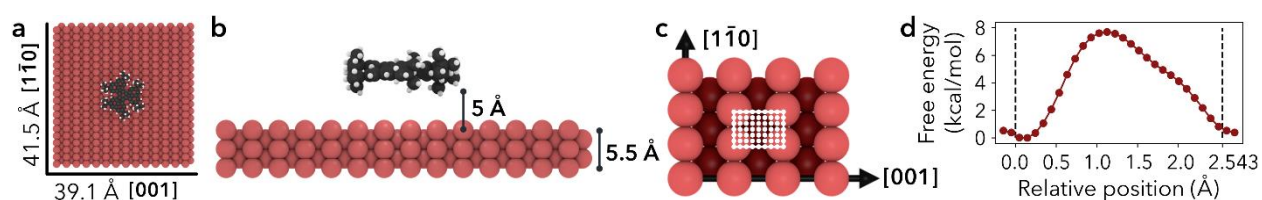


Figure 20 Simulation setup for HtBDC. (a) Top view - molecules are placed in the center of a 39.1 x 41.5 Å Cu (110) surface. (b) Side view - each molecule is placed 5 Å above the surface. (c) For TST calculations the unit cell of a Cu (110) surface is divided into 1131 grid points (29 points in $[1\bar{1}0]$ and 39 points in $[001]$ directions) with a step size of 0.1 Å. 3.597 x 2.543 (d) Representative free energy barrier for the diffusion of HtBDC molecule in $[1\bar{1}0]$ direction obtained from WHAM analysis (more simulation details in Appendix C).

Transition State Theory. As the diffusion of large molecules are quite slow and time scales cannot be achieved with traditional MD simulations, we employed umbrella sampling and weighted histogram analysis method (WHAM)¹⁷⁶ to calculate free energy barriers for diffusion. We divided the orthogonal unit cell of a Cu (110) surface using 0.1 Å grid spacing for both $[1\bar{1}0]$ and $[001]$ directions (see Figure 20c). For each point on the surface (1131 total), we placed the molecule at that point and constrained its motion in $[1\bar{1}0]$ and $[001]$ directions in separate simulations using a spring with a constant of 200 kcal/mol. The motion in the direction perpendicular to the surface was not constrained. We then let the molecule sample different configurations using the same simulation setup described above for the MD simulations with rigid molecules and a fixed surface. However, this time we scaled the mixed LJ epsilon parameter between the surface and molecule atoms by 10 to further increase the adsorption energy in order to better approximate the experimentally observed activation energy of diffusion. Using WHAM analysis and Boltzmann averaging we finally obtained a free energy barrier for diffusion in both $[1\bar{1}0]$ and $[001]$ directions. A representative energy barrier is provided in Figure 20d. After obtaining periodic free energy barriers we used dynamically corrected transition state theory method by Dubbeldam et al.¹⁸² to calculate the hopping rate ($k_{A\rightarrow B}$) and estimate self-diffusion coefficient (D_S). More details are given in Appendix C3.

4.1.2 Results and Discussion

We first investigated the diffusion of the molecules using classical MD simulations for the two primary directions of the Cu (110) surface namely, $[001]$ and $[1\bar{1}0]$ (see Figure 20c). Per the surface geometry, it is energetically more favorable to diffuse along the $[1\bar{1}0]$ direction compared to $[001]$ as highlighted by experimental studies.^{163,164,172,174,175}

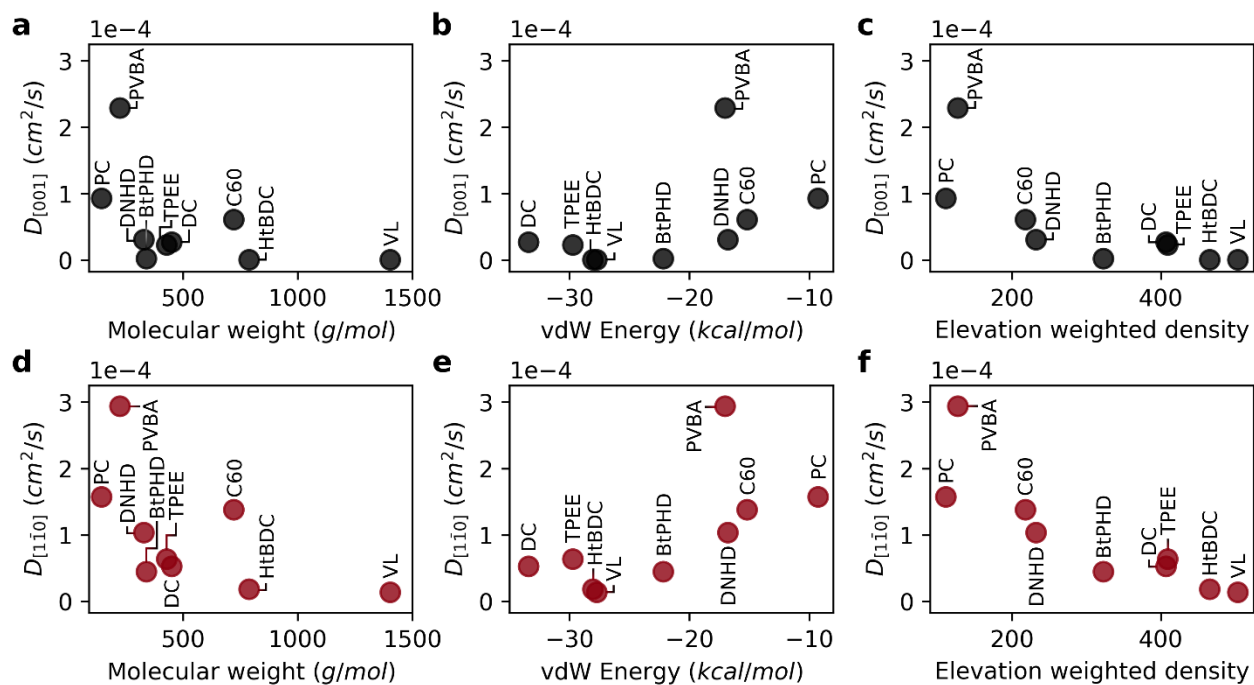


Figure 21 Diffusion coefficient calculated using MD simulations in $[001]$ and $[1\bar{1}0]$ directions: (a) molecular weight vs $D_{[001]}$ (b) vdW energy vs $D_{[001]}$ (c) elevation weighted density vs $D_{[001]}$ (d) molecular weight vs $D_{[1\bar{1}0]}$ (e) vdW energy vs $D_{[1\bar{1}0]}$ (f) elevation weighted density vs $D_{[1\bar{1}0]}$.

In Figure 21, self-diffusion coefficients calculated from MD simulations are given for both directions. Overall, the diffusion coefficient gets smaller with larger molecular weight and higher surface adhesion as the attraction between the surface and the molecule increases for both primary directions investigated (Figure 21a – d). However, it is also evident that not all molecules follow this relation directly, such as the PVBA molecule suggesting that the molecular geometry plays an important role in the diffusion. Furthermore, for all molecules the diffusion coefficient in $[1\bar{1}0]$ direction was higher than $[001]$ direction in good agreement with experimental observations.^{163,164,172,174,175} For the BtPHD molecule the addition of *tert*-butyl groups resulted in a slower diffusion compared to TPEE, and DNHD molecules and TPEE molecule was found to be slower than DNHD in agreement with Sun et al.¹⁷² However, addition of *tert*-butyl groups in

HtBDC molecule didn't results in a faster diffusion compared to the DC molecule as reported by Schunack et al.¹⁶⁴ Even though, in agreement with the experiments, we observed strong anisotropic diffusion for both of these molecules, our calculations did not rank these molecules the same way: DC molecule was found to be faster in our calculations than HtBDC molecule as opposed to Schunack et al. This difference in ranking might be caused by the assumed rigid geometry in our simulations, because whereas the *tert-butyl* spacers in HtBDC are likely to undergo configurational change as they interact with the surface which might increase or decrease the diffusion according to the complementarity of the final geometry with the surface. In the case of BtPHD vs TPEE adding *tert-butyl* groups decreased the diffusion whereas in DC vs HtBDC *tert-butyl* addition resulted in a faster diffusion according to experimental observations. This suggests that to get a better representation of the adsorption geometry configurational changes might need to be accounted, however they were neglected by the rigid approximation. Furthermore, the calculated diffusion coefficients for DC and HtBDC are in the range of 10^{-5} cm²/s which is approximately eight orders of magnitude higher than the experimentally observed values. This implies that the vdW interaction energy between the molecules and the surface is likely to be severely underestimated in our model. Even though we increased the UFF epsilon parameters five-fold to amplify surface adsorption energy, a further increase is required to approximate experimental energetics. However, estimating diffusion via classical MD simulations with such high interaction energies, without using a rare-event sampling technique, would be computationally infeasible. As the experimentally observed hopping events are very rare, it would require excessive computational time to have statistically significant hopping events during the simulations. However, even though the absolute timescale of the diffusion coefficients does not represent the experimental conditions, the relative

ranking of diffusion across the 9 molecules, as well as their diffusion along different crystallographic directions can be usefully investigated.

As molecular weight and vdW energy do not give a complete picture of diffusion we also propose a structural parameter, named elevation weighted density, based on molecular adsorption geometry. The calculation of this parameter is discussed in Appendix C4. As seen in Figure 21e and 21f the self-diffusion coefficients get smaller as the elevation weighted density increases. Moreover, compared to molecular weight there seems to be less outliers to this almost linear decrease. One reason might be that this parameter includes effect of both molecular weight and surface geometry.

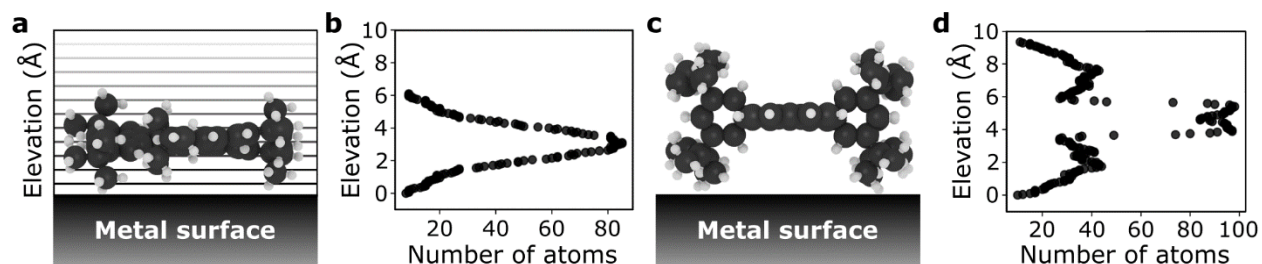


Figure 22 (a) Elevation weighted density calculation schematic for HtBDC. Starting from the bottom most part of the molecule, number of atoms are counted with 0.05 \AA discrete steps and using a cut-off radius of 1 \AA . (b) Plot of number of atoms with increasing elevation from the surface, i.e. elevation weighted density curve. (c) Side view of VL molecule on metal surface. (d) Elevation weighted density curve for VL molecule.

With the purpose of capturing the realistic time scale of diffusion, we calculated free energy barriers for the diffusion along the $[001]$ and $[1\bar{1}0]$ directions and estimated self-diffusion coefficients (see Figure 23). The activation energies for the average free energy profiles are given in Figure 23b and 23e for $[001]$ and $[1\bar{1}0]$ directions, respectively. As seen in the figure, the free energy barrier for diffusion is almost four times higher for the $[001]$ direction compared to the

[1 $\bar{1}$ 0] direction supporting experimental observed anisotropic diffusion.^{163,164,172,174,175} Consequently, this higher energy barrier results in a smaller diffusion coefficient for the [001] direction as seen in Figure 23a and 23d. By definition of TST, the self-diffusion coefficient is exponentially related to the energy barrier, therefore the diffusion coefficients calculated here span across a much higher range (8 orders of magnitude for [1 $\bar{1}$ 0] and 40 orders of magnitude for [001] directions). As a result, the anisotropy of diffusion is much higher compared to results obtained from MD simulations. Overall, similar to MD simulations the diffusion coefficients get smaller and the activation energies get higher with increasing molecular weight. We find that even though the individual rankings of diffusion coefficients were not identical between the two methods, both methods predicted the fastest and slowest molecules to be PVBA, and VL, respectively. Furthermore, ranking between DNHD, TPEE, and BtPHD molecules were found to be the same as in MD simulations in agreement with the experimental findings meaning addition of *tert-butyl* groups slowed surface diffusion. This also applied to DC and HtBDC molecules where addition of *tert-butyl* groups again resulted in slower diffusion for the HtBDC molecule in line with the MD simulations but opposing experimental observations. As rigid body approximation was also employed in TST simulations it is somewhat expected to see the same ranking with this method. We believe more sophisticated methods that account for the intramolecular reconfiguration during surface adhesion should be employed for more sensitive ranking. Alternatively, multi rigid body simulations or coarse graining methods could also be useful for this purpose.

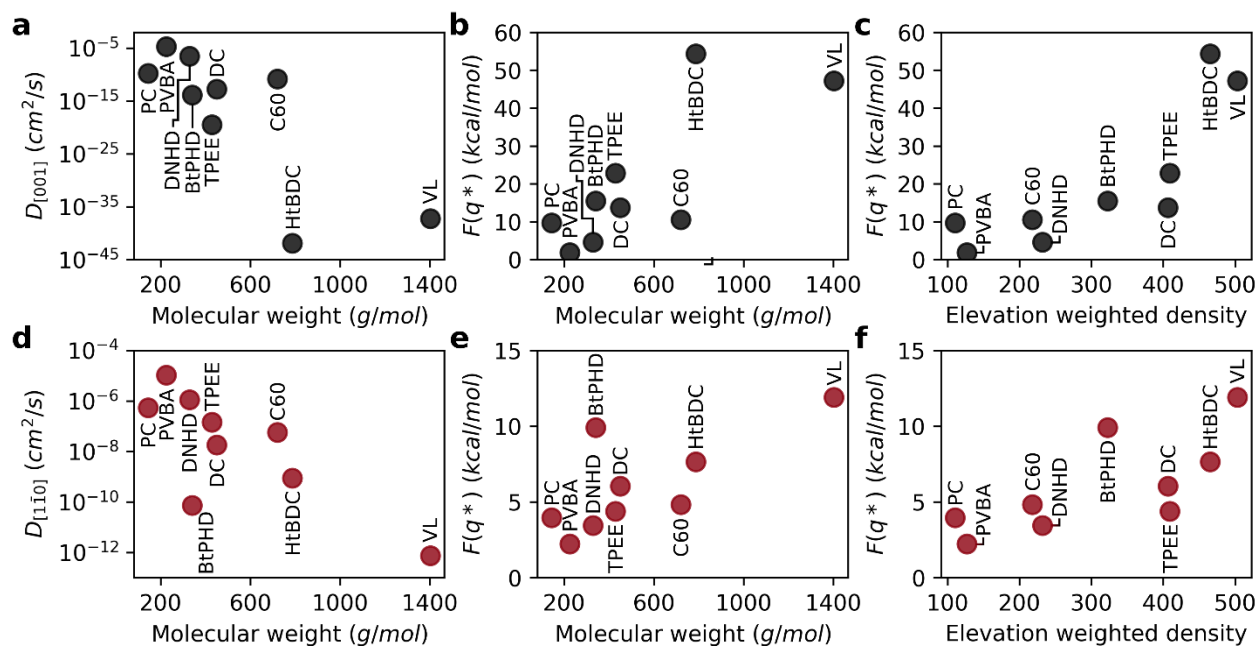


Figure 23 Transition state theory results: (a) molecular weight vs $D_{[001]}$ (b) molecular weight vs free energy barrier in [001] direction (c) elevation weighted density vs. free energy barrier in [001] direction (d) molecular weight vs $D_{[110]}$ (e) molecular weight vs. free energy barrier in $[1\bar{1}0]$ direction (e) elevation weighted density vs. free energy barrier in $[1\bar{1}0]$ direction.

As the team with the fastest molecule in the nanocar race, Simpson et al. highlighted several key features to improve velocity, maneuverability and function of nanocars: 1) using low molecular weight nanocars to decrease surface adhesion and make it easier to deposit under vacuum, 2) using large enough wheels to lift the chassis off the surface and using as few wheels as possible to minimize surface attraction, 3) having rigid chassis and short axles to prevent the chassis from sagging towards the surface to again minimize surface-chassis attraction.¹⁷⁰ Overall, the key factor improving diffusion for a given molecular weight is to minimize surface attraction by rational molecular design. We believe elevation weighted density is a good quick estimate of nanocar performance as it takes into account the key features highlighted by these nanocar racers. By definition, it takes both molecular weight and molecular geometry into account. Moreover, as

the calculation is performed on the surface adsorption geometry the configurational changes of the molecule is also introduced. This is supported by the linear correlation between elevation weighted density and free energy barrier of diffusion for both directions as seen in Figure 23c and 23e.

4.1.3 Conclusion

In summary, we employed classical MD simulations and TST calculations to predict surface diffusion of large organic molecules. We found that using a relatively simple and computationally inexpensive calculation i.e. rigid body MD simulations, it is possible to estimate the relative diffusion between different molecules. Moreover, we showed that the diffusion gets slower with higher molecular weight and stronger molecule-surface interaction energy. We suggested a geometric parameter, i.e. elevation weighted density, which can be easily calculated using the surface adsorption geometry of the molecules. We show that this parameter could be used to quickly rank diffusion of different molecular designs. Furthermore, we show that it is possible to employ a more computationally expensive transition state theory (TST) approach to estimate the timescale of diffusion. This includes increasing vdW interactions between the molecule and the surface and calculating free energy barrier for diffusion with umbrella sampling of rigid MD simulations. Overall, as highlighted by nanocar racers we suggest minimizing the surface adhesion energy is a good strategy to improve diffusion for a given molecular weight. One way to achieve this is to elevate the bulk of the molecule from the surface by using various molecular components (e.g. wheels).

Careful design of the molecular structure and selection of the appropriate surface can enable precise manipulation of the molecular diffusion. We believe these tools can be used to advance design of molecular structures to control their motion and play an important role in the design of

nanocars. Large screening studies can be employed and molecular designs can be ranked quickly using elevation weighted density or quick rigid MD simulations. After identifying promising designs, more rigorous calculations can be performed to rank different molecular designs more accurately.

4.2 Nanocar Builder Tool

With the purpose of designing new nanocars we developed a nanocar builder tool integrated with Avogadro 2 molecular visualizer.¹⁸³ Using the builder, nanocars can be assembled from a collection of chassis and wheel molecular components. Metal slabs with arbitrary size and geometry can be built and the nanocar can be placed on a metal surface. Finally, a LAMMPS¹⁵⁸ Molecular Dynamics configuration file can be exported to study diffusion of the nanocar on the metal surface. We believe this builder complements our efforts in developing a robust method to estimate surface diffusion of nanocars. We hope current nanocar designs can be improved through computational studies by applying the methods highlighted in Section 4.1 to the hypothetical nanocars generated using this software package.

4.2.1 Methodology

Initially a set of wheel and chassis molecular components were selected from previously studied nanocar molecules.⁹ The molecular geometries were optimized using Kohn-Sham density functional theory at BP86-D3/Def2-SVP level of theory as implemented in ORCA.¹⁸⁰ The current release of the nanocar library includes 12 wheel molecules and 4 chassis molecules as shown in Figure 24.

Then, available software packages were assessed for the user interface and Avogadro stood out with a large userbase with over one million downloads and a new user-friendly Python plug-in interface which enables easy integration of custom workflows into a molecular visualizer.

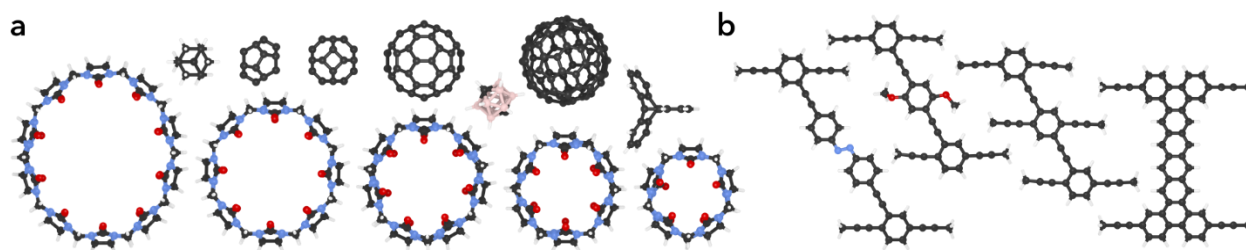


Figure 24 Nanocar builder plug-in library: (a) wheel molecules; (b) chassis molecules. Using the plug-in users can select a chassis molecule, connect wheels, build a metal surface, and setup an MD simulation configuration for LAMMPS software.

As the nanocar building process requires extensive geometric operations, a complementary Python package (Ångström¹⁸⁴) was developed to accommodate that. To build a metal surface ASE¹⁸¹ surface builder was integrated in the plug-in and a custom LAMMPS writer was developed to setup rigid MD simulations using Universal Force Field¹⁰¹ parameters. During the development, the MolSSI best practices were adopted including version control, unit testing and coverage, code styling, continuous integration and full documentation. A video and written tutorial for the nanocar builder is available from the GitHub repository.¹⁸⁵ Users can easily follow instructions on the web site to install Avogadro with the nanocar builder plug-in and start building. A screenshot of the plug-in can be seen in Figure 25. Below is a quick summary of the nanocar building process.

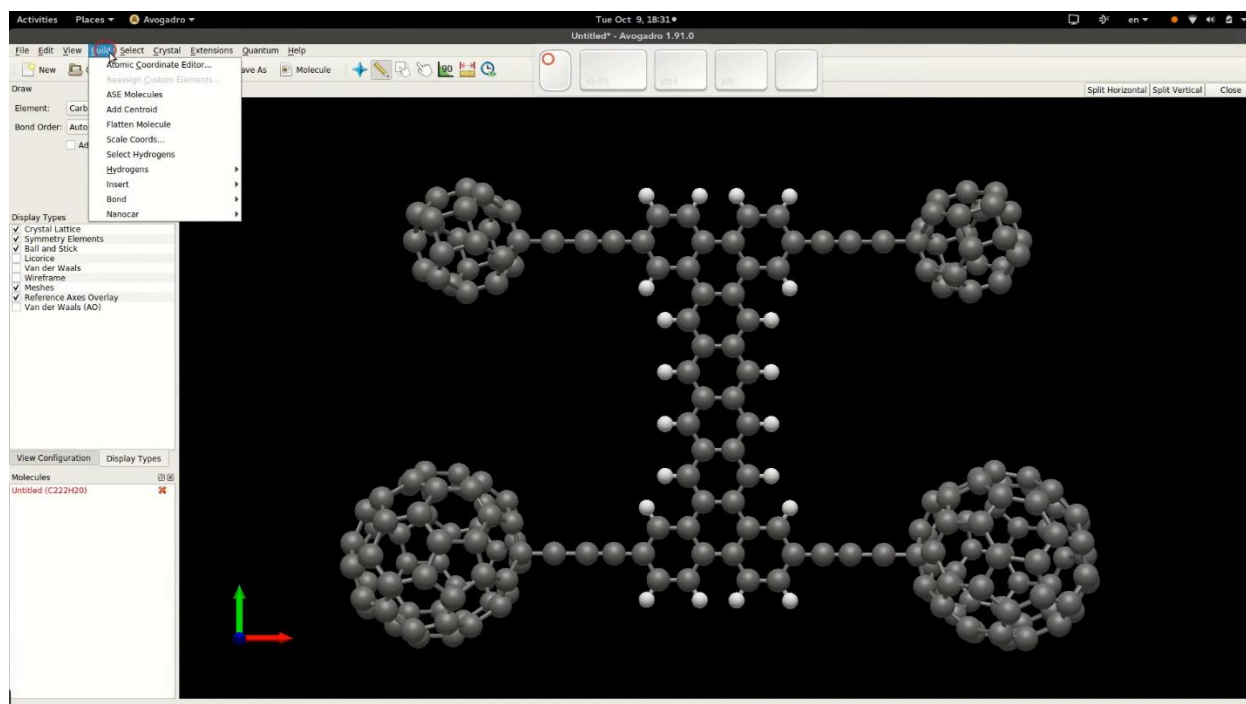


Figure 25 A screenshot of the nanocar builder Avogadro 2 plug-in. After installation a “Nanocar” menu appears under the build option which can be used to add chassis molecules, connect wheel molecules, add a custom metal surface, and export LAMMPS configuration files.

4.2.2 How to Build a Nanocar?

The nanocar building process starts by adding a chassis molecule. Then, wheels are connected either covalently or mechanically (interlocking) to the selected atoms of the chassis molecule. After all the wheels are connected then a custom metal surface is built and placed parallel to the chassis of the nanocar (see Figure 26). Lastly, a LAMMPS configuration file can be generated to test drive the nanocar with MD simulations.

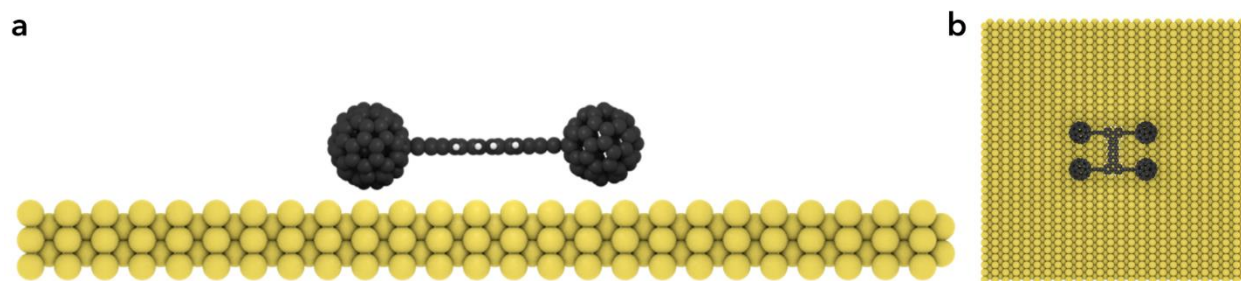


Figure 26 A nanocar molecule placed on a Au (110) surface built using the nanocar builder: (a) side view and (b) top view. Surface is approximately 5 nm x 5 nm and the nanocar molecule is approximately 1 nm in length.

Currently, we are working towards implementing the builder as a Python library to enable automated building of nanocars. Moreover, with the addition of parametric building blocks such as variable length chassis or variable size wheels, structural parameters that affect diffusion of nanocars can be studied. Another feature we are working on is setting up multibody MD simulations by grouping chassis and wheel molecular components as separate rigid bodies that are bonded together. Previous work by Akimov et al. has shown that experimentally observed wheel rotation can be simulated using this approach.¹²

With the upcoming 2nd International Nanocar Race, our nanocar builder can be used to improve nanocar designs by understanding how the molecular components of the nanocar affect the diffusion behavior. We believe the tools developed in this work will collectively help to push the frontier of knowledge (even if incrementally) towards the eventual building of useful AMMs.

Appendix A Discovery of Hypothetical Hetero-Interpenetrated MOFs

Appendix A.1 Algorithm Description

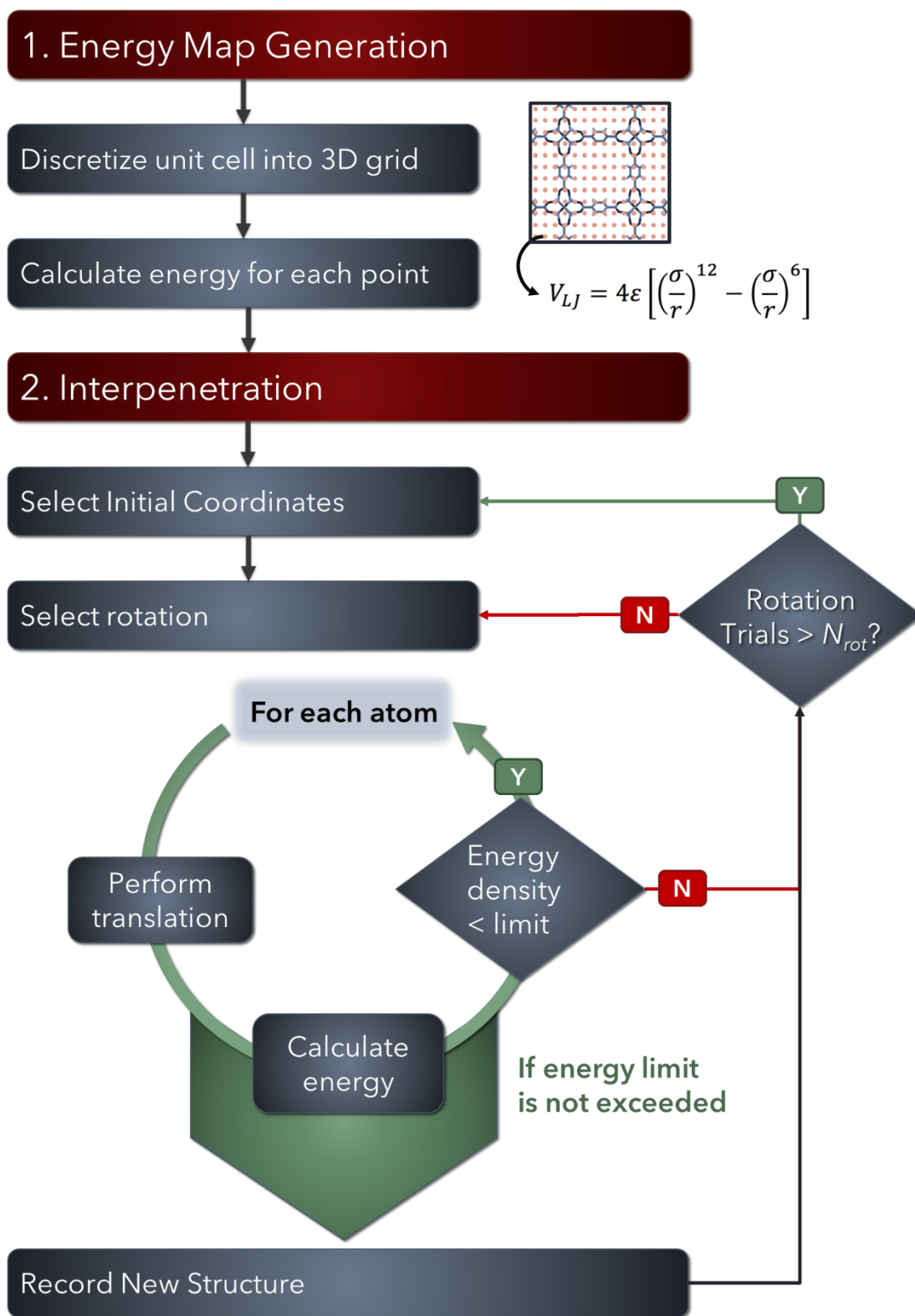
The algorithm tests whether two given crystal structures with any topology can theoretically interpenetrate each other. For two given unit cells, different orientations of the unit cells are checked for collisions and any favorable orientations are reported. Our main aim was to screen a large database to identify new interpenetrated structures therefore we needed a method that would rapidly identify possible interpenetration candidates. Moreover, we knew most of the combinations would be unfavorable for interpenetration therefore using a high accuracy model would result in wasting computer time. For that reason, we developed the “IPMOF” algorithm to rapidly identify which MOF pairs can possibly interpenetrate each other.

Initially, two MOFs are selected and one of them is designated as *passive* and the other as *active* (see Appendix Figure 5). For the *passive* MOF, an *energy map* is generated to calculate energy penalty associated with interpenetrating it with the *active* MOF. Secondly, different orientations of *active* MOF are tested by moving and rotating the structure. We did not consider improper rotation while testing different orientations. An *energy density* is calculated for each orientation and if the *energy density* is below the selected threshold value orientation is saved. After all orientations are tested, most favorable ones are identified according to *energy densities*.

This initial test is referred as *single unit-cell test* since it only considers interpenetration between single unit cells of two given MOFs. However, it is possible to observe atomic collisions in repeating unit cells even if there were no collisions in the single unit cells. For MOF pairs which pass the *single unit cell test*, *multiple unit-cell collision test* is performed to make sure that

differences in repeating patterns of the unit cells do not cause overlap when they are extended multiple times. Next step is to generate a supercell for the interpenetrating MOFs, which allows both structures to repeat according to their symmetry. After this step is complete a structure file for the hypothetical interpenetrated MOF is generated.

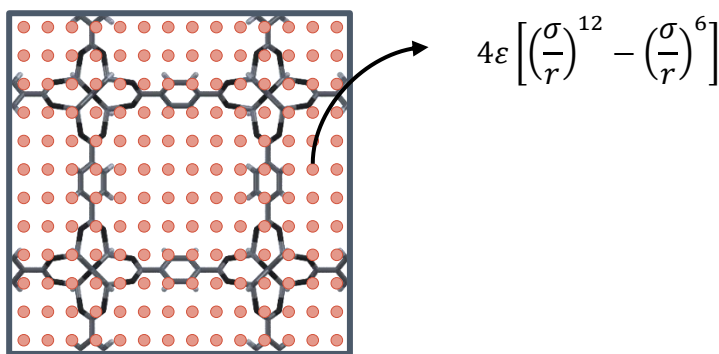
The algorithm is provided here (<https://github.com/kbsezginel/IPMOF>) where detailed documentation is also included for the software. In addition, detailed examples on how to use the algorithm are also provided in Jupyter notebooks. We tried to make it as easy as possible for others to use our software in order to help the community explore new interpenetrated materials. Following the documentation, it is relatively easy to perform simulations on a personal laptop with minimum programming experience. Our aim here was to make sure our algorithm can be beneficial for both experimental and computational scientists. Moreover, we provided the candidate structures discovered in this study with extensive structural and crystallographic information as well as references to publications in which the MOFs used in this study were reported.



Appendix Figure 1 Flowchart for IPMOF algorithm. Algorithm and its documentation with examples are provided here: <https://github.com/kbsezginel/IPMOF>.

Appendices contain supplementary or illustrative material or explanatory data too lengthy to be included in the text or not immediately essential to the reader's understanding of the text.

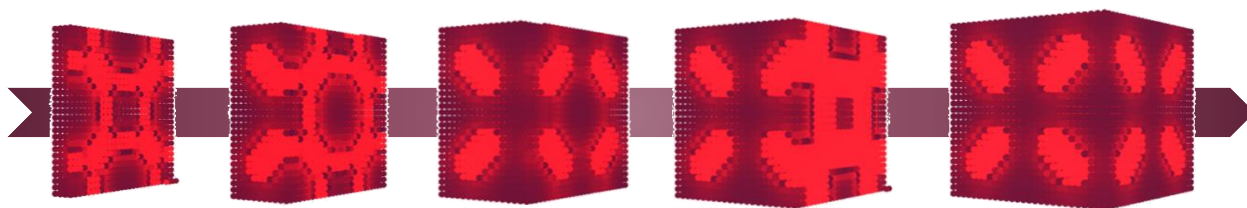
Energy Map Generation. The *energy map* is defined as a regular grid of points representing the interatomic potential energy of the unit cell (see Appendix Figure 2). The potential energy for each point in the grid is calculated using Lennard-Jones potential¹⁰⁰ and Universal Force Field¹⁰¹ (UFF) parameters with Lorentz-Berthelot mixing rules and a cut-off radius of 12 Å.



Appendix Figure 2 Energy map schematic for MOF-5. Each red point represents grid points 1 Å apart in 3 dimensions. For each point potential energy is calculated using Lennard-Jones equation.

In Appendix Figure 3 *energy map* generation process for MOF-5¹⁸⁶ is provided. As expected, empty regions in the unit cell are lower in energy (shown in dark red) and atomically crowded regions are higher in energy (light red). The *energy map* shown below is calculated using UFF parameters of a carbon atom which provides energetic information for inserting a carbon atom to any location in the unit cell. Each type of atom results in a different energy value for the grid points of the *energy map*, therefore the *energy map* array consists of 3D coordinates as well as different energy values for each type of atom used in the calculation of the *energy map*.

For high throughput screening energy values for various atom types are required to test interpenetration. However, this would result in having tens of energy values for each position in the *energy map*. To avoid having large *energy map* files force field parameters were simplified to only include total 11 atom types and consequently 11 energy values for each position in *energy map*.



Appendix Figure 3 Energy map generation process for MOF-5. The potential energy increases from dark red to light red.

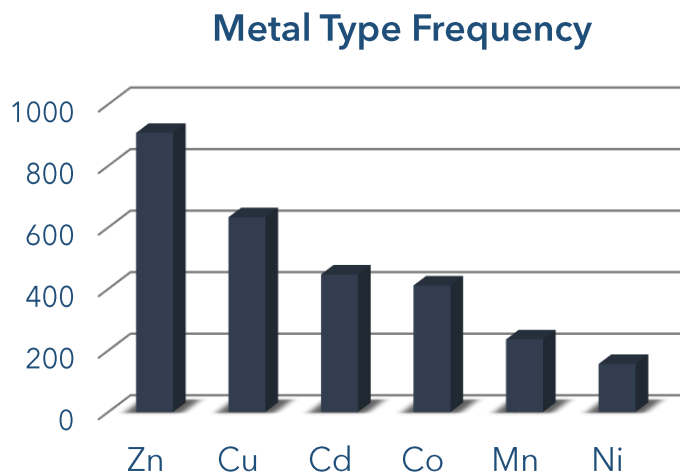
Force Field Parameters. Lennard-Jones equation is used to estimate interatomic potentials (Eq. 2-1) where ϵ and σ values used for atoms are listed below and r is the distance between atoms in Å. The resulting energy is in $K.k_B$ units (0.0083144621 kJ/mol).

As mentioned in section A1, for high throughput screening, energy values for various atom types are required to test interpenetration. This would be computationally expensive and the generated *energy map* files would take a lot of space. However, all MOFs are composed of organic linkers and metal cluster which suggests that almost all MOFs will have C, H, O, N atoms and one or more metal atoms. Making use of this information we decided to use a simplified force field by only considering actual UFF parameters for 10 atoms and assigning dummy force field parameters for the rest. In this way, we only needed to calculate 11 different energy values for each position

in the *energy map* instead of almost a hundred. In addition to C, H, O, N atoms for organic linkers we identified the 6 most frequent metal atoms in the database (Appendix Figure 4).

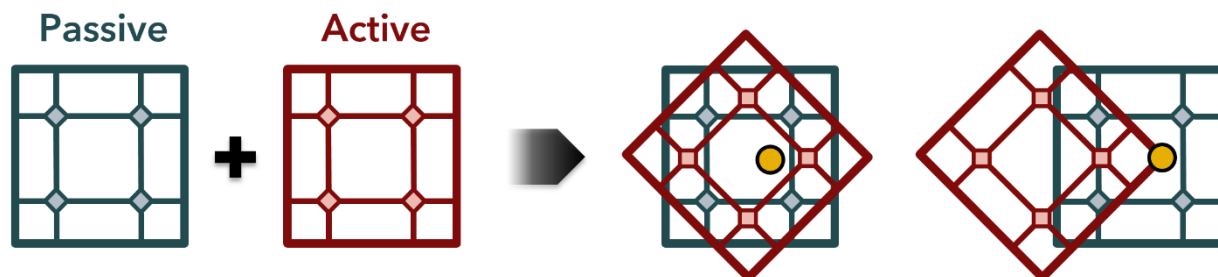
Appendix Table 1 Force field parameters used in this study

Atom	σ (Å)	ϵ/k_B (K)
C	3.430851	52.87336
Cd	2.53728	114.8107
Co	2.558661	7.049781
Cu	3.113691	2.517779
H	2.571134	22.15645
Mg	2.691405	55.89469
Mn	2.637951	6.546225
N	3.260689	34.74535
Ni	2.524807	7.553337
O	3.118146	30.21335
Zn	2.461553	62.44092
Dummy	3	30



Appendix Figure 4 Number of MOFs with given metal type observed in the database

Algorithm Parameters. We defined several algorithm parameters to introduce flexibility for various crystal structure pairs.



Appendix Figure 5 Interpenetration process for two cubic MOFs. Blue framework is the passive framework and red framework is the active framework. The active framework is first rotated and then translated to next point depicted by the yellow point.

Grid size: The grid size is defined as the distance between grid points of the *energy map* in each dimension. The *energy map* is generated as a 3D rectangular grid that surrounds the unit cell. For high-throughput screening we used grid size of 1 Å for the generation of *energy map*.

Interpolation: When an energy value is needed at a position that does not fall exactly on a grid point in the *energy map*, which is the usual case, interpolation is used. For high-throughput screening we used trilinear interpolation which approximates the value of a point in a regular grid linearly using data in the lattice points.

Cut-off distance: The cut-off distance used in the calculation of interatomic potentials. Any atom pair that are further away from this distance were assumed to have no interaction. For high-throughput screening cut-off distance was taken as 12 Å.

Extension cut-off distance: The extension cut-off distance is used to determine the number of extension that will be performed on the unit cell for multiple unit cell collision test. For a given distance the unit cell is extended in each dimension to make sure that it covers an area at least the

size of a sphere with radius of that distance. For high-throughput screening extension cut-off was taken as 50 Å.

Rotational freedom: The increments of rotation performed on the active unit cell to obtain different orientations. For high-throughput screening only 90° rotations were considered.

Rotational limit: The number of times a rotation is performed for same initial coordinate. For high-throughput screening all possible 90° rotations (24 total) were performed for each point.

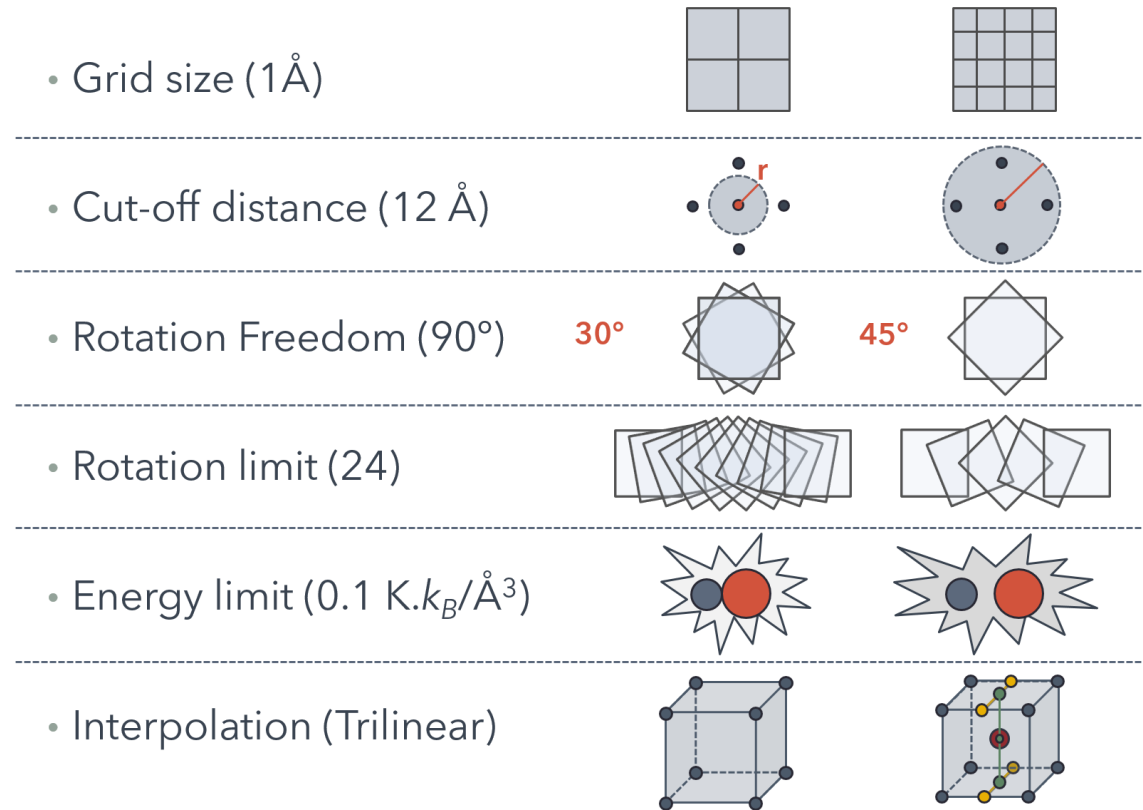
Energy limit: There are three types of energy limit defined in the algorithm: atom energy limit, structure energy limit, and energy density limit. The energy limit parameter affects the allowed contact distance between the frameworks, therefore using high energy limits may results in unphysical contact distances.

- Atom energy limit is the maximum allowed energy for insertion of a single atom.
- Structure energy limit is the maximum allowed energy for insertion of a collection of atoms that constitute the active structure. It is calculated by summing the insertion energies for each atom in the unit cell.
- Energy density limit is similar to structure energy limit however it is divided by the unit cell volume to make it more comparable among different structures. For unit cells with different sizes constituting different number of atoms we chose to have a universal energy limit scaled by the volume of the cell. The energy density, ρ_{energy} , is calculated according to Eq. A-1,

$$\rho_{energy} = \frac{\sum_{i=0}^{N_p} \sum_{j=0}^{N_a} V_{LJ}(i, j)}{V_{cell}} \quad \mathbf{A-1}$$

where N_p and N_a are number of atoms in active and passive MOFs; i and j are atom indices for passive and active MOFs; V_{LJ} is interatomic potential (Lennard-Jones) energy, and V_{cell} is unit cell volume in \AA^3 .

There are additional algorithm parameters available for user to manipulate how the structures are generated, how the data is reported etc. however these parameters do not affect the interpenetration. More information on algorithm parameters can be found in algorithm documentation.



Appendix Figure 6 Algorithm parameters with values used in this study shown in parenthesis. Energy density

limit of 0.1 $\text{K.k}_B/\text{\AA}^3$ corresponds to 0.83144621 J/mol \AA^3 .

For the high-throughput screening of the MOF database we selected a set of simulation parameters that we believe would yield a good amount of successful trials in a reasonable amount of time. In theory, it is possible to discover interpenetrated structures that were not found in this screening. Our aim in this study was to introduce a new method that allows testing whether two given periodic structures can interpenetrate each other. The screening study performed here was performed to make an initial estimate for possible interpenetrations rather than exploring the whole possible orientations for two given MOFs.

Appendix A.2 Generating Unit Cell for Interpenetrating Structures

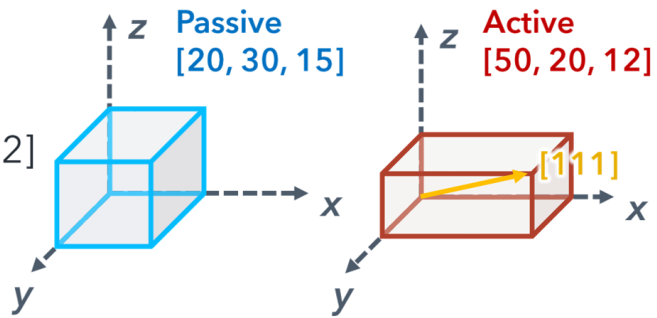
Calculating Supercell Parameters. The lattice parameters for the combined unit cell are calculated by several geometric operations:

1. First [111] vector for the active unit cell is converted to fractional coordinates using lattice vectors of passive unit cell. In other words, the [111] vector of passive unit cell is converted to coordinate system of the passive unit cell. This vector represents how active unit cell repeats in terms of the passive unit cell. To make sure both unit cells repeat symmetrically in a supercell we need to calculate new lattice parameters.
2. The lattice parameters are calculated by finding the least common integer multiple for each dimension of the fractional [111] vector. This gives the number of repeats required for the active unit cell. Multiplying these with fractional coordinates of [111] vector gives number of repeats required for the passive unit cell.

3. The unit cells are aligned and repeated (extended) according to calculated parameters and the supercell is generated using the supercell parameters which can be calculated by multiplying number of repeats for passive unit cell with its original unit cell parameters.

Example case:

- Find $[111] \rightarrow [50, 20, 12]$
- Convert to fractional
 - $[5/2, 2/3, 4/5]$
- Find least common multiple
 - $[2, 3, 5]$
 - $[2, 3, 5] \times [5/2, 2/3, 4/5] \rightarrow [5, 2, 4]$
- Extend both unit cells to the common unit cell
 - **Passive** $\rightarrow [5, 2, 4] \rightarrow [100, 60, 60]$
 - **Active** $\rightarrow [2, 3, 5] \rightarrow [100, 60, 60]$



Appendix Figure 7 Example case for supercell parameters calculation

Since lattice parameters have high resolution (4,5 significant figures) the combined unit cells would generally become huge and impractical. To avoid that we allowed the active unit cell to tolerate lattice parameter changes up to 1%. This allows us to constrain the combined unit cell to 100 repeats for any of the unit cells. Moreover, to make sure the active unit cell conserves its symmetry, we scaled the positions of the atoms according to adjustment we made to the lattice parameters. For example, if the a vector is enlarged by 0.3% then all distances in that direction are multiplied by 1.003.

Cell Distortion. The cell distortion is defined as the scaling required to perfectly combine unit cells with a selected tolerance. Cell distortion is calculated by summing percent change in atomic coordinates for each vector of the unit cell. This means with a given 1% tolerance the total cell distortion is less than or equal to 3%. For the calculation of supercell parameters 1% tolerance was used to ensure low cell distortion. However, candidate structures with very large supercells were not generated. It is possible to increase the tolerance and obtain a smaller supercell. For void fraction calculations reported in the manuscript, two of the candidate structures were generated using 2% tolerance which resulted in a much smaller supercell with a total of ~4% cell distortion. Example Jupyter notebook for supercell generation is provided in the GitHub repository (github.com/kbsezginel/IPMOF).

Appendix A.3 High-throughput Screening

Database Selection. For high-throughput MOF database created by Chung and co-workers⁹⁸ has been used. In addition to the structures proposed in this study, 1005 additional MOFs were added to the final database (total 6014 MOFs). The additional MOFs have been generated using the same methodology explained in that study.

MOF Combination Selection. To eliminate MOF combinations that are physically capable of resulting in interpenetration, only MOF combinations that have a total void fraction bigger than 1.0 are considered. To explain this better, we can imagine a unit cell of a MOF as a glass of water where the atoms in the unit cell would be analogous to water in glass (Appendix Figure 8). We can also imagine interpenetration as combining these two glasses of water into a single glass (or single unit cell). Thus, to have enough space for interpenetration the total water amount in the

glasses should be less than 100 % or in the MOF case the total void fraction of the MOFs should be bigger than 1.0.



Appendix Figure 8 Analogy for MOF combination selection. The interpenetrating MOFs must have enough empty space in their unit cell so when they form a single unit cell there is enough space for both frameworks.

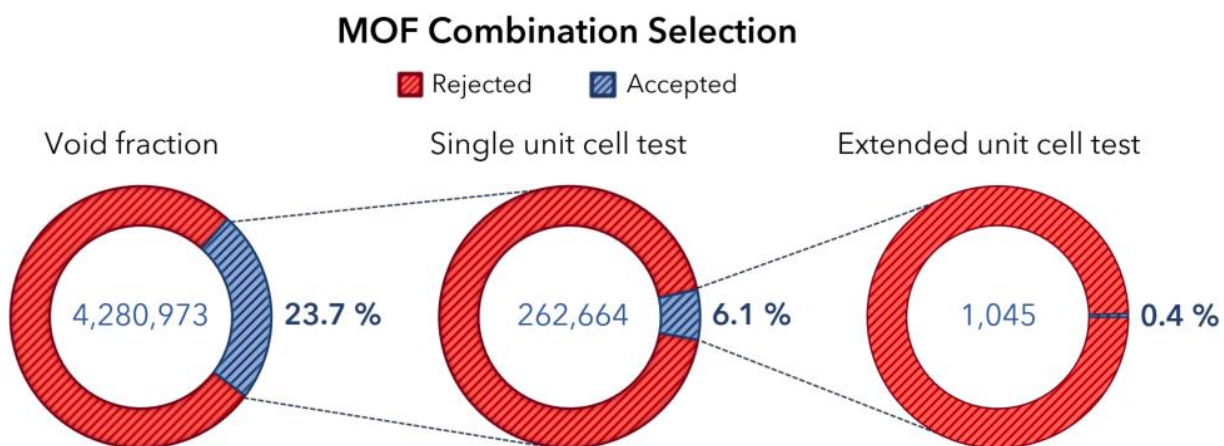
This can be imagined as filling two glasses of water into a single glass. In order to avoid overflowing the glasses should have enough empty space.

The total possible combinations correspond to combination of two of 6014 which comes to around 18.1 million combinations. When the physically impossible combinations are eliminated the total number of combinations come down to around 4.28 million which is a little less than quarter of total possible combinations.

$$\binom{6014}{2} = \sim 18.1 \text{ million} \xrightarrow{V_{f1} + V_{f2} > 1.0} \sim 4.3 \text{ million}$$

Void Fraction Calculation. The void fraction of the MOFs in this study are calculated using RASPA 2¹⁸⁷, a general purpose classical simulation package that can be used for the simulation of molecules in gases, fluids, zeolites, aluminosilicates, metal-organic frameworks, carbon nanotubes and external fields. <https://github.com/numat/RASPA2>

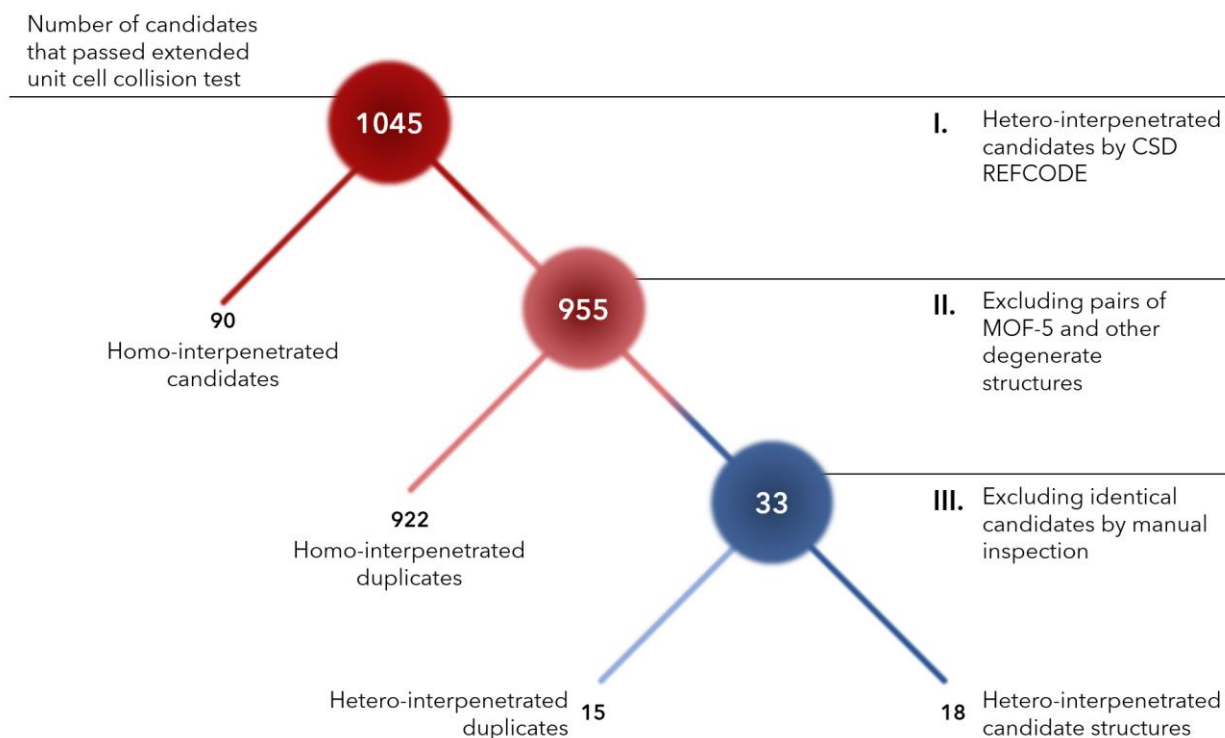
Analysis of Candidate Structures. Initially single unit-cell interpenetration tests were performed for ~4.3 million MOF pairs and ~6% of these pairs resulted in favorable orientations. The extended unit-cell test on these MOF pairs resulted in a total of 1045 MOF pairs which were identified as candidate interpenetrating structures (Appendix Figure 9).



Appendix Figure 9 Number of MOF pairs in different steps of high-throughput screening

Further analysis of these MOF pairs showed that most of these structures were homo-interpenetrated due to degenerate MOFs in the database. Total 113 MOFs were identified to form 1045 candidate structures and among these 113, 46 of them were found to be MOF-5 degenerate structures. Among the 1045 candidate structures, 1012 of them were identified as homo-interpenetrating where 92 of them were determined as pairs with same CCDC reference codes and 922 of them were determined as pairs of degenerate MOFs under different reference codes. 33 hetero-interpenetrating candidates were examined and 15 of them were found to be duplicate pairs resulting in 18 unique pairs of hetero-interpenetrating MOFs (see Appendix Figure 10). Among the hetero-interpenetrating candidates following topologies were observed: *pcu+pcu*, *the+tbo*,

ftw+ftw, *tbo+ntt*, *scu+tfe*, *reo-e+ftw*, *gee+ftw*, *ntt+pcu*, *tbo+pcu*. More information about all MOFs and all candidate structures are provided in Ref¹⁰⁶.



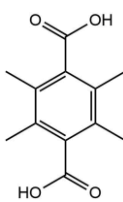
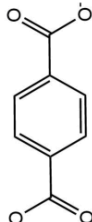
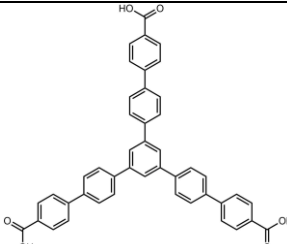
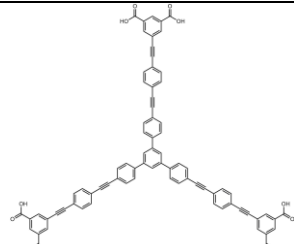
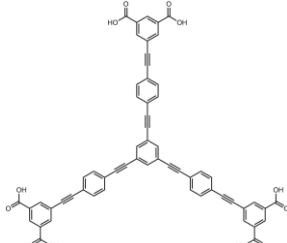
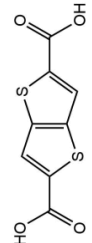
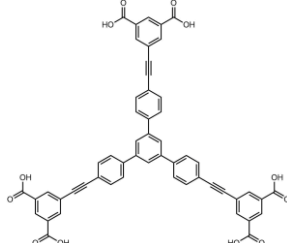
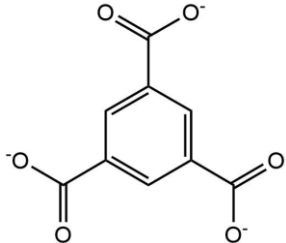
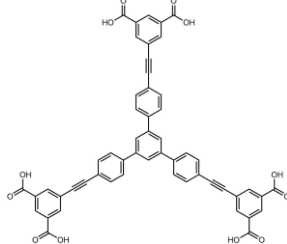
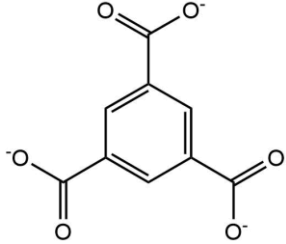
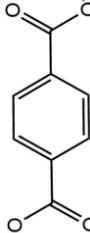
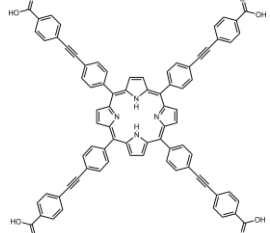
Appendix Figure 10 Analysis of candidate structures to find hetero-interpenetrated pairs (Starting from 1,045 candidates that passed the extended collision test, 90 of them were pairs of same MOFs according to their CSD reference codes [Step I]. From the remaining 955 candidates, pairs of MOFs that have different reference codes but are degenerate structures (922) are removed [Step II]. Remaining 33 candidates were inspected manually by comparing chemical formulas, crystallographic information and visually examining image renders of MOFs [Step III]. 15 more candidates were removed and 18 candidates were presented as hetero-interpenetrated candidate MOFs.

For candidate hetero-interpenetrated structures, supercells were calculated with 1% distortion tolerance and cif files were generated. The candidates which resulted in unpractically large supercells were generated with higher tolerance resulting in higher cell distortion. The candidate

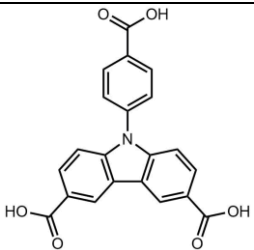
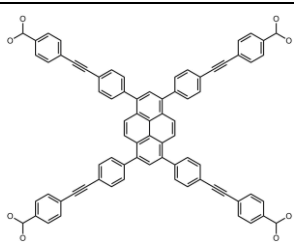
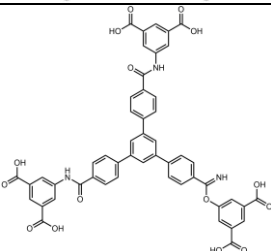
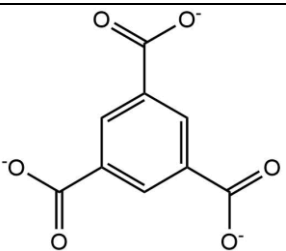
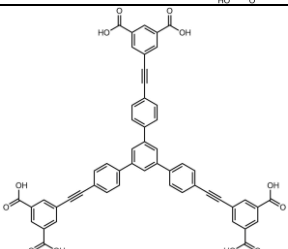
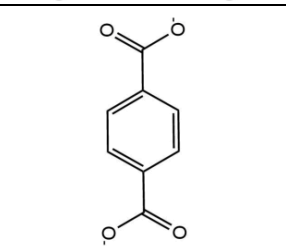
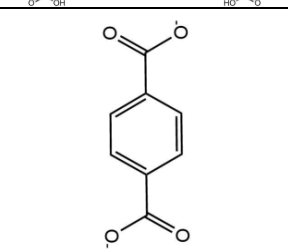
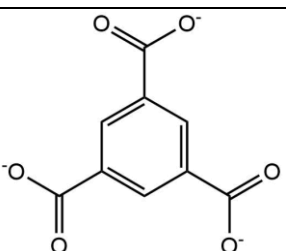
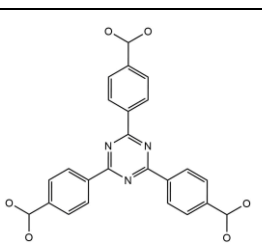
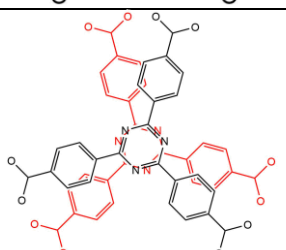
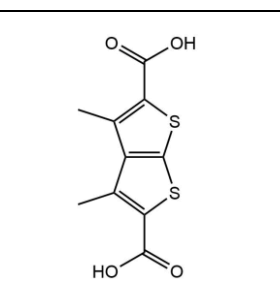
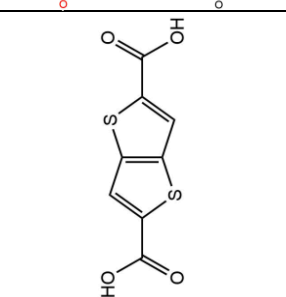
crystallographic information files (cif) are provided in GitHub repository (github.com/kbsezginel/IPMOF). In addition to regular structure files each candidate also has a colored version (for easy visual inspection) where each atom in the interpenetrating frameworks are replaced with carbon and oxygen atom for passive and active MOFs respectively.

Additionally, experimental synthesis procedure and chemical composition of the 18 candidate structures were analyzed. Metal centers and organic linkers that compose each MOF are presented below with crystallographic information.

Appendix Table 2 Chemical composition information for 18 hetero-interpenetrating MOF candidates

#	Candidate	Formula*	Supercell	Linker 1	Linker 2
1	AXUBAW [IRMOF-18] + NODTIL [IRMOF-1]	ZnTMBDC [C ₇₂ H ₇₂ O ₂₆ Zn ₈] + ZnBDC [C ₄₈ H ₂₄ O ₂₆ Zn ₈]	[1 1 1] + [1 1 1] D: 1.1072		
2	BAZGAM [MOF-399] + SEMNIJ [NU-110]	CuBBC [C ₃₆₀ H ₂₁₆ Cu ₁₂ O ₄₈] + Cu L [C ₆₂₄ H ₂₈₈ Cu ₂₄ O ₉₆]	[1 1 1] + [1 1 1] D: 1.7241		
3	HABQUY [PCN-610] + VEBHUG [IRMOF-20]	CuTTEI [C ₄₈₀ H ₁₉₂ Cu ₂₄ O ₉₆] + ZnTTDC [C ₄₈ H ₁₂ O ₂₆ S ₁₂ Zn ₈]	[8 8 22] + [49 49 45] D: 2.3537		
4	HABRAF [PCN-68] + HANHAH [ZnBTC]	CuPTEI [C ₄₃₂ H ₁₉₂ Cu ₂₄ O ₉₆] + ZnBTC [C ₇₂ H ₂₄ O ₄₈ Zn ₁₂]	[1 1 1] + [2 2 2] D: 0.8743		
5	HABRAF [PCN-68] + XADDIR [CuBTC]	CuPTEI [C ₄₃₂ H ₁₉₂ Cu ₂₄ O ₉₆] + CuBTC [C ₇₂ H ₂₄ Cu ₁₂ O ₄₈]	[1 1 1] + [2 2 2] D: 0.2717		
6	IZEPAF [MIL-hypo-1] + WUH DAG [NU-1104]	CrBDC [C ₂₈₈ H ₁₄₄ Cr ₃₆ O ₁₅₆] + ZrPor-PTP [C ₂₄₀ H ₁₃₀ N ₁₂ O ₃₂ Zr ₆]	[43 43 43] + [42 42 42] D: 2.8926		
7	JUTCW + PIYZAZ	[Cd(CN) ₂] + [Cd(C ₂) ₂]	[1 1 1] + [1 1 1] D: 1.9544	$\text{C}\equiv\text{N}$	$\text{C}\equiv\text{C}$

Appendix Table 2 continued

8	<p>KOZQEX [DUT-75] + WUHCUZ [NU-1103]</p>	<p>CuPCDC [C₂₅₂H₁₂₀Cu₁₈N₁₂O₇₂] + ZrPy-PTP [C₂₂₈H₁₁₈O₃₂Zr₆]</p>	<p>[1 1 1] + [1 1 1] D: 0.7444</p>		
9	<p>LEHXUT + XAMDUM02 [CuBTC]</p>	<p>CuBBC [C₄₀₈H₂₁₆Cu₂₄N₂₄O₁₂₀] + CuBTC [C₇₂H₂₄Cu₁₂O₄₈]</p>	<p>[1 1 1] + [2 2 2] D: 0.1275</p>		
10	<p>LURRIA [PCN-68] + MIBQAR06 [IRMOF-1]</p>	<p>CuPTEI [C₄₃₂H₁₉₂Cu₂₄O₉₆] + ZnBDC [C₄₈H₂₄O₂₆Zn₈]</p>	<p>[1 1 1] + [2 2 2] D: 2.3519 D: 0.1149</p>		
11	<p>PEVPUD [IRMOF-1] + XAMDUM04 [CuBTC]</p>	<p>ZnBDC [C₄₈H₂₄O₂₆Zn₈] + CuBTC [C₇₂H₂₄Cu₁₂O₄₈]</p>	<p>[1 1 1] + [1 1 1] D: 2.3791 D: 2.9419</p>		
12	<p>PIBNUK [ZnTATB] + PIBPIA [CdTATB]</p>	<p>ZnTATB [C₁₉₂H₉₆N₂₄O₄₈Zn₁₂] + CdTATB [C₁₉₂H₉₆Cd₁₂N₂₄O₄₈]</p>	<p>[43 43 43] + [42 42 42] D: 2.8962</p>		
13	<p>TEQPEN [IFMC-28] + VEBHUG [IRMOF-20]</p>	<p>ZnDMTDC [C₆₀H₃₆O₂₆S₁₂Zn₈] + ZnTTDC [C₄₈H₁₂O₂₆S₁₂Zn₈]</p>	<p>[1 1 1] + [3 3 1] D: 0.1337</p>		

Appendix Table 2 continued

14	<p>TOVGAO [PCN-228]</p> <p>+</p> <p>JOZWIG02 [NU-1102]</p>	<p>ZrTCP-1 [C₂₁₆H₁₂₄N₁₂Ni₃O₃₂Zr₆]</p> <p>+</p> <p>ZrPor-PP [C₂₁₆H₁₃₀N₁₂O₃₂Zr₆]</p>	<p>[1 1 1] +</p> <p>[1 1 1] D: 0.1516</p>		
15	<p>UQOFOX [PCN-528]</p> <p>+</p> <p>VEHJUP</p>	<p>MnTTPP [C₉₆H₅₆Mn₆N₄₀]</p> <p>+</p> <p>Zn_{3,4} BTC [C₁₀₈H₃₆O₇₂Zn₂₂]</p>	<p>[23 1 1] +</p> <p>[22 23 1] D: 1.5778 D: 1.1833</p>		
16	<p>VETSUK [POST-65(Co)]</p> <p>+</p> <p>HEXVEM [mesoMOF-1]</p>	<p>CoHMTT [C₅₇₆H₄₃₂Cl₁₂Co₂₆O₁₄₄]</p> <p>+</p> <p>CuTATAB [C₁₉₂H₁₂₀Cu₁₂N₄₈O₄₈]</p>	<p>[1 1 1] +</p> <p>[1 1 1] D: 1.2227</p>		
17	<p>VETTAR [POST-65(Ni)]</p> <p>+</p> <p>HEXVEM [mesoMOF-1]</p>	<p>NiHMTT [C₅₇₆H₄₃₂Cl₁₂Ni₂₆O₉₆]</p> <p>+</p> <p>CuTATAB [C₁₉₂H₁₂₀Cu₁₂N₄₈O₄₈]</p>	<p>[1 1 1] +</p> <p>[1 1 1] D: 0.7567</p>		
18	<p>RUTNOK [IRMOF-76]</p> <p>+</p> <p>VEJHEZ [MMPF-4]</p>	<p>Zn L0 [C₆₉H₄₅N₆O₁₃Zn₄]</p> <p>+</p> <p>ZnTDCPP [C₁₅₆H₆₀N₁₂O₅₀Zn₁₉]</p>	<p>[1 1 1] +</p> <p>[1 1 1] D: 0.7355</p>		

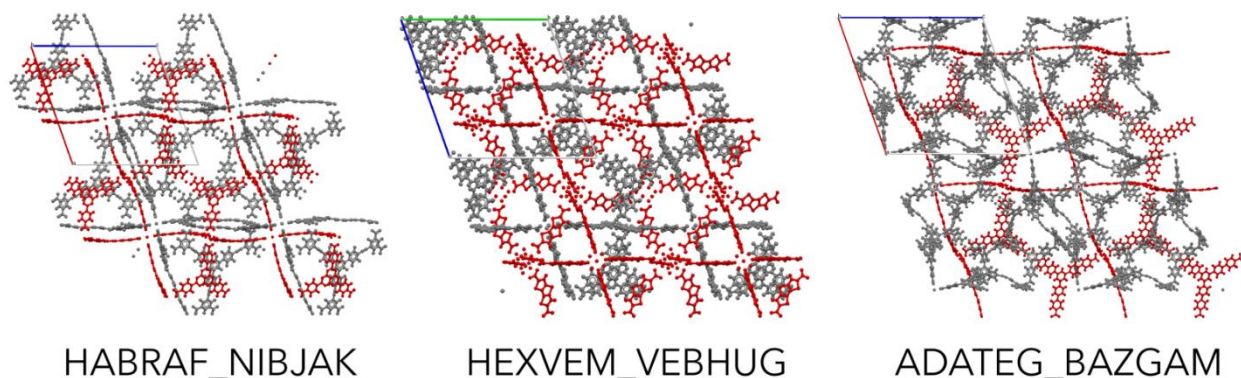
Notes:

- The red color represents the MOFs which can also *homo-interpenetrate*. The candidates where both MOFs are black in color are more likely to form *hetero-interpenetration* since *in theory* both MOFs don't interpenetrate with themselves.
- The formulas are just simplification of metal types and linkers. Even though two MOFs have the same metal type and linker (e.g. UQOFOX and HANHAH) they could have different structures.
- Supercell column has information on number of extensions required to form supercell for each of the MOFs. (e.g. [1 1 1] + [2 2 2] means MOF1 needs to be extended to [1 1 1] and MOF needs to be extended to [2 2 2] in x, y, z dimensions to form the supercell). The D value gives the distortion for supercell in percentage.
- Hashed bonds imply 90 degree rotations around the bonding axis.

Appendix A.4 Comparison with Literature

Comparison of Candidate Structures. An example comparison of results between our method and another method proposed by Kwon et al.¹⁸⁸ is provided. In their work, Kwon and co-workers developed an algorithm that can identify interpenetration of MOFs with orthogonal unit cells. They used their algorithm to screen the CoRE⁹⁸ database and provided a list of 113 candidates in Table S2 of their Supplementary Information. Comparing this list with our candidates list, we found out that 16 candidates included MOFs that weren't present in our database of 6014 MOFs. From the rest of 97 candidates, 45 of them were also present in the candidate list we provided. For the 52 candidates remaining, our calculations didn't find any interpenetrating pairs due to our selection of simulation parameters.

In the database used in this study, almost all MOFs are reported in their primitive unit cell. For cases where we are testing interpenetration of MOFs with non-orthogonal unit cells, 90-degree rotations may be insufficient to find the interpenetration. In the study by Kwon et al. they first converted all primitive unit cells of orthogonal MOFs to their conventional orthogonal cells and tested interpenetration after that. If we were to do the same before running interpenetration tests, 90-degree rotations would be sufficient to find the same pairs as well. However, using primitive unit cells, smaller rotational increments are necessary to find the interpenetrating configurations. It is important to point out that the frameworks obtained depend not just on the method, but also the parameters used. In this paper, we have described a rather general method, and as a demonstration we show results we obtained from choosing a *particular* set of parameters. Any reader can use our code, which we make freely available, and change the parameters to better suit their interests. Below we show how some additional structures were found by adding using smaller rotational increments.

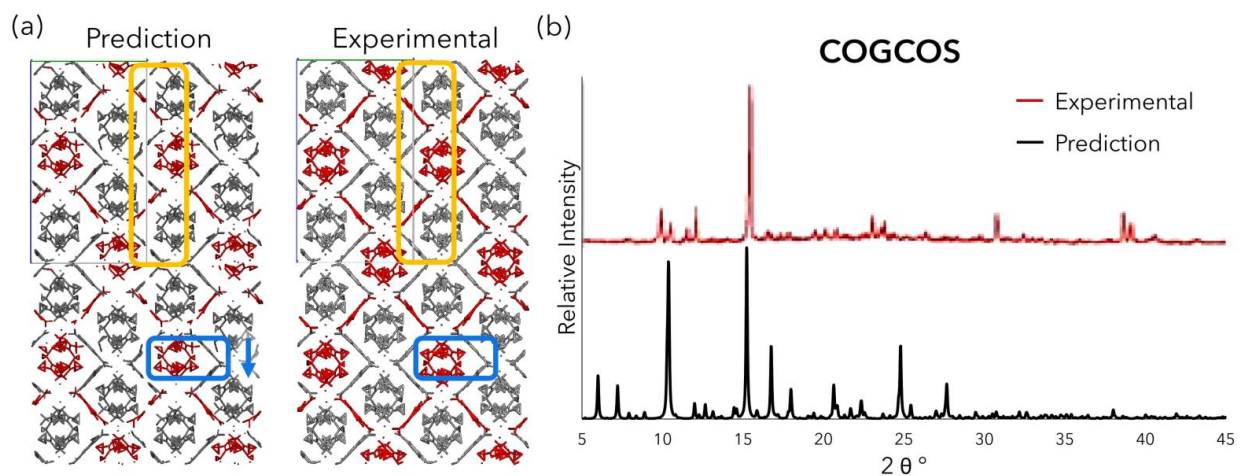


Appendix Figure 11 Candidate interpenetrating MOF pairs identified using 30-degree rotations. Same pairs are also present in the list provided by Kwon et al.¹⁸⁸ CCDC¹⁰⁴ reference codes for the MOF pairs are given below structures separated by an underscore. The first name corresponds the gray framework and second name corresponds to the red framework.

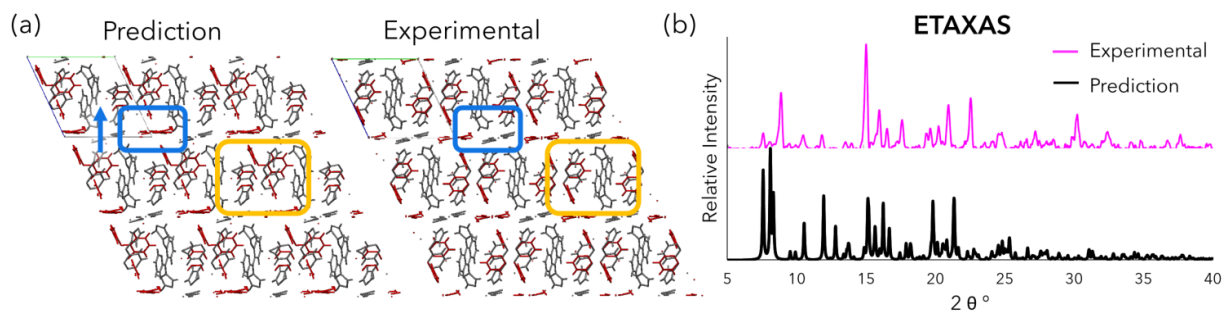
We performed interpenetration tests for three MOF pairs from the list by Kwon et al. and we obtained interpenetrated structures for [HABRAF_NIBJAK], [HEXVEM_VEBHUG], and [ADATEG_BAZGAM] using 30-degree rotations (see Appendix Figure 11). These MOF pairs were not identified in the original screening since they have trigonal unit cells where the interpenetrated configuration cannot be obtained using 90-degree rotations without orthogonalizing the unit cells.

Comparison of Experimental Hetero-Interpenetrated Structures. In addition to WEBZEK¹⁸⁹ provided in the article, hetero-interpenetration test was performed for 5 more MOFs using the algorithm. The crystal structure files were downloaded from the CCDC¹⁰⁴ database and the interpenetrating frameworks were separated. Then for each MOF the algorithm was ran using interpenetrating layers and resulting structures with lowest energy density were selected. Using the cif files provided by the algorithm X-ray diffraction (XRD) patterns were generated using Mercury¹⁹⁰ software. Moreover, the experimental XRD patterns were gathered from each study

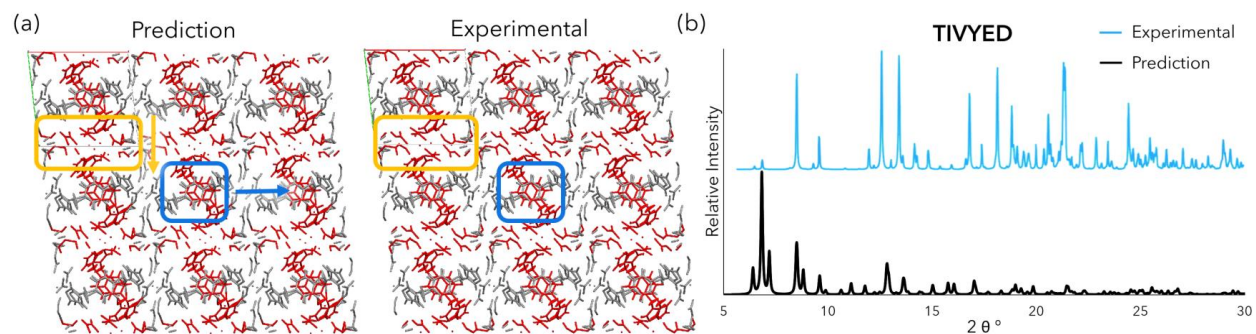
and results were compared. Both XRD patterns and visual inspection confirmed the high similarity between predicted and experimental structure. Here unit cell images and XRD patterns for these 5 MOFs are provided (Appendix Figures 12 - 16). In each figure, the XRD pattern with black line at the bottom is for prediction and the other color at the top is for experimental result. The yellow and blue boxes point out the subtle differences between structures and arrows show the directional difference. The interpenetrating frameworks are colored in gray and red for visual aid.



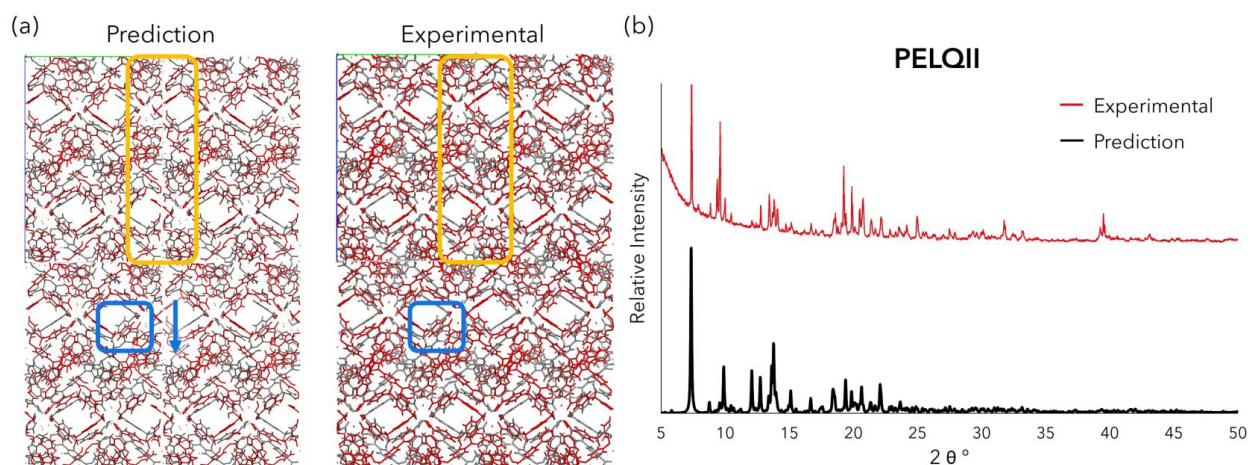
Appendix Figure 12 Hetero-interpenetration test for COGCOS⁶⁷ (a) Structure comparison (b) XRD pattern comparison



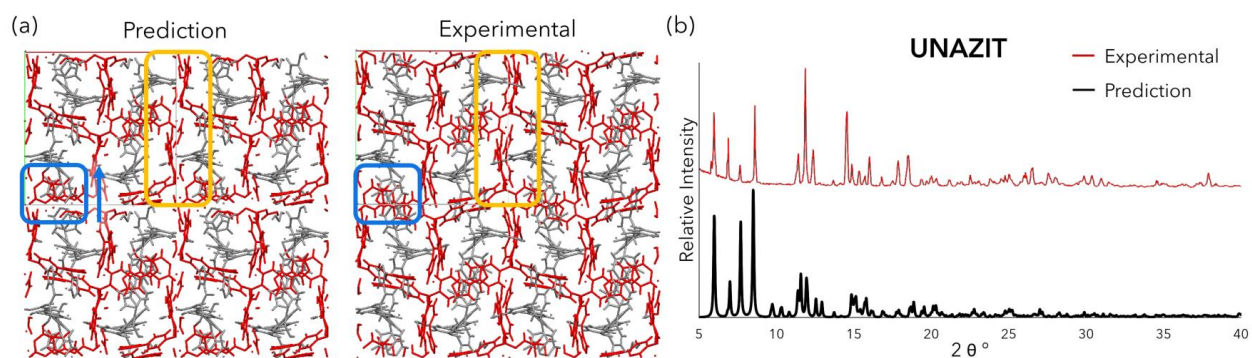
Appendix Figure 13 Hetero-interpenetration test for ETAXAS⁷² (a) Structure comparison (b) XRD pattern comparison



Appendix Figure 14 Hetero-interpenetration test for TIVYED⁷⁴ (a) Structure comparison (b) XRD pattern comparison



Appendix Figure 15 Hetero-interpenetration test for PELQII⁶⁸ (a) Structure comparison (b) XRD pattern comparison



Appendix Figure 16 Hetero-interpenetration test for UNAZIT⁷¹ (a) Structure comparison (b) XRD pattern comparison

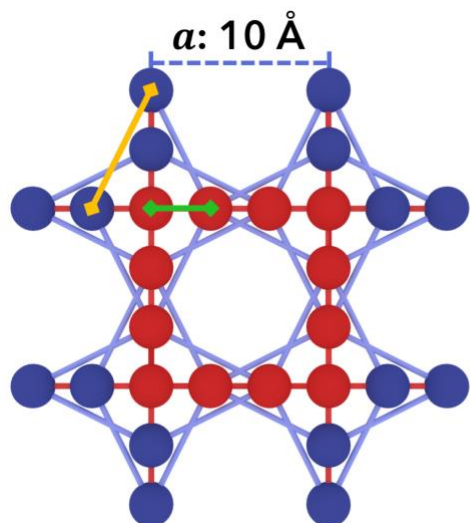
Appendix B Computational Methods and Supplementary Results for Thermal Conductivity of MOFs

Appendix B.1 Thermal Transport in Interpenetrated MOFs

Idealized Structure Generation. The ideal MOF structure is designed to have a cubic unit cell with a lattice constant of 10 Å consisting of 4 atoms in each side 3.3 Å apart from each other (see Appendix Figure 17). As evident from the inter-atomic distances, each atom site is modeled as a cluster of atoms with the mass of Ar (39.95 Da). The ideal MOF structure is inspired by IRMOF-1.

The interpenetrated structure is generated by creating a copy of the idealized structure and translating it 5 Å in each dimension which corresponds to maximal distance between frameworks. For each simulation, this initial configuration was used with a cubic simulation box of 80 Å containing 3584 and 7168 atoms for the single and interpenetrated structures, respectively.

Force Field Parameters for the Idealized Structure. The bonded interactions for idealized MOFs were modeled using Morse potential (see Appendix Figure 17). The equilibrium distances (r_0) were calculated according to the lattice constant (10 Å). For interpenetrated structures same potential parameters were used for individual frameworks. These parameters were chosen such that the structure would be stable and it would have a thermal conductivity of the same order as the typical MOFs (~0.8 W/mK).



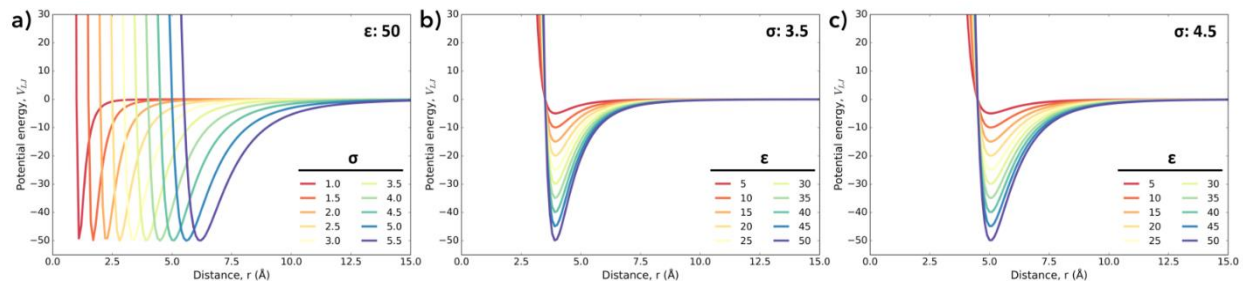
Morse Potential

$$U(r) = D[1 - e^{-\alpha(r-r_0)}]^2$$

Bond	$D \left(\frac{kcal}{mol} \right)$	$\alpha (\text{\AA}^{-1})$	$r_0 (\text{\AA})$
Short (green)	10	1.8	3.333 ($a/3$)
Long (yellow)	5	0.805	7.454 ($\sqrt{5}a/3$)

Appendix Figure 17 Bonded interactions for the idealized porous framework. Morse potential were used to model bonded interactions for the two types of bonds defined (depicted in green and yellow). The Morse potential parameters for these bonds are given.

The nonbonded interaction between interpenetrated frameworks were modeled using Lennard-Jones (LJ) potential (see Eq. 2-1) where epsilon (ϵ) is the depth of the potential well and sigma (σ) is the distance at which the interatomic potential is zero. The LJ potential energy function was plotted for varying σ and ϵ values in Appendix Figure 18. As seen in Appendix Figure 18a increasing σ shifts the potential well width and position. This effects the interpenetration by changing the optimal distance between frameworks. As seen in Appendix Figures 18b and 18c increasing ϵ values changes the depth of the potential well. This affects the likeliness of finding frameworks at the optimal distance at given time. At very low σ and ϵ the potential well almost disappears which causes interpenetrating frameworks to *slide* through each other. The interatomic distance in frameworks are 3.3 Å and for σ lower than approximately 1.5 Å the frameworks start to slide which artificially increases framework mobility.



Appendix Figure 18 Lennard-Jones potential for a) varying σ values and ϵ : 50 K.kB b) varying ϵ values for σ : 3.5 Å c) varying ϵ values for σ : 4.5 Å. In all plots the variable increases from red to blue as shown in legends.

Force Field Parameters for IRMOF-1. The force field parameters for IRMOF-1 was assigned from Universal Force Field (UFF)¹⁰¹ and the topology analysis was performed using the TherMOF Python package (see Appendix D). A periodic cubic simulation box ($a = 51.664$ Å) was used for each simulation using the same simulation procedure with idealized MOFs (see Section B2). The potentials used for IRMOF-1 simulations are provided in Appendix Table 3. Additionally, LAMMPS input files containing all force field parameters for both interpenetrated and non-interpenetrated IRMOF-1 are provided in the TherMOF GitHub repository.¹⁹¹

Molecular Dynamics Simulation Details. Equilibrium molecular dynamics simulations using LAMMPS¹²⁶ software package have been performed to calculate thermal conductivity. The thermal flux has been recorded in NVE ensemble for 1×10^6 timesteps after initialization in NVT (3×10^5) and NVE (3×10^5) ensembles, respectively. A time step of 1.0 fs was used for all idealized MOF simulations. Thermal conductivity was predicted using the Green-Kubo method which relates thermal conductivity to the instantaneous heat flux.^{192,193} For each idealized MOF structure, 10 simulations were run with different initial velocity distributions (using different seed numbers) and thermal flux was recorded in 3 directions (x, y, and z). The thermal conductivity was calculated for all 10 simulations and 3 directions separately and averaged for statistical sampling totaling 30

samples for each structure. For IRMOF-1, 5 individual simulations with different seed numbers were run with a time step of 0.5 fs and the same procedure as idealized MOFs. Recording the thermal flux in 3 directions (x, y, and z), thermal conductivity was calculated as an average of 15 samples for both interpenetrated and non-interpenetrated IRMOF-1. Example input files for LAMMPS simulations are provided in project GitHub repository.¹⁹¹

Appendix Table 3 Potential used for IRMOF-1 interactions

Interaction	Potential
Non-bonded	$E = 4\epsilon \left[\left(\frac{\sigma}{r} \right)^{12} - \left(\frac{\sigma}{r} \right)^6 \right] \quad r < r_c$
Bonded	$E = K(r - r_0)^2$
Angle	$E = K[C_0 + C_1 \cos(\theta) + C_2 \cos(2\theta)]$ $E = C [1 - B(-1)^n \cos(n\theta)]$
Dihedral	$E = K[1 + d \cos(n\phi)]$
Improper	$E = K[C_0 + C_1 \cos(\omega) + C_2 \cos(2\omega)]$

Framework Coupling on Thermal Conductivity. The thermal conductivity for an interpenetrated MOF can be estimated as the sum of the thermal conductivities of individual frameworks. However, at higher ϵ and moderate σ values it was observed that the thermal conductivity of the interpenetrating framework is lower than the sum of individual frameworks. As a result, a simple predictive equation is proposed which includes a coupling constant (γ) that describes the change of thermal conductivity with framework interaction:

$$k_{IP} = (k_1 + k_2)(1 - \gamma) \quad \mathbf{B-1}$$

where k_{IP} is the thermal conductivity of the interpenetrated framework and k_1 and k_2 are the thermal conductivities of the individual interpenetrating frameworks. The coupling constant, γ , is a function of σ and ε values used for approximating interframework interactions using Lennard Jones potential (see Eq. 2-1). We define the coupling constant as a product of the individual coupling constants of σ and ε as:

$$\gamma = \gamma_\sigma \gamma_\varepsilon \quad \mathbf{B-2}$$

For ε , a linear equation is formulated with the following boundary conditions:

$$\varepsilon_{min} < \varepsilon < \varepsilon_{max}$$

$$\varepsilon = \varepsilon_{min} \quad \rightarrow \quad \gamma_\varepsilon = 0$$

$$\varepsilon = \varepsilon_{max} \quad \rightarrow \quad \gamma_\varepsilon = \gamma_\varepsilon^{max}$$

where ε_{min} , ε_{max} and γ_ε^{max} are the lower and upper boundaries for ε coupling and the maximum contribution of ε to the overall coupling constant, respectively. In this study ε_{min} and ε_{max} were selected as the ε value of carbon atom in UFF (0.1 kcal/mol) and maximum ε used for interframework interactions (1.0 kcal/mol). Using the boundary conditions, the following step function is derived for γ_ε (see Appendix Figure 19a):

$$\gamma_{\varepsilon}(\varepsilon) = \begin{cases} 0 & \varepsilon < \varepsilon_C \\ \frac{\gamma_{\varepsilon}^{max}(\varepsilon - \varepsilon_C)}{\varepsilon_{max} - \varepsilon_C} & \varepsilon_C < \varepsilon < \varepsilon_{max} \\ 0 & \varepsilon > \varepsilon_{max} \end{cases} \quad \mathbf{B-3}$$

For σ , a quadratic equation was formulated with the following boundary conditions:

$$d_{min} < \sigma < d_{max}$$

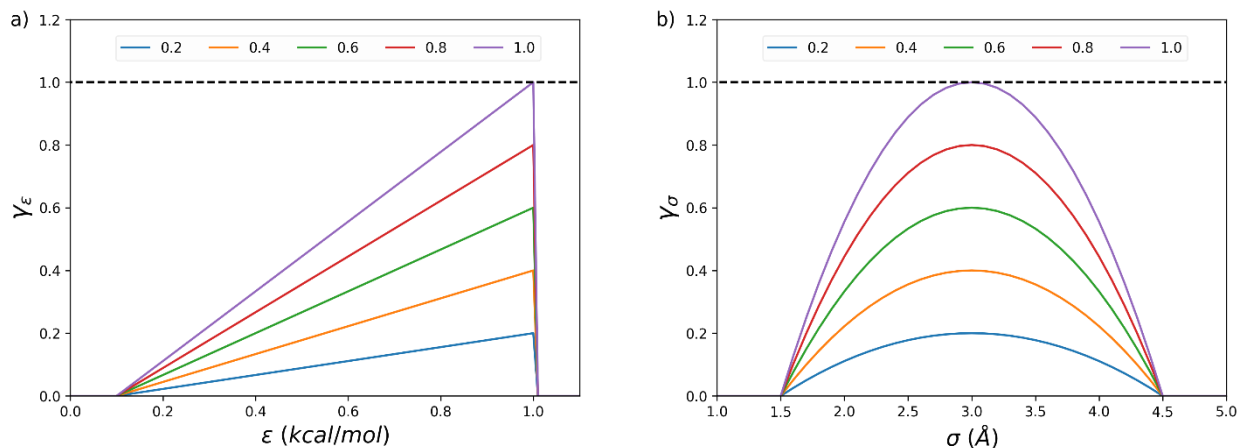
$$\sigma = d_{max} \quad \rightarrow \gamma_{\sigma} = 0$$

$$\sigma = d_{min} \quad \rightarrow \gamma_{\sigma} = -0$$

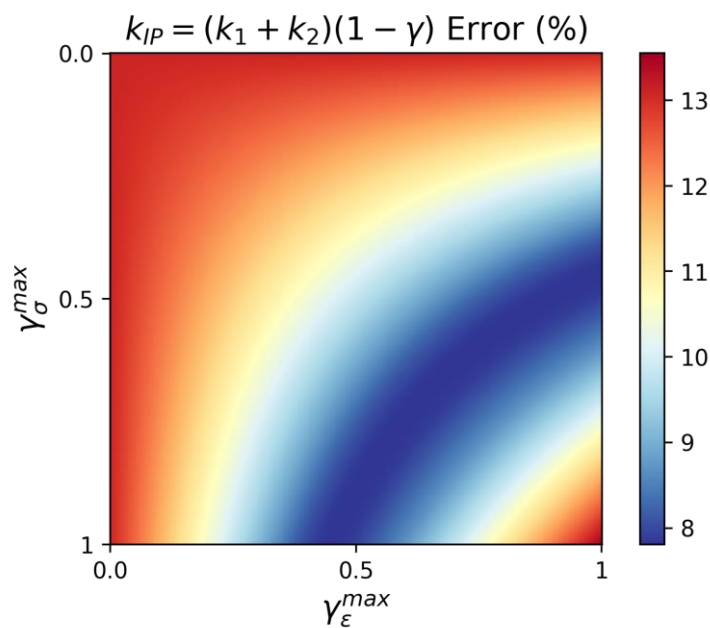
$$\sigma = \frac{d_{min} + d_{max}}{2} \quad \rightarrow \gamma_{\sigma} = \gamma_{\sigma}^{max}$$

where d_{min} , d_{max} , and γ_{σ}^{max} are the lower and upper boundaries for σ coupling and the maximum contribution of σ to the overall coupling constant, respectively. In this study d_{min} and d_{max} were selected as 1.5 and 4.5 Å, respectively. We observed that d_{min} corresponds well with the half of the minimum interatomic distance (3.33 Å) and d_{max} corresponds well with the half of the maximum interframework distance (8.67 Å). Using the boundary conditions, the following step function is derived for γ_{σ} (see Appendix Figure 19b):

$$\gamma_{\sigma}(\sigma) = \begin{cases} 0 & \sigma < d_{min} \\ \frac{4\gamma_{\sigma}^{max}}{2d_{min}d_{max} - d_{min}^2 - d_{max}^2}(\sigma - d_{min})(\sigma - d_{max}) & d_{min} < \sigma < d_{max} \\ 0 & \sigma > d_{max} \end{cases} \quad \mathbf{B-4}$$



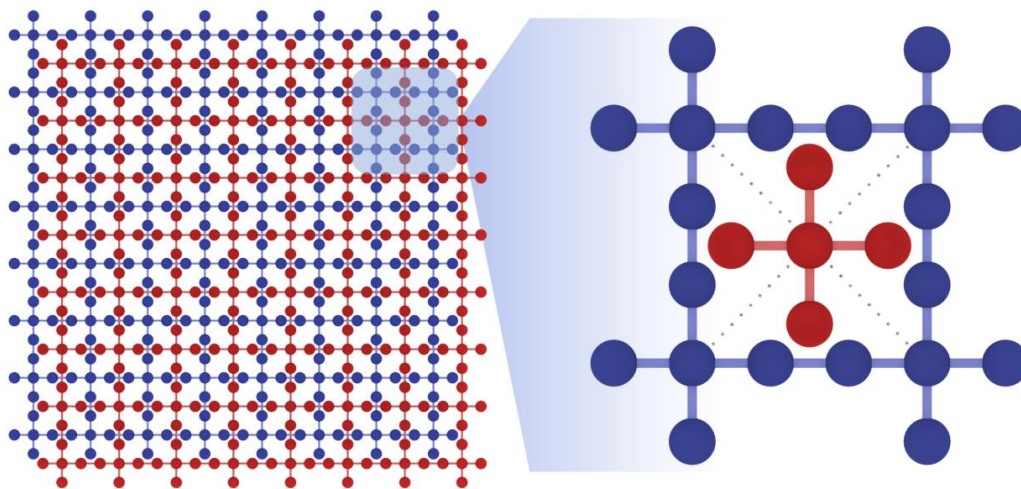
Appendix Figure 19 Coupling constant profile for different coupling constant limits. a) ϵ coupling constant (γ_ϵ) profile for changing limits (γ_ϵ^{\max}). b) σ coupling constant (γ_σ) profile for changing limits (γ_σ^{\max}).



Appendix Figure 20 Thermal conductivity prediction error (%) for interpenetrated framework using the relationship in Eq. B-1 for a range of σ (γ_σ^{\max}) and ϵ (γ_ϵ^{\max}) coupling constant limits. Minimum average error (7.8 %) was found for γ_σ^{\max} : 0.498 and γ_ϵ^{\max} : 0.889.

The maximum contributions of σ (γ_{σ}^{max}) and ε ($\gamma_{\varepsilon}^{max}$) to the coupling constant can be optimized by minimizing the average prediction error of Eq. B-1. The average error of Eq. B-1 for varying γ_{σ}^{max} and $\gamma_{\varepsilon}^{max}$ were calculated for all range of interframework interactions considered in this study (see Appendix Figure 20). The lowest average error was found to be 7.8% with $\gamma_{\sigma}^{max} = 0.498$ and $\gamma_{\varepsilon}^{max} = 0.889$.

Relative Distance Between Interpenetrating Frameworks. The relative distance of one corner atom of the second framework (Appendix Figure 21 shown in red) to the 8 corner atoms of the surrounding first framework (Appendix Figure 21 shown in blue) were calculated from MD trajectories. The calculation was done for a single unit cell selected from the center of the simulation box. Using this calculation, the relative position of interpenetrating frameworks were analyzed as shown in the manuscript.



Appendix Figure 21 Interpenetrated idealized MOF structure where entangled frameworks are colored in blue and red. The zoomed in single unit cell shows atoms used to calculate the relative distance between frameworks in 2D. In 3D the distance between the red atom in the middle and all 8 corner atoms, identical to a body centered cubic configuration, is calculated for each 1000 timesteps of MD trajectories.

Mean Squared Displacement. Mean squared displacement (MSD) was calculated by averaging the distance of a given atom to a reference position using the equation below:

$$\langle d_i^2 \rangle = \frac{1}{N} \sum_{t=1}^N d_i(t)^2 \quad \mathbf{B-5}$$

where $d_i(t)$ is the distance of atom i from its position at $t = 0$ and N is the number of timesteps.

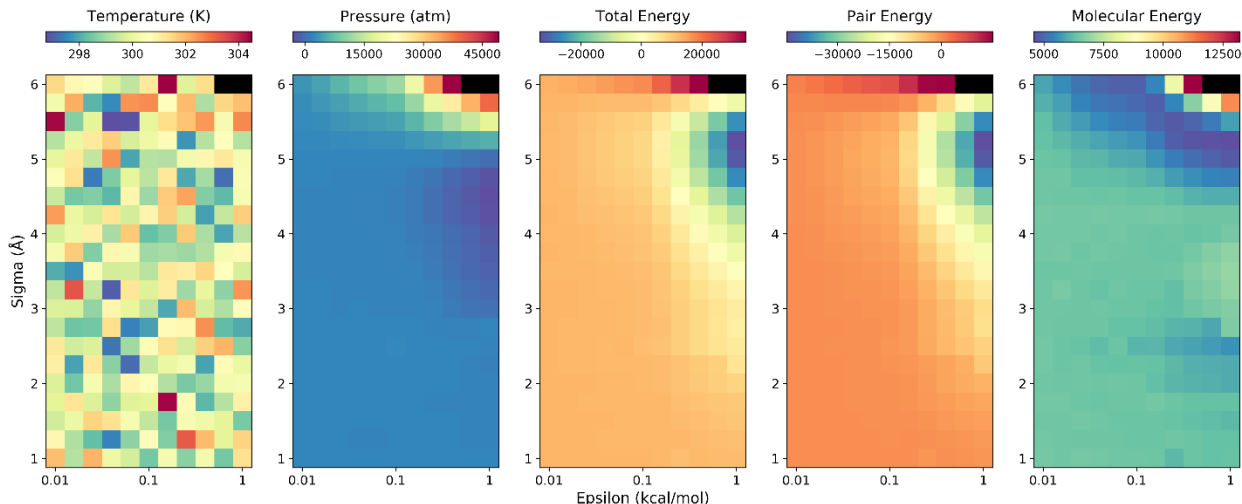
Consequently $d_i(t)$ is calculated as:

$$d_i(t) = \sqrt{[x_i(t) - x_i(0)]^2 + [y_i(t) - y_i(0)]^2 + [z_i(t) - z_i(0)]^2} \quad \mathbf{B-6}$$

The calculation was performed for the interpenetrating framework atoms separately to see whether the displacement is same for each framework. As expected, the MSD were almost identical for each simulation.

The MSD is calculated using the therMOF Python library for a wide range of force field parameters that describe framework interactions and reported in the manuscript. MSD was observed to increase towards low σ and ε values. This suggests that when the framework interactions are weaker and the distance between framework atoms are higher the framework mobility is increased.

Thermodynamics. Thermodynamic data including temperature, pressure, total energy, pair energy, and molecular energy were recorded for each simulation in each 1000 timesteps. Each bin in the histogram represents average of 10 runs of MD simulations with 2.3 million timesteps.



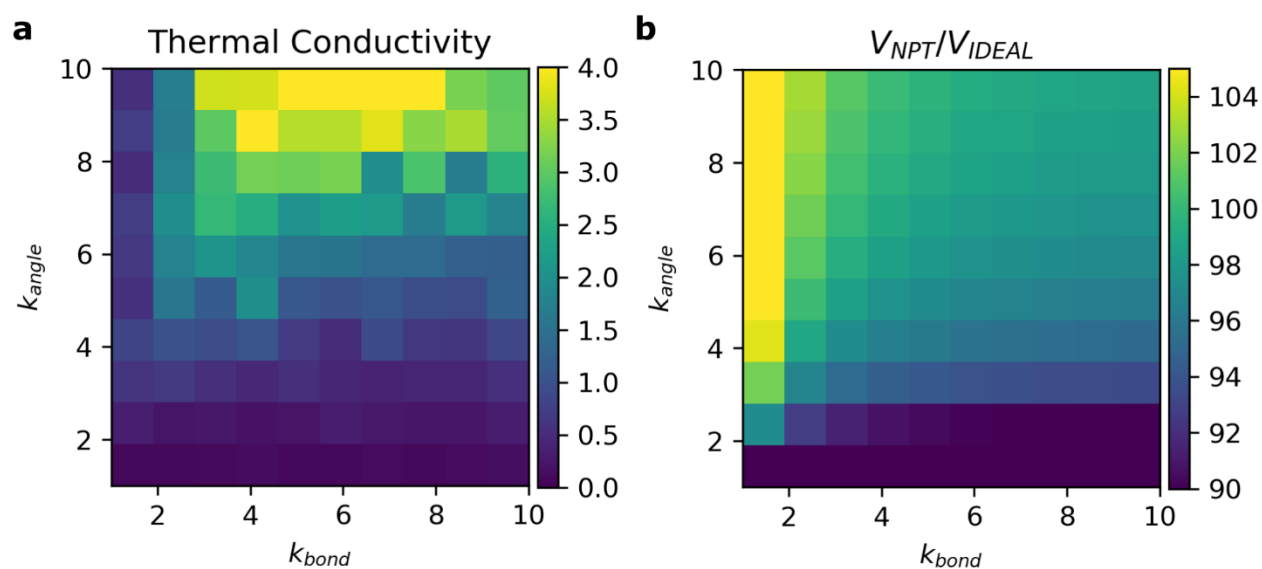
Appendix Figure 22 2D histograms for thermodynamic data recorded during framework interaction parametric screening. All energy in kcal/mol.

The temperature is randomly distributed among interaction parameters with no apparent trend. This suggests the system is properly relaxed in each simulation and temperature was kept mostly constant with approximately ± 3 °C deviation. The pressure is mostly similar among interaction parameters except for two regions corresponding to higher ϵ and σ values. The high-pressure region is observed for $\sigma > 5$ Å and $\epsilon > 0.1$ kcal/mol which have high repulsion forces. The low-pressure region is defined by $3 < \sigma < 5$ Å and $0.2 < \epsilon < 1.0$ kcal/mol. The total energy is defined as the sum of molecular energy and pair energy. As seen in Appendix Figure 22 the pair energy dominates the total energy and both show similar trends with pressure.

Appendix B.2 Thermal Transport in Flexible MOFs

The atomic positions for the idealized MOFs were adapted from the idealized cubic MOF model mentioned in Appendix B1. In order to model framework breathing we define two-body

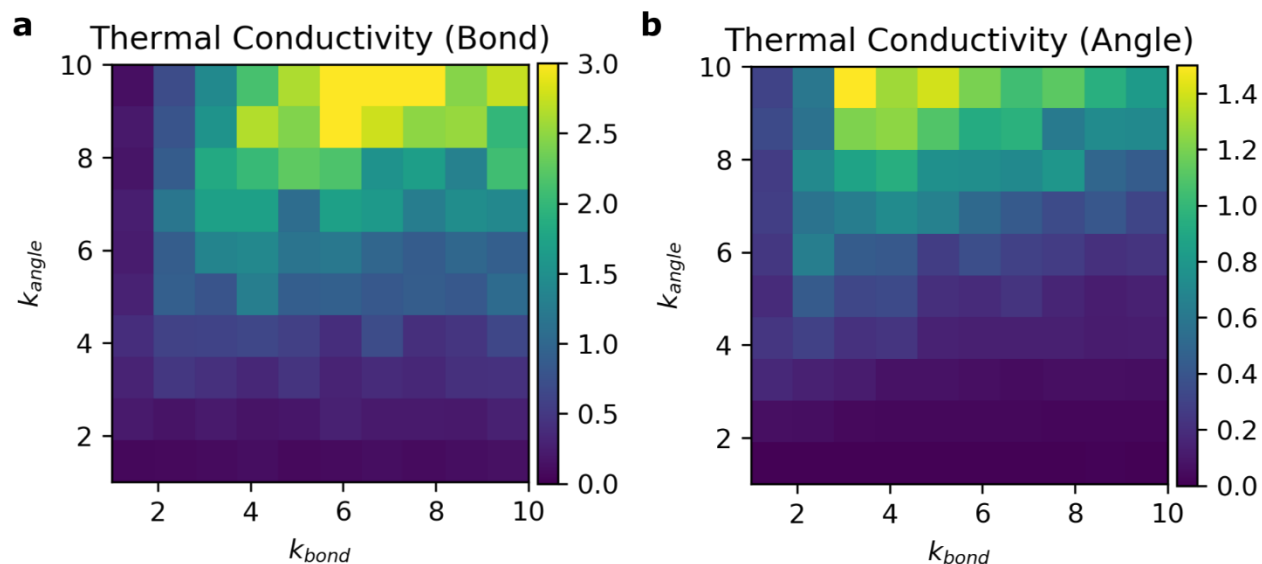
bonded and three-body angular interactions between atoms, which are modeled using harmonic potentials (see Figure 14). To determine meaningful spring constants for the potentials we screened spring constants between 1 - 10 kcal/mol for the 90° structure with increments of 1 kcal/mol for both two-body bonded and three-body angular harmonic potentials (see Appendix Figure 23). As seen in Appendix Figure 23a the thermal conductivity increases at higher spring constants, especially for angular potential. For bonded potential, this increase seems to be maximized around 6 kcal/mol and then levels off with further increase.



Appendix Figure 23 2D histograms for change in (a) thermal conductivity (W/mK) and (b) simulated box volume to idealized box volume ratio (%) as a function of spring constants for two-body bonded and three-body angular harmonic potentials.

As the idealized structure is relaxed during the MD simulation in the NPT ensemble the simulation box size is changed compared to the initial configuration. This change is influenced by the spring constants used for the bonded and angle potentials as they determine the final geometry of the structure. Here we calculated the average box size during the NPT ensemble and plotted is

as a function of spring constant for two-body bonded and three-body angular harmonic potentials. As seen in Appendix Figure 23b the simulation box size increases compared to initial (ideal) box size at higher angular spring constants and lower bonded spring constants. Overall, the simulated box size is relatively close to the ideal box size.

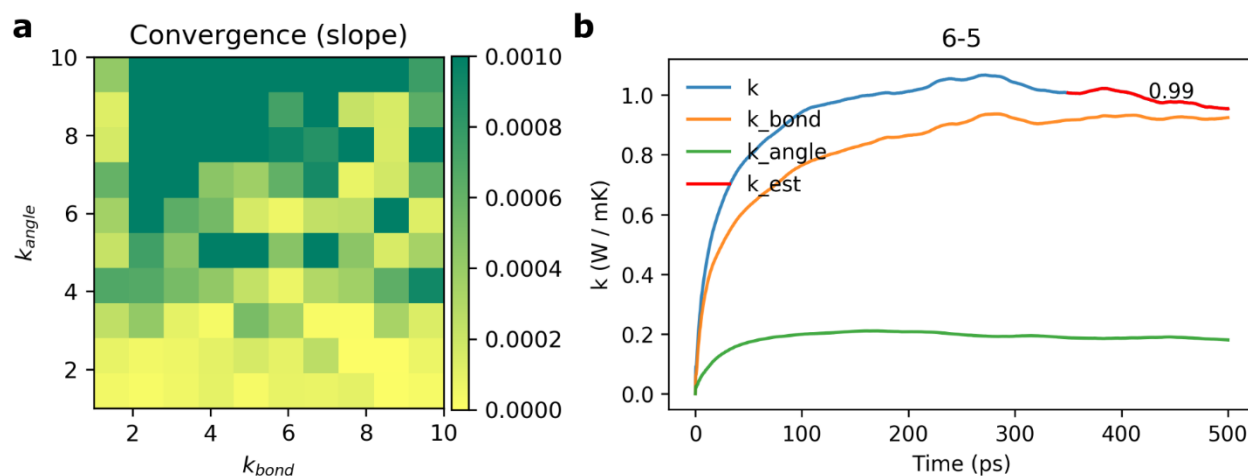


Appendix Figure 24 2D histograms for change in thermal conductivity (W/mK) due to (a) bonds and (b) angles as a function of spring constants for two-body bonded (x-axis) and three-body angular (y-axis) harmonic potentials.

Furthermore, we isolated the contribution of bonded and angular harmonic potentials to thermal conductivity and investigated the effect of spring constants of these potentials to thermal conductivity. As seen in Appendix Figure 24, bonded potentials contribute considerably more to the overall thermal conductivity compared to angle potentials. Overall, the thermal conductivity shows similar behavior for both of these potentials as observed in Appendix Figure 23.

As we investigated the heat current autocorrelation functions we realized not all these spring constants were resulting in converged simulations to estimate accurate thermal conductivities. As

seen in Appendix Figure 25b the average thermal conductivity change during the simulation time needs to flatten in order to estimate the overall thermal conductivity accurately. To check for that we calculated the absolute slope of a linear fit to the last 150 ps of the autocorrelation window (see the red line in Appendix Figure 25b) of all averaged thermal conductivity vs time curves for all the spring constants considered. As this slope gets closer to zero it means that the fit region gets flatter which is an indication of thermal conductivity convergence. In Appendix Figure 25a, the slope of these fits (i.e. convergence) is given as a function of spring constants for bonded and angular potentials. As the spring constant for both bonded and angular potentials increase, the convergence seems to get worse.



Appendix Figure 25 (a) 2D histogram for the thermal conductivity convergence as a function of spring constants for two-body bonded (x-axis) and three-body angular (y-axis) harmonic potentials. (b) Average thermal conductivity vs simulation time for the idealized structure with a bonded potential spring constant of 6 kcal/mol and angular potential spring constant of 5 kcal/mol. “ k ” stands for overall thermal conductivity, “ k_{bond} ” and “ k_{angle} ” are the contributions of bonded and angular potentials to the thermal conductivity, respectively. “ k_{est} ” is the estimated thermal conductivity (0.99 kcal/mol) calculated by averaging the last 150 ps of the time dependent thermal conductivity curve.

With further investigation the spring constant for the bonded potential was selected as 6 kcal/mol and the spring constant for the angular potential was selected as 5 kcal/mol. These parameters were selected by considering the proximity of the estimated thermal conductivity to 1 W/mK, the proximity of the simulated box volume to ideal box volume and finally the thermal conductivity convergence. Overall, the aforementioned parameter set gave the best results.

Adding Adsorbate Molecules to Idealized Structures. The idealized structures were populated with single site adsorbates at a density of 5 molecules/nm³ using Packmol software.¹⁹⁴ All the gas molecules were randomly distributed in the simulation box making sure none of them overlapped with the framework atoms or each other. A 5 Å tolerance was used to make sure molecules were not added to the edges of the box and all gas molecules were placed at least 4 Å apart from each other and the framework atoms. For each tilt angle considered, same initial positions of gas molecules were used with different initial velocities. Total number of atoms in the simulation box and the number of adsorbate atoms for each tilt angle is in Appendix Table 4.

Appendix Table 4 Total number of atoms and total number of adsorbate molecules for simulation setups with different tilt angles

Tilt angle (°)	Total # atoms	# Adsorbates
40	5229	1645
50	5545	1961
60	5801	2217
70	5989	2405
80	6105	2521
90	6144	2560

The nonbonded interaction for the gas molecules were modeled using a Lennard-Jones potential with mixed force field parameters given in Appendix Table 5.

Appendix Table 5 Force field parameters for a Lennard-Jones potential modeling vdW interactions of gas molecules

Interaction	Epsilon (kcal/mol)	Sigma (Å)
MOF – Gas	0.429	3.73
Gas – Gas	0.294	3.73

Appendix C Calculating Surface Diffusion of Large Molecules

Appendix C.1 Force Field Parameters

All molecules were assumed to be rigid and the Cu (110) surface atom positions were fixed during all simulations (including both MD and TST). Only vdW interactions between the molecule and surface were considered using a Lennard-Jones potential with a cut-off radius of 12.5 Å as implemented in LAMMPS¹²⁶ software package. The force field parameters were adopted from Universal Force Field (UFF)¹⁰¹ and Lorenz-Berthelot mixing rules were applied. For classical MD simulations the parameters were used without change, however, for TST simulations all mixed parameters were scaled by 10 (see Appendix Table 6 below for all parameters used).

Appendix Table 6 Simulation parameters used in this study to calculate vdW energy using a Lennard-Jones potential. All parameters are for pairs of atoms where the epsilon values are in kcal/mol and sigma values are

in Å.

Element Pair	MD		TST	
	Epsilon (kcal/mol)	Sigma (Å)	Epsilon (kcal/mol)	Sigma (Å)
Cu - B	0.15	3.376	1.5	3.376
Cu - C	0.115	3.272	1.15	3.272
Cu - H	0.074	2.842	0.74	2.842
Cu - N	0.093	3.187	0.93	3.187
Cu - O	0.087	3.116	0.87	3.116

Appendix C.2 Calculating Diffusion Coefficient from Rigid Body Molecular Dynamics Simulations

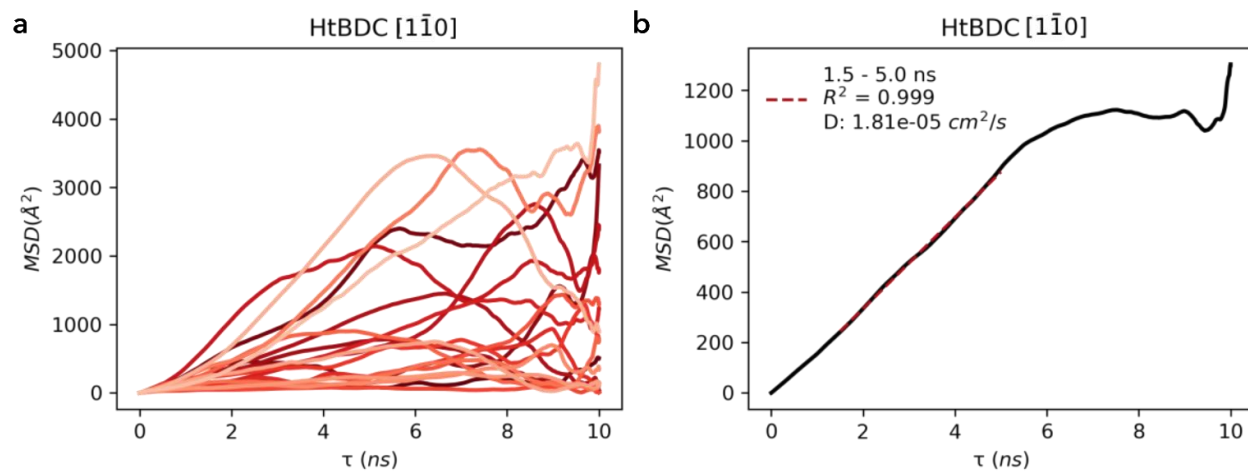
For each molecule, the center of mass was calculated at every 1 ps and was used to calculate mean squared displacement (MSD) to estimate diffusion coefficient. The MSD is calculated using the relation below:

$$MSD = \langle (x - x_0)^2 \rangle = \frac{1}{N} \sum_i^N [x_n(t) - x_n(0)]^2 \quad \text{C-1}$$

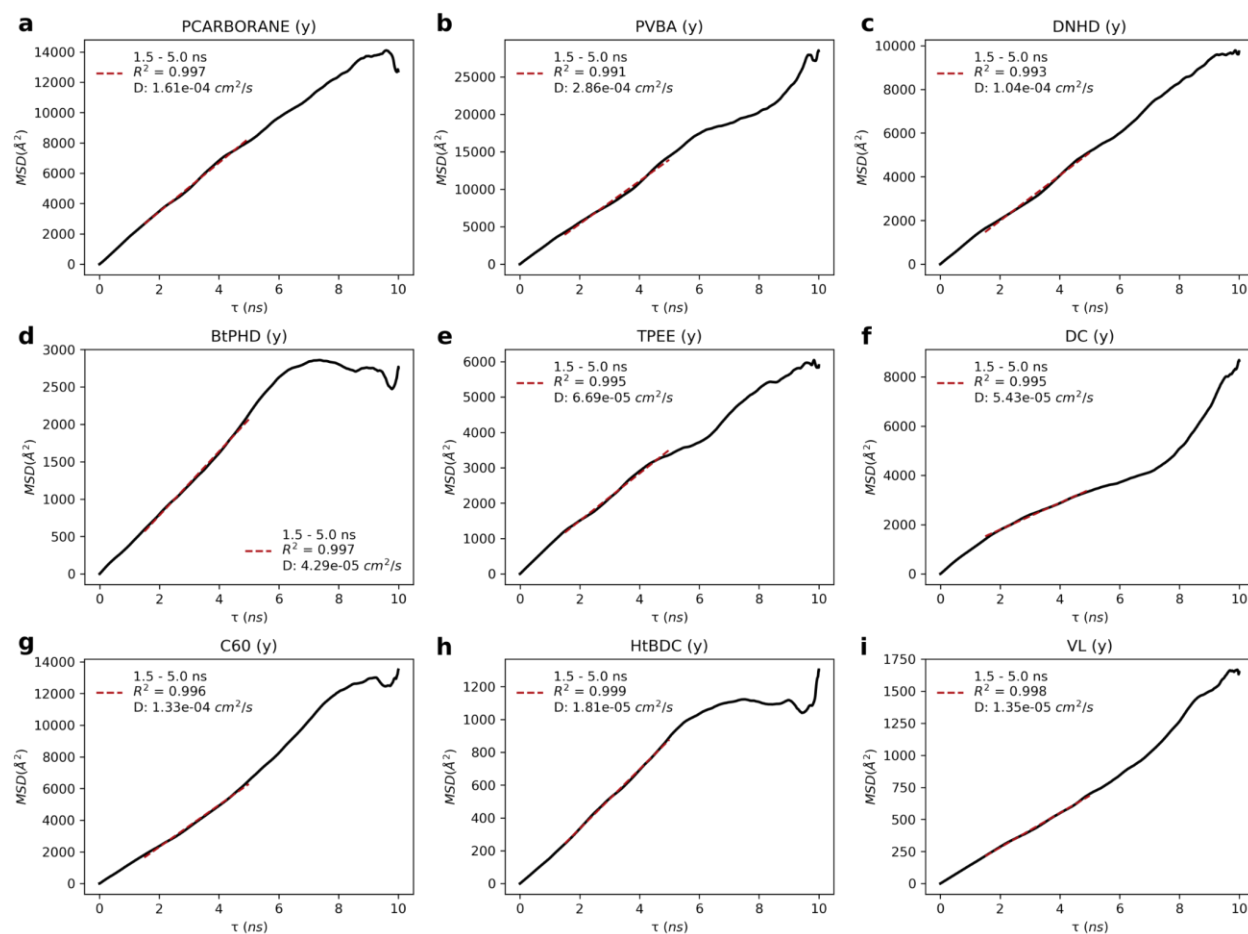
where N is the number of particles to be averaged (in our case since there is only one molecule N becomes 1), $x_n(0)$ is the reference position, and $x_n(t)$ is the position at time t . Calculating MSD with respect to different reference times, we can plot MSD vs τ (Appendix Fig 26a). Repeating this for multiple runs to improve sampling we can then get an average MSD vs τ and using Einstein's relation we can calculate self-diffusion coefficient using the relation below:

$$MSD = (2nD)\tau + b \quad \text{C-2}$$

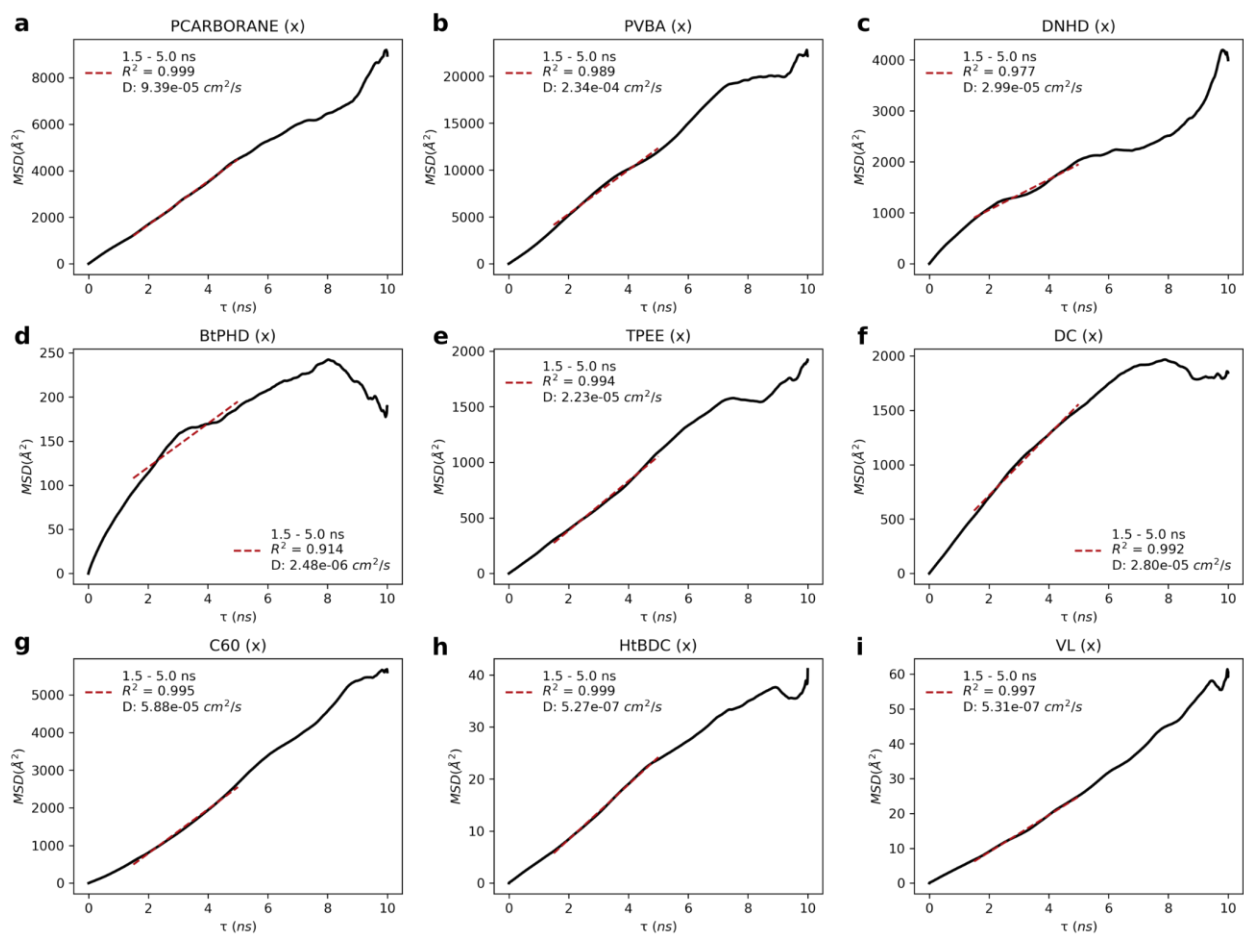
where n is the dimensionality of motion, D is the self-diffusion coefficient, τ is the time delta, and b is the constant to the linear fit (see Appendix Figure 26b).



Appendix Figure 26 (a) Mean squared displacement (MSD) vs time delta (τ) for 20 molecular dynamics simulations in $[1\bar{1}0]$ direction for HtBDC molecule. (b) Average of all MSD vs τ curves and a linear fit between 1.5 ns – 5.0 ns to calculate self-diffusion coefficient. The R-squared value for the fit as well as the diffusion coefficient are given in the legend.



Appendix Figure 27 (a) Averaged mean squared displacement (MSD) vs time delta (τ) for 20 molecular dynamics simulations in $[1\bar{1}0]$ direction. A linear fit between 1.5 ns – 5.0 ns was used to calculate self-diffusion coefficient. The R-squared value for the fit as well as the diffusion coefficients are given in the legend and the molecule names are given in the title.



Appendix Figure 28 (a) Averaged mean squared displacement (MSD) vs time delta (τ) for 20 molecular dynamics simulations in [001] direction. A linear fit between 1.5 ns – 5.0 ns was used to calculate self-diffusion coefficient. The R-squared value for the fit as well as the diffusion coefficients are given in the legend and the molecule names are given in the title.

Appendix C.3 Transition State Theory

As the diffusion of large molecules are quite slow and time scales cannot be achieved with classical MD simulations, we further increased adsorption energy by increasing LJ epsilon parameter of the surface atom and employed umbrella sampling and weighted histogram analysis method (WHAM)¹⁷⁶ to calculate free energy barriers for diffusion. We developed a Python wrapper for the WHAM implementation by Grossfield et al.¹⁹⁵ for this study which is freely available on GitHub.¹⁹⁶

For the umbrella sampling, we divided the orthogonal unit cell of a Cu (110) surface (3.597 x 2.543 Å) using 0.1 Å grid spacing with two additional grid points on the edges of the cell resulting in 29 points in $[1\bar{1}0]$ and 39 points in $[001]$ directions (1131 total). For each point on the surface, we placed the molecule at that point and constrained its motion in $[1\bar{1}0]$ and $[001]$ directions in separate simulations using a spring with a constant of 200 kcal/mol. The motion in the direction perpendicular to the surface was not constrained.

For a given direction, periodic free energy barriers were calculated for each parallel pathway. For $[1\bar{1}0]$ direction 39 parallel paths were considered with 29 points in each path. For each of these paths the transition state energy was estimated and for a given direction overall transition state energy was calculated using a Boltzmann average.

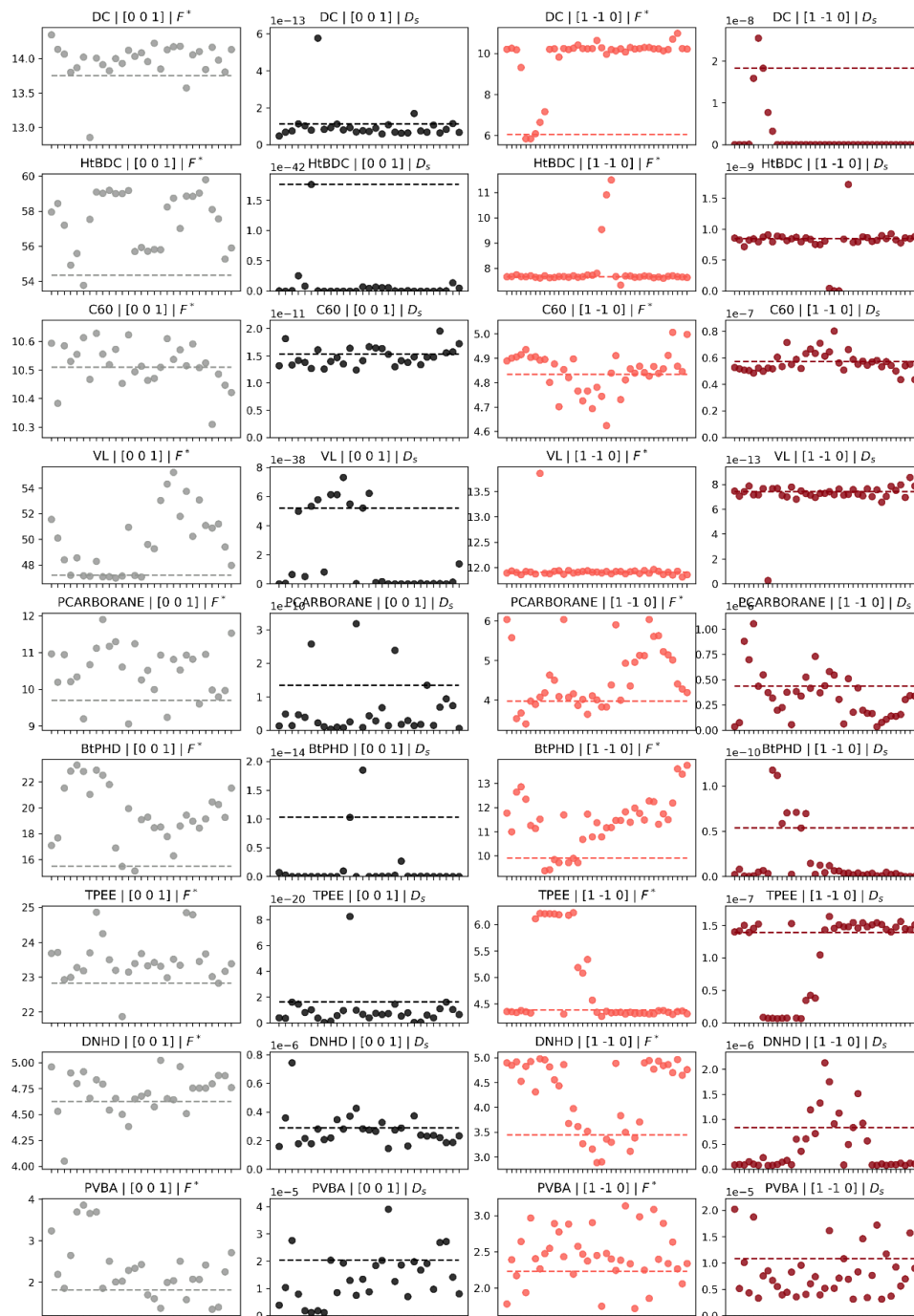
Using one dimensional transition state theory, hopping rate between these points were calculated using the equation below:

$$k_{A \rightarrow B} = \kappa \sqrt{\frac{k_B T}{2\pi M}} \times \frac{e^{-\beta F(q^*)}}{\int e^{-\beta F(q)} dq} \quad \text{C-3}$$

where $k_{A \rightarrow B}$ is hopping rate from state A to B, κ is transmission coefficient, k_B is Boltzmann constant, T is temperature, M is mass of the molecule, $F(q)$ is free energy at position q where q^* denotes the transition state position and $\beta = 1/k_B T$.¹⁸² In this study the transmission coefficient κ was assumed to be 1. After calculating hopping rate, self-diffusion coefficient can be estimated using the relation below:

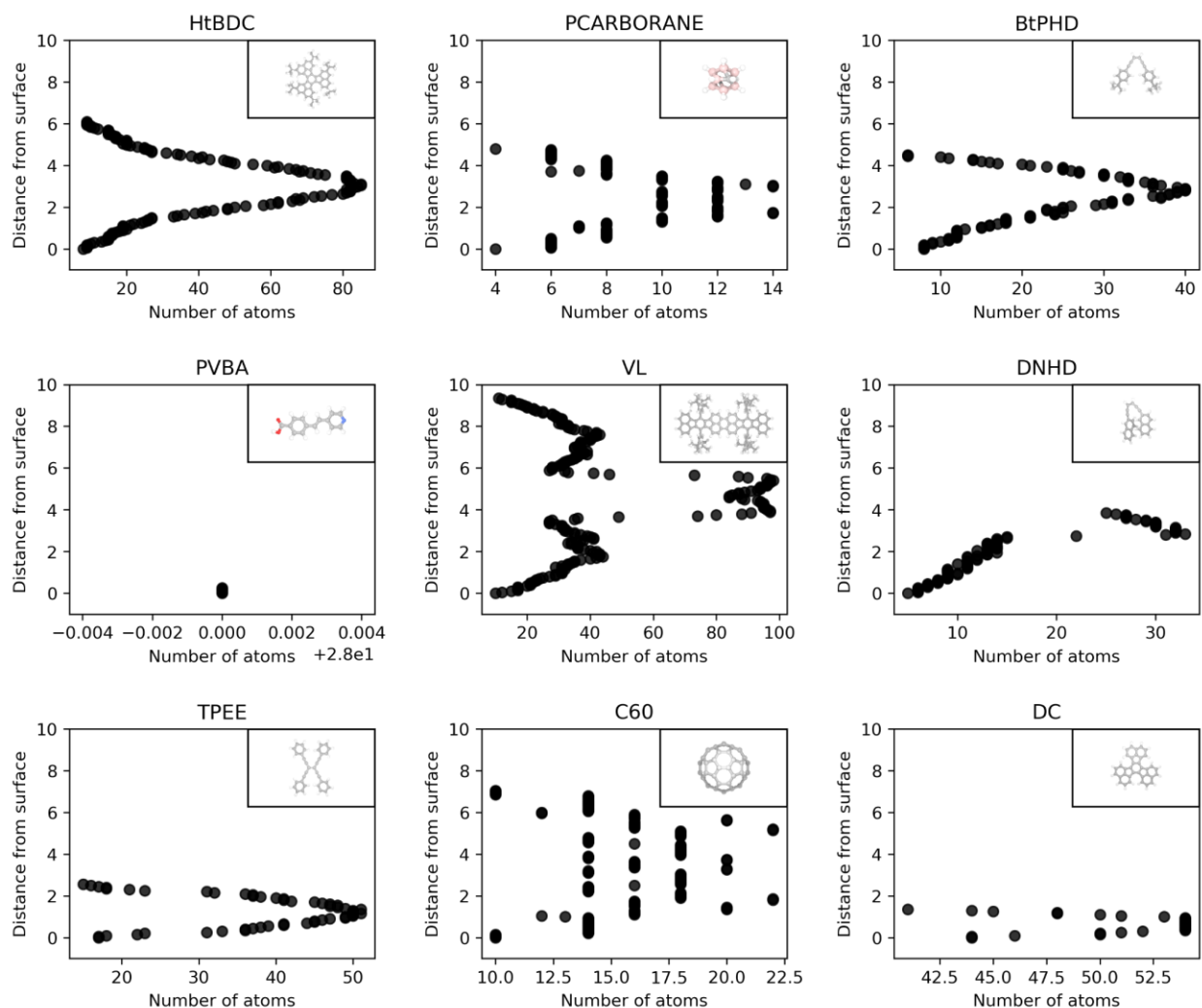
$$D_S = \frac{1}{2n} \times k_{A \rightarrow B} \times \lambda^2 \quad \mathbf{C-4}$$

where n is dimensionality and λ is hopping length. As diffusion coefficient was calculated separately for each direction, dimensionality was taken as 1.



Appendix Figure 29 Free energy barriers and self-diffusion coefficients for each molecule and each umbrella sampling paths for the two primary crystallographic directions. Red and blue points correspond to results for $[001]$, and $[1\bar{1}0]$ directions, respectively. The dashed line represents the Boltzmann averaged value for the overall diffusion in that direction. The molecule name, crystallographic direction and variable names are given in the title.

Appendix C.4 Elevation Weighted Density



Appendix Figure 30 Elevation weighted density curves for the nine molecules used in this study

As discussed in Section 4.1, we calculated elevation weighted density for each molecule according to their orientation with respect to the surface. This calculation was done by counting the number of atoms within a selected cut off-distance (1 \AA) as we discretely move up from the surface (with a step size of 0.05 \AA) until we reach a distance of 12 \AA . The resulting distance vs number of atoms graphs are plotted for each molecule in Appendix Figure 30 below.

In order to calculate a scalar value from the curves in Appendix Figure 30, each point from $z=0$ to $z=12$ was scaled exponentially to reach zero at $z=12$, where z is the elevation in Å. An exponential decay equation was used for the scaling and the constants were chosen to make sure the scaling reaches to zero at the cut-off radius. The elevation weighted density equation form is given below:

$$\sum_{z=0}^{r_c} N_z [a(1-b)^z] \quad \text{C-5}$$

where r_c is the cut-off radius taken as 12 Å, N_z is the number of atoms for a given elevation z , a , and b are the constants of the exponential decay equation which were taken as 0.376 and 0.4, respectively.

Appendix D Software Packages Developed

In this section, we highlight the software development efforts for this dissertation. Numerous packages were developed and made available with open source licenses on GitHub. When developing these packages, we made sure to use best software practices as much as possible. These include creating proper documentation, employing unit tests, using continuous integration and version control. Here we list some of the more developed packages and briefly explain their functionality.

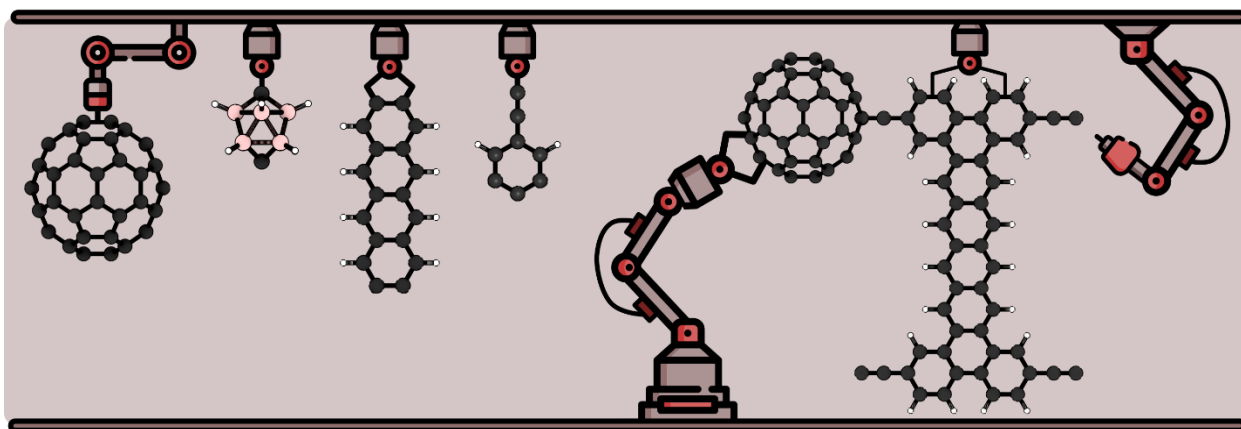
Appendix D.1 Ångström: a Python Package for Molecular Architecture and Visualization



Ångström is a Python package for geometric molecular operations, molecular visualization and animations. The purpose of Ångström is to be a lightweight and easily integrable package. This way it can be easily included in various simulation packages. Ångström offers high quality molecular visualization from the command-line. It provides easy integration with visualization software such as Blender, OpenBabel, VMD for producing images and animations as well nglview

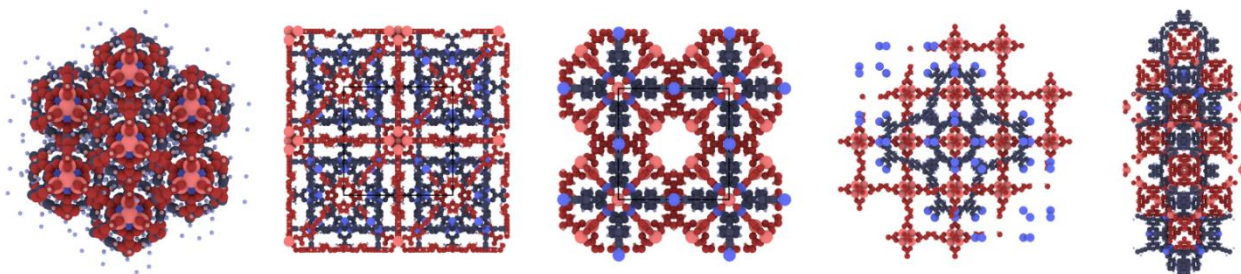
Python packages for visualization in Jupyter notebooks. Ångström is available from:
<https://github.com/kbsezginel/angstrom>.

Appendix D.2 Nanocar Builder Avogadro Plug-in



As discussed in Section 4.2 nanocar builder is a plug-in for Avogadro 2 molecular visualization software. Using this plug-in, nanocar molecules can be assembled from a collection of chassis and wheel molecular components. Metal slabs with arbitrary size and geometry can be built and the nanocar can be placed on a metal surface. Finally, a LAMMPS¹⁵⁸ Molecular Dynamics configuration file can be exported to study diffusion of the nanocar on metal surfaces. Detailed installation and usage instructions (including a video tutorial) are provided on the GitHub page:
<https://github.com/kbsezginel/nanocar-avogadro>.

Appendix D.3 IPMOF: a Python Package for Discovering Interpenetrated MOFs



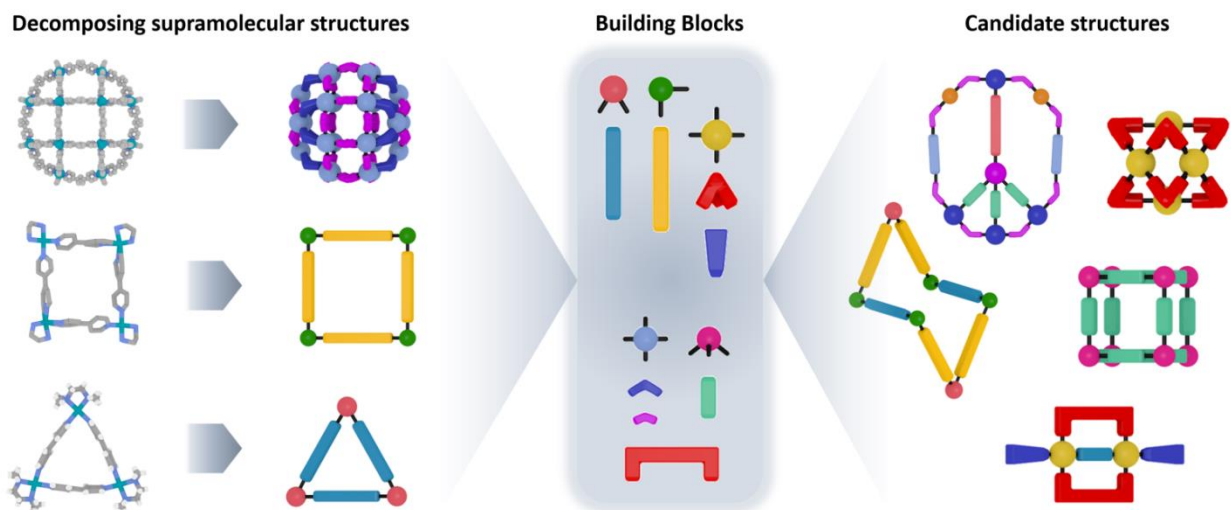
As introduced in Section 2, IPMOF tests whether two given MOFs can interpenetrate each other by rapidly trying different relative orientations of the two frameworks and reports the plausibly energetically favorable ones. The algorithm tries many different orientations of two given MOFs by performing rotation and translation operations according to user configurable parameters. After an orientation is chosen, its energetic favorability is calculated based on the pairwise interactions between each atom on one framework with every atom on the other framework. Overall, IPMOF can rapidly detect cases where interpenetration is impossible, and suggest ones where it may be plausible. Detailed installation and usage instructions and the software are available from: <https://github.com/kbsezginel/IPMOF>.

Appendix D.4 TherMOF: a Python Package for Investigating Thermal Transport in MOFs

TherMOF library can be used to initialize, run, and analyze simulation results to investigate thermal transport in porous crystals. This package was used in Section 3 to investigate thermal conductivity of interpenetrating and flexible MOFs. Detailed installation and usage instructions,

representative simulation setup files and the software are available from:
<https://github.com/kbsezginel/thermof>.

Appendix D.5 Moleidoscope (Molecular Kaleidoscope)



A key challenge in chemistry is to design molecules with given shapes and sizes comprising many components. One approach to designing structures with such a large number of components is to leverage the typically highly symmetrical nature of supramolecular structures. “Moleidoscope” interactively applies point group symmetry operations to generate hypothetical supramolecular structures in silico. Starting with a simple organic compound, the molecule is replicated using mirror operations, and by selecting multiple mirrors (3D planes), prisms can be

formed to have multiple copies of the molecule oriented symmetrically. Moreover, as is the case with kaleidoscope, by rotating these mirrors even more copies can be obtained with many different symmetries. Software and installation instructions are available from: <https://github.com/kbsezginel/Moleidoscope>.

Appendix D.6 Tutorials for Computational Chemistry Tools and Scientific Visualization

In addition to software packages highlighted here, tutorials for using other computational chemistry tools and scientific visualization have been put together. These include Python scripts for chemical file conversion and manipulation, tutorials for writing Avogadro plug-ins, and tutorials for using RASPA, LAMMPS, OpenBabel, EQeq, Packmol, and HostDesigner. These are available from: <https://github.com/kbsezginel/chem-tools-tutorials>. Furthermore, additional tutorials and examples for using matplotlib Python plotting library and different molecular visualization tools are available from: <https://github.com/kbsezginel/visualization>.

Bibliography

1. Browne, W. R. & Feringa, B. L. Making molecular machines work. *Nat Nano* **1**, 25–35 (2006).
2. Eelkema, R. *et al.* Molecular machines: Nanomotor rotates microscale objects. *Nature* **440**, 163–163 (2006).
3. Juluri, B. K. *et al.* A Mechanical Actuator Driven Electrochemically by Artificial Molecular Muscles. *ACS Nano* **3**, 291–300 (2009).
4. Collier, C. P. *et al.* Electronically Configurable Molecular-Based Logic Gates. *Science* **285**, 391–394 (1999).
5. Van Noorden, R. & Castelvechi, D. World's tiniest machines win chemistry Nobel. *Nature News* **538**, 152 (2016).
6. Zhang, Q. & Qu, D.-H. Artificial Molecular Machine Immobilized Surfaces: A New Platform to Construct Functional Materials. *ChemPhysChem* 1–11 (2016).
7. Carter, N. J. & Cross, R. A. Mechanics of the kinesin step. *Nature* **435**, 308 (2005).
8. Kudernac, T. *et al.* Electrically driven directional motion of a four-wheeled molecule on a metal surface. *Nature* **479**, 208–211 (2011).
9. Shirai, Y., Morin, J.-F., Sasaki, T., Guerrero, J. M. & Tour, J. M. Recent progress on nanovehicles. *Chemical Society Reviews* **35**, 1043–1055 (2006).
10. Chiang, P.-T. *et al.* Toward a light-driven motorized nanocar: Synthesis and initial imaging of single molecules. *Acs Nano* **6**, 592–597 (2011).
11. Morin, J.-F., Sasaki, T., Shirai, Y., Guerrero, J. M. & Tour, J. M. Synthetic Routes toward Carborane-Wheeled Nanocars. *J. Org. Chem.* **72**, 9481–9490 (2007).
12. Akimov, A. V., Nemukhin, A. V., Moskovsky, A. A., Kolomeisky, A. B. & Tour, J. M. Molecular Dynamics of Surface-Moving Thermally Driven Nanocars. *J. Chem. Theory Comput.* **4**, 652–656 (2008).
13. Furukawa, H., Cordova, K. E., O'Keeffe, M. & Yaghi, O. M. The Chemistry and Applications of Metal-Organic Frameworks. *Science* **341**, 1230444 (2013).
14. Long, J. R. & Yaghi, O. M. The pervasive chemistry of metal–organic frameworks. *Chemical Society Reviews* **38**, 1213–1214 (2009).

15. Kitagawa, S. Metal–organic frameworks (MOFs). *Chemical Society Reviews* **43**, 5415–5418 (2014).
16. Zhou, H.-C., Long, J. R. & Yaghi, O. M. Introduction to Metal–Organic Frameworks. *Chem. Rev.* **112**, 673–674 (2012).
17. Cui, Y. *et al.* Metal–organic frameworks as platforms for functional materials. *Accounts of chemical research* **49**, 483–493 (2016).
18. Lu, W. *et al.* Tuning the structure and function of metal–organic frameworks via linker design. *Chemical Society Reviews* **43**, 5561–5593 (2014).
19. Alberts, B. *Molecular biology of the cell*. (Garland science, 2017).
20. Erbas-Cakmak, S., Leigh, D. A., McTernan, C. T. & Nussbaumer, A. L. Artificial Molecular Machines. *Chem. Rev.* **115**, 10081–10206 (2015).
21. Kassem, S. *et al.* Artificial molecular motors. *Chemical Society Reviews* (2017) doi:10.1039/C7CS00245A.
22. Kistemaker, J. C. M., Štacko, P., Visser, J. & Feringa, B. L. Unidirectional rotary motion in achiral molecular motors. *Nat Chem* **7**, 890–896 (2015).
23. Yang, W., Li, Y., Liu, H., Chi, L. & Li, Y. Design and Assembly of Rotaxane-Based Molecular Switches and Machines. *Small* **8**, 504–516 (2012).
24. Feringa, B. L., van Delden, R. A., Koumura, N. & Geertsema, E. M. Chiroptical molecular switches. *Chemical Reviews* **100**, 1789–1816 (2000).
25. Murakami, H., Kawabuchi, A., Matsumoto, R., Ido, T. & Nakashima, N. A multi-mode-driven molecular shuttle: photochemically and thermally reactive azobenzene rotaxanes. *Journal of the American Chemical Society* **127**, 15891–15899 (2005).
26. Bissell, R. A., Córdova, E., Kaifer, A. E. & Stoddart, J. F. A chemically and electrochemically switchable molecular shuttle. *Nature* **369**, 133 (1994).
27. Lewandowski, B. *et al.* Sequence-specific peptide synthesis by an artificial small-molecule machine. *Science* **339**, 189–193 (2013).
28. Kassem, S. *et al.* Stereodivergent synthesis with a programmable molecular machine. *Nature* **549**, 374 (2017).
29. Bo, G. *et al.* An artificial molecular machine that builds an asymmetric catalyst. *Nature nanotechnology* **13**, 381 (2018).
30. Prasanna de Silva, A. & McClenaghan, N. D. Proof-of-principle of molecular-scale arithmetic. *Journal of the American Chemical Society* **122**, 3965–3966 (2000).

31. Magri, D. C., Brown, G. J., McClean, G. D. & de Silva, A. P. Communicating chemical congregation: a molecular AND logic gate with three chemical inputs as a “lab-on-a-molecule” prototype. *Journal of the American Chemical Society* **128**, 4950–4951 (2006).
32. Klärner, F.-G. & Kahlert, B. Molecular tweezers and clips as synthetic receptors. Molecular recognition and dynamics in receptor- substrate complexes. *Accounts of chemical research* **36**, 919–932 (2003).
33. Yurke, B., Turberfield, A. J., Mills Jr, A. P., Simmel, F. C. & Neumann, J. L. A DNA-fuelled molecular machine made of DNA. *Nature* **406**, 605 (2000).
34. Ceroni, P., Credi, A. & Venturi, M. Light to investigate (read) and operate (write) molecular devices and machines. *Chemical Society Reviews* **43**, 4068–4083 (2014).
35. Silvi, S., Venturi, M. & Credi, A. Light operated molecular machines. *Chemical Communications* **47**, 2483–2489 (2011).
36. Berna, J. *et al.* Macroscopic transport by synthetic molecular machines. *Nature materials* **4**, 704 (2005).
37. Badjić, J. D., Balzani, V., Credi, A., Silvi, S. & Stoddart, J. F. A molecular elevator. *Science* **303**, 1845–1849 (2004).
38. Tuncel, D., Özsar, Ö., Tiftik, H. B. & Salih, B. Molecular switch based on a cucurbit [6] uril containing bistable [3] rotaxane. *Chemical Communications* 1369–1371 (2007).
39. Nguyen, T. D. *et al.* Construction of a pH-driven supramolecular nanovalve. *Organic letters* **8**, 3363–3366 (2006).
40. Zhao, Y.-L. *et al.* A redox-switchable α -cyclodextrin-based [2] rotaxane. *Journal of the American chemical society* **130**, 11294–11296 (2008).
41. Bruns, C. J. *et al.* Redox switchable daisy chain rotaxanes driven by radical–radical interactions. *Journal of the American Chemical Society* **136**, 4714–4723 (2014).
42. Zhang, Z., Han, C., Yu, G. & Huang, F. A solvent-driven molecular spring. *Chemical Science* **3**, 3026–3031 (2012).
43. Klajn, R., Browne, K. P., Soh, S. & Grzybowski, B. A. Nanoparticles that “remember” temperature. *Small* **6**, 1385–1387 (2010).
44. Stoddart, J. F. The chemistry of the mechanical bond. *Chemical Society Reviews* **38**, 1802–1820 (2009).
45. Bruns, C. J. & Stoddart, J. F. Rotaxane-based molecular muscles. *Accounts of chemical research* **47**, 2186–2199 (2014).

46. Iwaso, K., Takashima, Y. & Harada, A. Fast response dry-type artificial molecular muscles with [c2] daisy chains. *Nature chemistry* **8**, 625–632 (2016).
47. Goujon, A. *et al.* Bistable [c 2] Daisy Chain Rotaxanes as Reversible Muscle-like Actuators in Mechanically Active Gels. *Journal of the American Chemical Society* **139**, 14825–14828 (2017).
48. Jang, S. S. *et al.* Structures and properties of self-assembled monolayers of bistable [2] rotaxanes on Au (111) surfaces from molecular dynamics simulations validated with experiment. *Journal of the American Chemical Society* **127**, 1563–1575 (2005).
49. Jang, Y. H., Jang, S. S. & Goddard, W. A. Molecular dynamics simulation study on a monolayer of half [2] rotaxane self-assembled on Au (111). *Journal of the American Chemical Society* **127**, 4959–4964 (2005).
50. Jang, S. S. *et al.* Molecular dynamics simulation of amphiphilic bistable [2] rotaxane Langmuir monolayers at the air/water interface. *Journal of the American Chemical Society* **127**, 14804–14816 (2005).
51. Kim, H. *et al.* Free energy barrier for molecular motions in bistable [2] rotaxane molecular electronic devices. *The Journal of Physical Chemistry A* **113**, 2136–2143 (2009).
52. Kelly, T. R., De Silva, H. & Silva, R. A. Unidirectional rotary motion in a molecular system. *Nature* **401**, 150 (1999).
53. Vicario, J., Meetsma, A. & Feringa, B. L. Controlling the speed of rotation in molecular motors. Dramatic acceleration of the rotary motion by structural modification. *Chemical Communications* 5910–5912 (2005).
54. Fang, C., Oruganti, B. & Durbeej, B. Computational study of the working mechanism and rate acceleration of overcrowded alkene-based light-driven rotary molecular motors. *RSC Advances* **4**, 10240–10251 (2014).
55. Oruganti, B., Fang, C. & Durbeej, B. Computational design of faster rotating second-generation light-driven molecular motors by control of steric effects. *Physical Chemistry Chemical Physics* **17**, 21740–21751 (2015).
56. Oruganti, B., Wang, J. & Durbeej, B. Computational Insight to Improve the Thermal Isomerisation Performance of Overcrowded Alkene-Based Molecular Motors through Structural Redesign. *ChemPhysChem* **17**, 3399–3408 (2016).
57. Wang, J., Oruganti, B. & Durbeej, B. Light-driven rotary molecular motors without point chirality: a minimal design. *Physical Chemistry Chemical Physics* **19**, 6952–6956 (2017).
58. Oruganti, B., Wang, J. & Durbeej, B. Quantum chemical design of rotary molecular motors. *International Journal of Quantum Chemistry* **118**, e25405 (2018).

59. Wang, J. & Durbееj, B. Toward Fast and Efficient Visible-Light-Driven Molecular Motors: A Minimal Design. *ChemistryOpen* **7**, 583–589 (2018).
60. Wang, J. & Durbееj, B. Molecular motors with high quantum efficiency and visible-light responsiveness: Meeting two challenges in one design. *Computational and Theoretical Chemistry* **1148**, 27–32 (2019).
61. Konyukhov, S. S. *et al.* Rigid-body molecular dynamics of fullerene-based nanocars on metallic surfaces. *Journal of chemical theory and computation* **6**, 2581–2590 (2010).
62. Akimov, A. V., Williams, C. & Kolomeisky, A. B. Charge transfer and chemisorption of fullerene molecules on metal surfaces: application to dynamics of nanocars. *The Journal of Physical Chemistry C* **116**, 13816–13826 (2012).
63. Akimov, A. V. & Kolomeisky, A. B. Unidirectional rolling motion of nanocars induced by electric field. *The Journal of Physical Chemistry C* **116**, 22595–22601 (2012).
64. Ganji, M. D., Ahangari, M. G. & Emami, S. M. Carborane-wheeled nanocar moving on graphene/graphyne surfaces: van der Waals corrected density functional theory study. *Materials Chemistry and Physics* **148**, 435–443 (2014).
65. Zhu, K., O’keefe, C. A., Vukotic, V. N., Schurko, R. W. & Loeb, S. J. A molecular shuttle that operates inside a metal–organic framework. *Nature chemistry* **7**, 514 (2015).
66. Proserpio, D. M. Topological crystal chemistry: Polycatenation weaves a 3D web. *Nat Chem* **2**, 435–436 (2010).
67. Guo, X.-G., Yang, W.-B., Wu, X.-Y., Lin, L. & Lu, C.-Z. 3D/3D Hetero-Interpenetrating Diamondoid Framework and Homo-Interpenetrating pcu Network by a One-Pot Reaction. *Eur. J. Inorg. Chem.* **2014**, 2481–2485 (2014).
68. Zhang, M.-D. *et al.* Chiral 3D/3D hetero-interpenetrating framework with six kinds of helices, 3D polyrotaxane and 2D network via one-pot reaction. *CrystEngComm* **15**, 227–230 (2012).
69. Xu, H. *et al.* An unprecedented 3D/3D hetero-interpenetrated MOF built from two different nodes, chemical composition, and topology of networks. *CrystEngComm* **14**, 5720–5722 (2012).
70. Wen, L., Cheng, P. & Lin, W. Mixed-motif interpenetration and cross-linking of high-connectivity networks led to robust and porous metal–organic frameworks with high gas uptake capacities. *Chemical Science* **3**, 2288 (2012).
71. Yao, X.-Q. *et al.* Chiral and Porous Coordination Polymers Based on an N-Centered Triangular Rigid Ligand. *Crystal Growth & Design* **11**, 231–239 (2011).
72. Lee, H.-J. *et al.* Controlled assembly of an unprecedented 2D + 3D interpenetrated array of (4,4)-connected and pcu topologies. *CrystEngComm* **13**, 4814–4816 (2011).

73. Hou, L., Zhang, J.-P. & Chen, X.-M. Two Metal-Carboxylate Frameworks Featuring Uncommon 2D + 3D and 3-Fold-Interpenetration: (3,5)-Connected Isomeric hms and gra Nets. *Crystal Growth & Design* **9**, 2415–2419 (2009).
74. Carlucci, L., Ciani, G., Maggini, S. & Proserpio, D. M. A New Polycatenated 3D Array of Interlaced 2D Brickwall Layers and 1D Molecular Ladders in $[\text{Mn}_2(\text{bix})_3(\text{NO}_3)_4] \cdot 2\text{CHCl}_3$ [bix = 1,4-bis(imidazol-1-ylmethyl)benzene] That Undergoes Supramolecular Isomerization upon Guest Removal. *Crystal Growth & Design* **8**, 162–165 (2008).
75. Carlucci, L., Ciani, G. & Proserpio, D. M. A new type of entanglement involving one-dimensional ribbons of rings catenated to a three-dimensional network in the nanoporous structure of $[\text{Co}(\text{bix})_2(\text{H}_2\text{O})_2](\text{SO}_4) \cdot 7\text{H}_2\text{O}$ [bix = 1,4-bis(imidazol-1-ylmethyl)benzene]. *Chem. Commun.* 380–381 (2004) doi:10.1039/B314322H.
76. Sasa, M., Tanaka, K., Bu, X.-H., Shiro, M. & Shionoya, M. Spontaneously Resolved Chiral Interpenetrating 3-D Nets with Two Different Zinc Coordination Polymers. *J. Am. Chem. Soc.* **123**, 10750–10751 (2001).
77. Carlucci, L., Ciani, G. & Proserpio, D. M. Three-dimensional architectures of intertwined planar coordination polymers: the first case of interpenetration involving two different bidimensional polymeric motifs. *New J. Chem.* **22**, 1319–1321 (1998).
78. Carlucci, L., Ciani, G., Proserpio, D. M. & Rizzato, S. New architectures from the self-assembly of MII SO_4 salts with bis(4-pyridyl) ligands. The first case of polycatenation involving three distinct sets of 2D polymeric (4,4)-layers parallel to a common axis. *CrystEngComm* **5**, 190–199 (2003).
79. Carlucci, L. & Ciani, G. An unprecedented triply interpenetrated chiral network of ‘square-planar’ metal centres from the self-assembly of copper (II) nitrate and 1, 2-bis (4-pyridyl) ethyne. *Chemical Communications* 1837–1838 (1998).
80. A. Blatov, V., Carlucci, L., Ciani, G. & M. Proserpio, D. Interpenetrating metal–organic and inorganic 3D networks: a computer-aided systematic investigation. Part I. Analysis of the Cambridge structural database. *CrystEngComm* **6**, 378–395 (2004).
81. Baburin, I. A., Blatov, V. A., Carlucci, L., Ciani, G. & Proserpio, D. M. Interpenetrating metal-organic and inorganic 3D networks: a computer-aided systematic investigation. Part II [1]. Analysis of the Inorganic Crystal Structure Database (ICSD). *Journal of Solid State Chemistry* **178**, 2452–2474 (2005).
82. Gong, Y.-N., Zhong, D.-C. & Lu, T.-B. Interpenetrating metal–organic frameworks. *CrystEngComm* **18**, 2596–2606 (2016).
83. Wang, Z.-L., Fang, W.-H. & Yang, G.-Y. The first three-fold interpenetrated framework with two different four-connected uniform nets of 6 6 dia and new chiral 8 6 mdf networks. *Chemical Communications* **46**, 8216–8218 (2010).

84. Wu, H., Yang, J., Su, Z.-M., Batten, S. R. & Ma, J.-F. An exceptional 54-fold interpenetrated coordination polymer with 103-srs network topology. *Journal of the American Chemical Society* **133**, 11406–11409 (2011).
85. Farha, O. K., Malliakas, C. D., Kanatzidis, M. G. & Hupp, J. T. Control over catenation in metal–organic frameworks via rational design of the organic building block. *Journal of the American Chemical Society* **132**, 950–952 (2009).
86. Rosi, N. L., Eddaoudi, M., Kim, J., O’Keeffe, M. & Yaghi, O. M. Infinite Secondary Building Units and Forbidden Catenation in Metal–Organic Frameworks. *Angew. Chem. Int. Ed.* **41**, 284–287 (2002).
87. Deng, H. *et al.* Large-pore apertures in a series of metal-organic frameworks. *science* **336**, 1018–1023 (2012).
88. Song, F., Wang, C., Falkowski, J. M., Ma, L. & Lin, W. Isoreticular chiral metal–organic frameworks for asymmetric alkene epoxidation: tuning catalytic activity by controlling framework catenation and varying open channel sizes. *Journal of the American Chemical Society* **132**, 15390–15398 (2010).
89. Rankine, D., Avellaneda, A., Hill, M. R., Doonan, C. J. & Sumby, C. J. Control of framework interpenetration for in situ modified hydroxyl functionalised IRMOFs. *Chemical Communications* **48**, 10328–10330 (2012).
90. Choi, S. B. *et al.* Reversible Interpenetration in a Metal–Organic Framework Triggered by Ligand Removal and Addition. *Angewandte Chemie International Edition* **51**, 8791–8795 (2012).
91. Ferguson, A. *et al.* Controlled partial interpenetration in metal–organic frameworks. *Nat Chem* **8**, 250–257 (2016).
92. Reineke, T. M., Eddaoudi, M., Moler, D., O’keeffe, M. & Yaghi, O. Large Free Volume in Maximally Interpenetrating Networks: The Role of Secondary Building Units Exemplified by Tb₂(ADB)₃[(CH₃)₂SO]₄·16[(CH₃)₂SO]·1. *Journal of the American Chemical Society* **122**, 4843–4844 (2000).
93. Long, D.-L. *et al.* Anion Control over Interpenetration and Framework Topology in Coordination Networks Based on Homoleptic Six-Connected Scandium Nodes. *Chemistry-A European Journal* **11**, 1384–1391 (2005).
94. Chen, B., Eddaoudi, M., Hyde, S., O’keeffe, M. & Yaghi, O. Interwoven metal-organic framework on a periodic minimal surface with extra-large pores. *Science* **291**, 1021–1023 (2001).
95. Wilmer, C. E. *et al.* Large-scale screening of hypothetical metal–organic frameworks. *Nature Chemistry* **4**, 83–89 (2012).

96. Colón, Y. J., Gómez-Gualdrón, D. A. & Snurr, R. Q. Topologically Guided, Automated Construction of Metal–Organic Frameworks and Their Evaluation for Energy-Related Applications. *Crystal Growth & Design* **17**, 5801–5810 (2017).
97. D. Allendorf, M. & Stavila, V. Crystal engineering, structure–function relationships, and the future of metal–organic frameworks. *CrystEngComm* **17**, 229–246 (2015).
98. Chung, Y. G. *et al.* Computation-Ready, Experimental Metal–Organic Frameworks: A Tool To Enable High-Throughput Screening of Nanoporous Crystals. *Chem. Mater.* **26**, 6185–6192 (2014).
99. Sezginel, K. B. *Discovering interpenetration in MOFs.* (2018).
100. Lennard-Jones, J. E. Cohesion. *Proc. Phys. Soc.* **43**, 461 (1931).
101. Rappe, A. K., Casewit, C. J., Colwell, K. S., Goddard, W. A. & Skiff, W. M. UFF, a full periodic table force field for molecular mechanics and molecular dynamics simulations. *J. Am. Chem. Soc.* **114**, 10024–10035 (1992).
102. Kim, J., Martin, R. L., Rübel, O., Haranczyk, M. & Smit, B. High-Throughput Characterization of Porous Materials Using Graphics Processing Units. *J. Chem. Theory Comput.* **8**, 1684–1693 (2012).
103. Halder, P., Maurya, M., Jain, S. K. & Singh, J. K. Understanding adsorption of CO₂, N₂, CH₄ and their mixtures in functionalized carbon nanotube arrays. *Phys. Chem. Chem. Phys.* **18**, 14007–14016 (2016).
104. Groom, C. R., Bruno, I. J., Lightfoot, M. P. & Ward, S. C. The Cambridge Structural Database. *Acta Cryst B, Acta Cryst Sect B, Acta Crystallogr B, Acta Crystallogr Sect B, Acta Crystallogr B Struct Crystallogr Cryst Chem, Acta Crystallogr Sect B Struct Crystallogr Cryst Chem* **72**, 171–179 (2016).
105. Hafizovic, J. *et al.* The inconsistency in adsorption properties and powder XRD data of MOF-5 is rationalized by framework interpenetration and the presence of organic and inorganic species in the nanocavities. *Journal of the American Chemical Society* **129**, 3612–3620 (2007).
106. Sezginel, K. B., Feng, T. & Wilmer, C. E. Discovery of hypothetical hetero-interpenetrated MOFs with arbitrarily dissimilar topologies and unit cell shapes. *CrystEngComm* **19**, 4497–4504 (2017).
107. Rowsell, J. L. C., Millward, A. R., Park, K. S. & Yaghi, O. M. Hydrogen Sorption in Functionalized Metal–Organic Frameworks. *J. Am. Chem. Soc.* **126**, 5666–5667 (2004).
108. Allen, C. A. & Cohen, S. M. Exploration of Chemically Cross-Linked Metal–Organic Frameworks. *Inorg. Chem.* **53**, 7014–7019 (2014).

109. Mellot-Draznieks, C., Dutour, J. & Férey, G. Computational Design of Hybrid Frameworks: Structure and Energetics of Two $\text{Me}_3\text{OF}_3\{-\text{O}_2\text{C}-\text{C}_6\text{H}_4-\text{CO}_2-\}_3$ Metal-Dicarboxylate Polymorphs, MIL-hypo-1 and MIL-hypo-2. *Z. anorg. allg. Chem.* **630**, 2599–2604 (2004).
110. Wang, T. C. *et al.* Ultrahigh Surface Area Zirconium MOFs and Insights into the Applicability of the BET Theory. *J. Am. Chem. Soc.* **137**, 3585–3591 (2015).
111. Liu, D. *et al.* A Reversible Crystallinity-Preserving Phase Transition in Metal–Organic Frameworks: Discovery, Mechanistic Studies, and Potential Applications. *J. Am. Chem. Soc.* **137**, 7740–7746 (2015).
112. Hao, X.-R. *et al.* Remarkable solvent-size effects in constructing novel porous 1,3,5-benzenetricarboxylate metal–organic frameworks. *CrystEngComm* **14**, 5596–5603 (2012).
113. Zheng, B., Yang, Z., Bai, J., Li, Y. & Li, S. High and selective CO_2 capture by two mesoporous acylamide-functionalized rht-type metal–organic frameworks. *Chem. Commun.* **48**, 7025–7027 (2012).
114. Graham, A. J., Tan, J.-C., Allan, D. R. & Moggach, S. A. The effect of pressure on Cu-btc: framework compression vs. guest inclusion. *Chem. Commun.* **48**, 1535–1537 (2012).
115. Yan, Y. *et al.* Metal–Organic Polyhedral Frameworks: High H_2 Adsorption Capacities and Neutron Powder Diffraction Studies. *J. Am. Chem. Soc.* **132**, 4092–4094 (2010).
116. Lock, N. *et al.* Elucidating Negative Thermal Expansion in MOF-5. *J. Phys. Chem. C* **114**, 16181–16186 (2010).
117. Yuan, D., Zhao, D., Sun, D. & Zhou, H.-C. An Isorecticular Series of Metal–Organic Frameworks with Dendritic Hexacarboxylate Ligands and Exceptionally High Gas-Uptake Capacity. *Angewandte Chemie International Edition* **49**, 5357–5361 (2010).
118. Larsen, R. W., Miksovská, J., Musselman, R. L. & Wojtas, L. Ground- and Excited-State Properties of Zn(II) Tetrakis(4-tetramethylpyridyl) Porphyrin Specifically Encapsulated within a Zn(II) HKUST Metal–Organic Framework. *J. Phys. Chem. A* **115**, 11519–11524 (2011).
119. Schneemann, A. *et al.* Flexible metal–organic frameworks. *Chemical Society Reviews* **43**, 6062–6096 (2014).
120. Zhang, H., Deria, P., K. Farha, O., T. Hupp, J. & Q. Snurr, R. A thermodynamic tank model for studying the effect of higher hydrocarbons on natural gas storage in metal–organic frameworks. *Energy & Environmental Science* **8**, 1501–1510 (2015).
121. Mason, J. A., Veenstra, M. & Long, J. R. Evaluating metal–organic frameworks for natural gas storage. *Chemical Science* **5**, 32–51 (2014).
122. Babaei, H., McGaughey, A. J. & Wilmer, C. E. Effect of pore size and shape on the thermal conductivity of metal-organic frameworks. *Chemical Science* **8**, 583–589 (2017).

123. Babaei, H. & Wilmer, C. E. Mechanisms of heat transfer in porous crystals containing adsorbed gases: Applications to metal-organic frameworks. *Physical review letters* **116**, 025902 (2016).
124. Morse, P. M. Diatomic molecules according to the wave mechanics. II. Vibrational levels. *Physical Review* **34**, 57 (1929).
125. Eddaoudi, M. *et al.* Systematic design of pore size and functionality in isoreticular MOFs and their application in methane storage. *Science* **295**, 469–472 (2002).
126. Plimpton, S. Fast parallel algorithms for short-range molecular dynamics. *Journal of computational physics* **117**, 1–19 (1995).
127. Che, J., Çağın, T., Deng, W. & Goddard III, W. A. Thermal conductivity of diamond and related materials from molecular dynamics simulations. *The Journal of Chemical Physics* **113**, 6888–6900 (2000).
128. Schneemann, A. *et al.* Flexible metal–organic frameworks. *Chem. Soc. Rev.* **43**, 6062–6096 (2014).
129. Mason, J. A. *et al.* Methane storage in flexible metal–organic frameworks with intrinsic thermal management. *Nature* **527**, 357–361 (2015).
130. Raatikainen, K. & Rissanen, K. Breathing molecular crystals: halogen- and hydrogen-bonded porous molecular crystals with solvent induced adaptation of the nanosized channels. *Chem. Sci.* **3**, 1235–1239 (2012).
131. Wang, Z. *et al.* Soft Porous Crystal Based upon Organic Cages That Exhibit Guest-Induced Breathing and Selective Gas Separation. *J. Am. Chem. Soc.* **141**, 9408–9414 (2019).
132. Serre, C., Millange, F., Surblé, S. & Férey, G. A Route to the Synthesis of Trivalent Transition-Metal Porous Carboxylates with Trimeric Secondary Building Units. *Angewandte Chemie International Edition* **43**, 6285–6289 (2004).
133. Férey, G. *et al.* A Chromium Terephthalate-Based Solid with Unusually Large Pore Volumes and Surface Area. *Science* **309**, 2040–2042 (2005).
134. Barthelet, K., Marrot, J., Riou, D. & Férey, G. A Breathing Hybrid Organic–Inorganic Solid with Very Large Pores and High Magnetic Characteristics. *Angewandte Chemie International Edition* **41**, 281–284 (2002).
135. Serre, C., Mellot-Draznieks, S., Surblé, N., Audebrand, Y., Filinchuk, G. F. Role of Solvent-Host Interactions That Lead to Very Large Swelling of Hybrid Frameworks. *Science* **315**, 1828–1831 (2007).
136. Liu, Y. *et al.* Reversible Structural Transition in MIL-53 with Large Temperature Hysteresis. *J. Am. Chem. Soc.* **130**, 11813–11818 (2008).

137. Yot, P. G. *et al.* Large breathing of the MOF MIL-47(VIV) under mechanical pressure: a joint experimental–modelling exploration. *Chem. Sci.* **3**, 1100–1104 (2012).
138. Loiseau, T. *et al.* A Rationale for the Large Breathing of the Porous Aluminum Terephthalate (MIL-53) Upon Hydration. *Chemistry – A European Journal* **10**, 1373–1382 (2004).
139. Neimark, A. V., Coudert, F.-X., Boutin, A. & Fuchs, A. H. Stress-Based Model for the Breathing of Metal–Organic Frameworks. *J. Phys. Chem. Lett.* **1**, 445–449 (2010).
140. Vanduyfhuys, L. *et al.* Thermodynamic insight into stimuli-responsive behaviour of soft porous crystals. *Nat Commun* **9**, 1–9 (2018).
141. Boutin, A. *et al.* Breathing Transitions in MIL-53(Al) Metal–Organic Framework Upon Xenon Adsorption. *Angewandte Chemie International Edition* **48**, 8314–8317 (2009).
142. Yue, Y. *et al.* A Flexible Metal–Organic Framework: Guest Molecules Controlled Dynamic Gas Adsorption. *J. Phys. Chem. C* **119**, 9442–9449 (2015).
143. Salles, F. *et al.* Molecular Dynamics Simulations of Breathing MOFs: Structural Transformations of MIL-53(Cr) upon Thermal Activation and CO₂ Adsorption. *Angewandte Chemie International Edition* **47**, 8487–8491 (2008).
144. Wieme, J. *et al.* Thermal Engineering of Metal–Organic Frameworks for Adsorption Applications: A Molecular Simulation Perspective. *ACS Appl. Mater. Interfaces* (2019) doi:10.1021/acsami.9b12533.
145. Huang, B. L., McGaughey, A. J. H. & Kaviani, M. Thermal conductivity of metal-organic framework 5 (MOF-5): Part I. Molecular dynamics simulations. *International Journal of Heat and Mass Transfer* **50**, 393–404 (2007).
146. Zhang, X. & Jiang, J. Thermal Conductivity of Zeolitic Imidazolate Framework-8: A Molecular Simulation Study. *J. Phys. Chem. C* **117**, 18441–18447 (2013).
147. Wang, X. *et al.* Anisotropic Lattice Thermal Conductivity and Suppressed Acoustic Phonons in MOF-74 from First Principles. *J. Phys. Chem. C* **119**, 26000–26008 (2015).
148. Babaei, H. & Wilmer, C. E. Mechanisms of Heat Transfer in Porous Crystals Containing Adsorbed Gases: Applications to Metal-Organic Frameworks. *Phys. Rev. Lett.* **116**, 025902 (2016).
149. Babaei, H., McGaughey, A. J. H. & Wilmer, C. E. Effect of pore size and shape on the thermal conductivity of metal-organic frameworks. *Chem. Sci.* **8**, 583–589 (2016).
150. Babaei, H., McGaughey, A. J. H. & Wilmer, C. E. Transient Mass and Thermal Transport during Methane Adsorption into the Metal–Organic Framework HKUST-1. *ACS Appl. Mater. Interfaces* **10**, 2400–2406 (2018).

151. Sezginel, K. B., Asinger, P. A., Babaei, H. & Wilmer, C. E. Thermal Transport in Interpenetrated Metal–Organic Frameworks. *Chem. Mater.* **30**, 2281–2286 (2018).
152. Huang, B. L. *et al.* Thermal conductivity of a metal-organic framework (MOF-5): Part II. Measurement. *International Journal of Heat and Mass Transfer* **50**, 405–411 (2007).
153. Liu, D. *et al.* MOF-5 composites exhibiting improved thermal conductivity. *International Journal of Hydrogen Energy* **37**, 6109–6117 (2012).
154. Ming, Y. *et al.* Thermophysical properties of MOF-5 powders. *Microporous and Mesoporous Materials* **185**, 235–244 (2014).
155. Cui, B. *et al.* Thermal Conductivity of ZIF-8 Thin-Film under Ambient Gas Pressure. *ACS Appl. Mater. Interfaces* **9**, 28139–28143 (2017).
156. Schelling, P. K., Phillpot, S. R. & Keblinski, P. Comparison of atomic-level simulation methods for computing thermal conductivity. *Phys. Rev. B* **65**, 144306 (2002).
157. Babaei, H., Keblinski, P. & Khodadadi, J. M. Equilibrium molecular dynamics determination of thermal conductivity for multi-component systems. *Journal of Applied Physics* **112**, 054310 (2012).
158. Plimpton, S. Fast Parallel Algorithms for Short-Range Molecular Dynamics. *Journal of Computational Physics* **117**, 1–19 (1995).
159. Boone, P., Babaei, H. & Wilmer, C. E. Heat Flux for Many-Body Interactions: Corrections to LAMMPS. *J. Chem. Theory Comput.* **15**, 5579–5587 (2019).
160. Maginn, E. J., Bell, A. T. & Theodorou, D. N. Transport diffusivity of methane in silicalite from equilibrium and nonequilibrium simulations. *J. Phys. Chem.* **97**, 4173–4181 (1993).
161. Babaei, H., DeCoster, M. E., Jeong, M., Hassan, Z. M., Islamoglu, T., Baumgart, H., McGaughey, A. J. H., Engelbert, R., Farha, O. K., Hopkins, P. E., Malen, J. A. & Wilmer, C. E. Observation of reduced thermal conductivity in a metal-organic framework due to the presence of adsorbates.
162. Rosei, F. *et al.* Organic Molecules Acting as Templates on Metal Surfaces. *Science* **296**, 328–331 (2002).
163. Otero, R. *et al.* Lock-and-key effect in the surface diffusion of large organic molecules probed by STM. *Nature Materials* **3**, 779–782 (2004).
164. Schunack, M. *et al.* Long jumps in the surface diffusion of large molecules. *Physical review letters* **88**, 156102 (2002).
165. Rosei, F. *et al.* Properties of large organic molecules on metal surfaces. *Progress in Surface Science* **71**, 95–146 (2003).

166. Shirai, Y., Osgood, A. J., Zhao, Y., Kelly, K. F. & Tour, J. M. Directional control in thermally driven single-molecule nanocars. *Nano Letters* **5**, 2330–2334 (2005).
167. Joachim, C. & Rapenne, G. Molecule Concept Nanocars: Chassis, Wheels, and Motors? *ACS Nano* **7**, 11–14 (2013).
168. Castelvechi, D. Drivers gear up for world’s first nanocar race. *Nature News* **544**, 278 (2017).
169. Rapenne, G. & Joachim, C. The first nanocar race. *Nat. Rev. Mater* **2**, 17040 (2017).
170. Simpson, G. J., García-López, V., Petermeier, P., Grill, L. & Tour, J. M. How to build and race a fast nanocar. *Nature Nanotechnology* <https://www.nature.com/articles/nnano.2017.137> (2017) doi:10.1038/nnano.2017.137.
171. Pawlak, R. & Meier, T. Fast and curious. *Nature Nanotechnology* **12**, 712–712 (2017).
172. Sun, Q. *et al.* Controlling on-surface molecular diffusion behaviors by functionalizing the organic molecules with tert-butyl groups. *Appl. Phys. Lett.* **103**, 013103 (2013).
173. Lavasani, S. M. H., Pishkenari, H. N. & Meghdari, A. A closer look at the motion of p-carborane on gold surface. in *Manipulation, Automation and Robotics at Small Scales (MARSS), International Conference on 1–6* (IEEE, 2016).
174. Weckesser, J., Barth, J. V. & Kern, K. Mobility and bonding transition of $\{\mathrm{C}\}_{60}$ on Pd(110). *Phys. Rev. B* **64**, 161403 (2001).
175. Weckesser, J., Barth, J. V. & Kern, K. Direct observation of surface diffusion of large organic molecules at metal surfaces: PVBA on Pd(110). *J. Chem. Phys.* **110**, 5351–5354 (1999).
176. Kumar, S., Rosenberg, J. M., Bouzida, D., Swendsen, R. H. & Kollman, P. A. The weighted histogram analysis method for free-energy calculations on biomolecules. I. The method. *Journal of computational chemistry* **13**, 1011–1021 (1992).
177. Perdew, J. P. Density-functional approximation for the correlation energy of the inhomogeneous electron gas. *Phys. Rev. B* **33**, 8822–8824 (1986).
178. Grimme, S., Ehrlich, S. & Goerigk, L. Effect of the damping function in dispersion corrected density functional theory. *Journal of Computational Chemistry* **32**, 1456–1465 (2011).
179. Weigend, F. & Ahlrichs, R. Balanced basis sets of split valence, triple zeta valence and quadruple zeta valence quality for H to Rn: Design and assessment of accuracy. *Physical Chemistry Chemical Physics* **7**, 3297–3305 (2005).
180. Neese, F. The ORCA program system. *Wiley Interdisciplinary Reviews: Computational Molecular Science* **2**, 73–78 (2012).
181. Larsen, A. H. *et al.* The atomic simulation environment—a Python library for working with atoms. *J. Phys.: Condens. Matter* **29**, 273002 (2017).

182. Dubbeldam, D., Beerdsen, E., Vlugt, T. J. H. & Smit, B. Molecular simulation of loading-dependent diffusion in nanoporous materials using extended dynamically corrected transition state theory. *The Journal of chemical physics* **122**, 224712 (2005).
183. Hanwell, M. D. *et al.* Avogadro: an advanced semantic chemical editor, visualization, and analysis platform. *Journal of cheminformatics* **4**, 17 (2012).
184. Sezginel, K. B. *Ångström, a Python package for basic molecular operations with minimal-dependency: kbsezginel/angstrom.* (2018).
185. Sezginel, K. B. *Nanocar builder Avogadro 2 plug-in.* (2018).
186. Li, H., Eddaoudi, M., O’Keeffe, M. & Yaghi, O. M. Design and synthesis of an exceptionally stable and highly porous metal-organic framework. *Nature* **402**, 276–279 (1999).
187. Dubbeldam, D., Calero, S., Ellis, D. E. & Snurr, R. Q. RASPA: molecular simulation software for adsorption and diffusion in flexible nanoporous materials. *Molecular Simulation* **42**, 81–101 (2016).
188. Kwon, O., Park, S., Zhou, H.-C. & Kim, J. Computational prediction of hetero-interpenetration in metal-organic frameworks. *Chem. Commun.* **53**, 1953–1956 (2017).
189. Xu, H. *et al.* An unprecedented 3D/3D hetero-interpenetrated MOF built from two different nodes, chemical composition, and topology of networks. *CrystEngComm* **14**, 5720–5722 (2012).
190. Macrae, C. F. *et al.* Mercury CSD 2.0 – new features for the visualization and investigation of crystal structures. *J Appl Cryst, J Appl Crystallogr* **41**, 466–470 (2008).
191. Sezginel, K. B. *TherMOF.*
192. Schelling, P. K., Phillpot, S. R. & Keblinski, P. Comparison of atomic-level simulation methods for computing thermal conductivity. *Physical Review B* **65**, 144306 (2002).
193. Babaei, H., Keblinski, P. & Khodadadi, J. M. Equilibrium molecular dynamics determination of thermal conductivity for multi-component systems. *Journal of Applied Physics* **112**, 054310 (2012).
194. Martínez, L., Andrade, R., Birgin, E. G. & Martínez, J. M. PACKMOL: a package for building initial configurations for molecular dynamics simulations. *Journal of computational chemistry* **30**, 2157–2164 (2009).
195. Grossfield, A. *WHAM: the weighted histogram analysis method”, version 2.0.9.*
196. Sezginel, K. B. *Python wrapper for Weighted Histogram Analysis Method as implemented by Grossfield et al.* (2019).